Super resolution imaging in coherent Raman scattering for biological tissues

Julien Guilbert

PSL
UNIVERSITÉ PARIS

THÈSE DE DOCTORAT
DE L'UNIVERSITÉ PSL

Préparée à Laboratoire Kastler Brossel - École Normale Supérieure de Paris

Imagerie de super résolution en diffusion Raman stimulée pour des tissus biologiques

Super resolution imaging in coherent Raman scattering for biological tissues

Soutenue par
Julien Guilbert
Le 8 Mars 2022

École doctorale n°564
École Doctorale de Physique en Île de France

Spécialité
Physique

Composition du jury :

Emmanuel Beaurepaire Directeur de recherche, CNRS	*Rapporteur*
Dario Polli Professeur, Politecnico di Milano	*Rapporteur*
Alexandra Fragola Maîtresse de conférence, Sorbonne Université	*Examinatrice*
Sandrine Lévêque-Fort Directrice de recherche, CNRS	*Examinatrice*
Gilles Tessier Directeur de recherche, CNRS	*Président*
Sylvain Gigan Professeur, Sorbonne Université	*Directeur de thèse*
Hilton Barbosa de Aguiar Chargé de recherche, CNRS	*Co-encadrant*

Laboratoire Kastler Brossel
Physique quantique et applications

ENS
ÉCOLE NORMALE SUPÉRIEURE

Département de Physique
École normale supérieure

COLLÈGE DE FRANCE
1530

SORBONNE UNIVERSITÉ
CRÉATEURS DE FUTURS DEPUIS 1257

Remerciement

Tout d'abord, je souhaite remercier les membres de mon jury de défense de thèse. Je remercie Gilles Tessier, président du jury, Emmanuel Beaurepaire et Dario Poli, rapporteurs du jury, et Sandrine Lévêque-Fort et Alexandra Fragola, examinatrices du jury. Je vous remercie, toutes et tous, pour le temps passé à relire mon manuscript, je vous remercie de m'avoir écouté et enfin je vous remercie pour les discussions pointues et agréables que nous avons pu avoir. Pour l'anecdote, je remercie Alexandra et Sandrine de m'avoir montré des astuces de membres du jury lors de la conférence Mifobio.

Également membres du jury mais aussi partie prenante de mes recherches, je souhaite remercier mes deux directeurs de thèse, Sylvain Gigan notamment pour le financement et Hilton Barbosa de Aguiar pour m'avoir introduit et formé dans le fourmillant groupe *Complex Media Optics Lab.* Au sein du laboratoire, je veux également remercier toute la partie administrative du labo, Audrey, Christelle, Stéphanie, Thierry et Valérie sans qui, nous doctorants, post-doc et permanents ne pouvons pas faire grand chose. Tout autant merci à Arnaud et Nabil qui s'occupent de l'atelier et de la réalisation de nos pièces sur mesure.

Notre groupe de recherche est constitué de gens formidables avec qui j'ai passé trois années pleines de rencontres et de découvertes. Je tiens donc à remercier celles et ceux qui étaient là quand je suis arrivé : Antoine, Baptiste, Claudio, Jonathan, Louisiane, Saroch, Tom, toutes celles et tous ceux arrivé.e.s pendant Bernhard, Bingxin, Fernando, Lorenzo, Michal, Mushegh, Pauline, Zen et celles et ceux qui restent après moi Alexandra, Fei, Gianni, Léa, Lei, Louis, Raj, Yonseok. Je tiens également à remercier Baba, Tunc et Walter qui ont travaillé avec moi lors de leurs stages respectifs.

Plus personnellement, je tiens à remercier les amis du labo pour avoir partagé tous ces moments : Lei et Mushegh pour la bonne humeur, Léa et Louis pour l'excellente relève, Gianni pour ces parties endiablées, Louisiane et Alexandra, pour toutes nos discussions passées à refaire le monde et refaire le monde refait. Je vous remercie pour tout, ce qui est mentionné ici mais aussi tout ce qui ne rentre pas dans ces quelques courts mots. En parallèle, je remercie toutes et tous mes ami.e.s d'école et les HX3, les numéros 10, pour tous les moments de bonheur que nous avons passés durant ces 3 années et ceux qui suivront.

Je remercie mon Papa et ma Maman pour être venus jusqu'à Paris et qui m'ont surtout aidé à devenir ce que je suis aujourd'hui. Je remercie Léo et Marsu, les frères que je voulais, je veux et je voudrai.

Je garde ces derniers mots pour celle qui pendant une bonne partie de ma thèse, en plus de la sienne, a fait preuve de courage pour me supporter pendant des journées, des semaines, des mois entiers, notamment à cause de vous savez quoi. Maëlle, tout simplement merci pour les moments que nous avons partagés, et plus simplement encore, merci pour tout.

Acronyms

CARS	Coherent Anti-Stokes Raman Scattering
SIM	Structured Illumination Microscopy
SRS	Stimulated Raman Scattering
1PF	1 photon fluorescence
2PF	2 photon fluorescence
3PF	3 photon fluorescence
STED	Saturated Emission Depletion
PALM	PhotoActivated Localization Microscopy
STORM	Stochastic Optical Reconstruction Microscopy
NIR	Near infrared
FOV	Field Of View
NA	Numerical Aperture
ROI	Region Of Interest
SNR	Signal to Noise Ratio
PSF	Point Spread Function
FWHM	Full Width at Half Maximum
SLM	Spatial Light Modulator
DMD	Digital Micromirror Device
OTF	Optical Transfer Function
MTF	Modulation Transfer Function
PTF	Phase Transfer Function
AO	Adaptive Optics

Abstract

The development of optical imaging has led to numerous advances in the field of life science. During the last fifteen years, fluorescence microscopy and the associated super-resolution methods have experienced an intense development which notably have applications in the field of neuroscience. However, not all biological tissues are naturally fluorescent and it is therefore necessary to incorporate markers that will specifically bind to a particular molecule. This introduction of markers in biological tissues can disrupt the normal functioning of the cells. In addition, the development of new markers requires many years of work in order to obtain a molecule compatible with biological applications and which binds specifically to the targeted molecules. Finally, the emission spectrum of fluorophores being wide (1500 cm^{-1}), it is then complicated to tag and image several chemical species simultaneously. It is generally considered that beyond 4 or 5 fluorophores, the imaging system becomes extremely complex.

For all these reasons, it would be desirable to develop imaging techniques and in particular super-resolution methods that do not use external chemical markers even in complex medium like biological tissues which are generally considered as sensitive and cannot support too high energy densities. Moreover, because all molecules have unique Raman scattering resonance signatures, Raman scattering is an ideal candidate in order to image label-free tissues and to be able to target specific molecule types. However, the signal being low due to the spontaneous nature of the emission prevents from imaging fast enough. A common solution that we exploited in this thesis is the use of coherent Raman scattering which greatly improves the cross section of the signal and thus the imaging speed. Nevertheless, microscopy techniques are limited in resolution by diffraction, which may be problematic when imaging subwavelength biological structures. In order to obtain images beyond the resolution limit, it is possible to choose among three main categories of technique such as photoactivated localization microscopy (PALM), stimulated emission depletion (STED) or structured illumination microscopy (SIM). For the PALM category, it is necessary to use blinking fluorophores and is therefore not compatible with the non blinking nature of Raman scattering. Moreover, unlike fluorescence, coherent Raman scattering is much less efficient and the STED category already requires a lot of power in fluorescence and seems not to be the

most relevant here. This is why we have chosen to develop a technique using coherent Raman scattering with an original strategy in order to couple it with SIM techniques during this PhD thesis. First, we will present in the manuscript numerical simulations of the technique to show that it is indeed able to perform super resolution. Second, we did experimental realizations of this technique on calibrated plastic samples larger than the diffraction limit to make sure the hardware and software were working as expected. Following that, we imaged calibrated beads below the diffraction limit and could resolve them with our technique while the standard imaging technique failed to distinguish the beads. Third, we tested the imaging method on biological samples such as HeLa cells and axons of a mouse cerebellum. We showed that our methodology was compatible with biological imaging and it had the ability the reject the signal outside of the focus, a feature known as sectioning. At last, in order to push the resolution even further, it is necessary to solve a problem specific to structured illumination. Indeed, the number of images necessary to obtain a final super-resolved image drastically increases by using Raman scattering signals which are of non linear order 3 instead of 2. We then studied the statistics of the non-standard speckles that we propose to use as structured illuminations and its effects on the number of realizations needed to obtain a meaningful image. Finally, we study the extent to which these unnatural speckle statistics can be maintained with the presence of inhomogeneities in the medium.

To summarize, we demonstrated a new methodology using coherent Raman scattering in combination with SIM to achieve super resolution in a label-free manner which is compatible with biological samples. In addition, we studied the effect of changing speckle statistics on blind-SIM reconstructions and if it could sustain in a scattering medium.

Résumé

Le développement de l'imagerie optique a permis de nombreuses avancées dans le domaine de la biologie. Au cours des quinze dernières années, la microscopie de fluorescence et les méthodes de super-résolutions associées ont connu un essor important qui trouve notamment des applications dans le domaine des neurosciences. Cependant, les tissus biologiques ne sont pas tous naturellement fluorescents, et il est alors nécessaire de leurs incorporer des marqueurs qui vont se lier spécifiquement à une molécule. Cette introduction de marqueurs dans les tissus biologiques peut perturber le fonctionnement normal des cellules. De plus, la mise au point de nouveaux marqueurs requiert de nombreuses années de travail afin d'obtenir une molécule compatible avec les applications biologiques et qui se lie spécifiquement sur les molécules ciblées. Enfin, le spectre d'émission des fluorophores étant large (1500 cm^{-1}), il est compliqué de marquer et d'imager plusieurs espèces chimiques simultanément. Il est généralement considéré qu'au delà de 4 ou 5 fluorophores, le système d'imagerie devient extrêmement complexe.

Pour toutes ces raisons, l'objectif de ce doctorat est de développer une nouvelle technique d'imagerie et notamment une méthode n'utilisant pas de marqueurs chimiques externes. Plus précisément, cette thèse se propose de développer une technique d'imagerie de super résolution sans marqueur et compatible avec les tissus biologiques qui sont généralement considérés comme fragiles c'est à dire qu'ils ne peuvent supporter une densité d'énergie trop élevée. Afin d'imager des tissus sans marqueur et de pouvoir cibler un type précis de molécule, la diffusion Raman est une candidate idéale car toutes les molécules possèdent des signatures uniques appelées résonances de diffusion Raman. Cependant, le caractère spontané de l'émission ne permettrait pas d'imager suffisamment rapidement. Une solution communément employée et que nous avons exploitée dans cette thèse est l'utilisation du signal de la diffusion Raman cohérente qui améliore considérablement la section efficace du signal et donc la vitesse d'imagerie. Néanmoins, les techniques de microscopie sont limitées en résolution par la diffraction, ce qui peut être problématique lors de l'imagerie de structures biologiques sub-longueur d'onde. Afin d'obtenir des images allant au delà de la limite de résolution, il est possible de choisir parmi trois grandes catégories de techniques que sont la

microscopie par localisation photoactivée (PALM), la déplétion par émission stimulée (STED) ou la microscopie par illumination structurée (SIM). En ce qui concerne la catégorie PALM, il est nécessaire d'utiliser des fluorophores clignotants et cela n'est donc pas compatible avec l'objet de la thèse. De plus, à la différence de la fluorescence, la diffusion Raman cohérente est bien moins efficace et la catégorie STED nécessite déjà beaucoup de puissance en fluorescence et paraît ne pas être la plus pertinente du point de vue des dommages photo-induits. C'est pourquoi, nous avons choisi de développer durant cette thèse une technique utilisant la diffusion Raman cohérente avec une stratégie originale de scanning afin de pouvoir l'utiliser en combinaison avec des techniques de SIM. Nous montrerons dans le manuscrit des simulations numériques de cette technique pour montrer qu'elle est effectivement capable d'atteindre la super résolution.

Ensuite, nous avons effectué des réalisations expérimentales de cette technique sur des échantillons de plastique calibrés, plus grands que la limite de diffraction, afin de nous assurer que le matériel et le logiciel fonctionnent comme prévu. Ensuite, nous avons imagé des billes calibrées en dessous de la limite de diffraction et nous avons pu les résoudre avec notre technique alors que la technique d'imagerie standard ne parvenait pas à distinguer les billes. Enfin, nous avons testé la méthode d'imagerie sur des échantillons biologiques tels que des cellules HeLa et des axones de cervelet de souris. Nous avons montré que notre méthode était compatible avec l'imagerie biologique et qu'elle avait la capacité de rejeter le signal en dehors du foyer optique, une caractéristique connue sous le nom de sectionnement optique. Enfin, dans le but de pousser la résolution encore plus loin, nous envisageons d'utiliser des ordres de nonlinéarités plus élevé. Il est alors nécessaire de résoudre une problématique propre à l'illumination structurée. En effet, le nombre d'image nécessaire afin d'obtenir une image finale super résolue pourrait augmenter drastiquement en utilisant des signaux de diffusion Raman qui sont d'ordre de non linéarité 3 au lieu de 2. Nous proposons alors d'étudier la statistique des tavelures (speckle) utilisée en tant qu'illumination structurée et étudions ses effets sur le nombre d'images alors nécessaire pour obtenir une image reconstruite. Enfin, nous étudions à quel point ces statistiques non naturelles de speckle peuvent se maintenir avec une présence d'inhomogénéïté dans le milieu.

En résumé, nous avons démontré une nouvelle méthodologie utilisant la diffusion Raman cohérente en combinaison avec la SIM pour obtenir une technique de super résolution sans marqueur, compatible avec les échantillons biologiques. En outre, nous avons étudié l'effet de la modification des statistiques de speckle sur les reconstructions SIM aveugles et si cette méthode peut être maintenue dans un milieu diffusant.

抽象

光学成像的发展推动了生命科学领域的诸多技术进步。过去的 15 年里，荧光显微镜和与其相关的超分辨率方法经历了飞速的发展，尤其是在神经科学应用领域。然而，并不是所有的生物组织都具有天然荧光的特性，因此需要引入具有与特定分子结合功能的标记物。这种在生物组织中引入标记物的过程通常会破坏细胞的正常功能。此外，开发新的标记物需要多年的工作，以便获得一个与生物应用相适应的分子与生物应用兼容，并能与目标分子特异性结合。最后，荧光体的发射光谱很宽（1500 cm^{-1}），因此，同时标记和成像几个化学物相当复杂。一般认为，超过 4 或 5 个荧光团，成像系统因此变得极其复杂。

由于上述原因，最好能开发出不使用外部化学标记的成像技术和特别的超分辨率成像方法，在生物组织类似的复杂介质中同样适用，该介质一般被认为是敏感的，且不承受太高的能量密度。此外，由于所有的分子都有独特的拉曼散射共振特征，所以拉曼散射是一种理想的候选方法，以便对无标记的组织进行成像，并能够针对特定的分子类型进行成像。然而，由于自发性质信号强度弱的特点，因此无法快速成像。在本博士论文中利用一种常见的解决方案即使用相干拉曼散射，该方法极大提高了信号的横截面，进而提高了成像速度。然而，显微镜技术的分辨率受到衍射极限的限制，在对亚波长生物结构成像时可能会出现问题。为了获得超出分辨率限制的图像，可以在以下三大类技术中进行选择，如光敏定位显微技术（PALM）、受激发射损耗荧光显微术（STED）或结构光照明显微技术（SIM）。对于 PALM 技术，必须使用闪烁的荧光体，因此与拉曼散射的非闪烁性质不兼容。此外，与荧光不同，相干拉曼散射的效率要低得多，而且 STED 技术在荧光中成像中需要很大的功率，因此难以实施。这就是为什么我们选择使用相干拉曼散射来开发一种原创性的技术，将相干拉曼散射与 SIM 技术结合起来。在本博士论文中，首先，我们在论文中介绍该技术的数值模拟，以表明它确实能够实现超级分辨率。其次，在大于衍射极限的校准样品上对该技术进行了实验验证，以确保硬件和软件能按预期工作。之后，对低于衍射极限的校准样本进行了成像，并且证明了该方法的有效性，而标准的成像技术却无法分辨出这些样本。第三，我们利用小鼠的小脑和 HeLa 细胞等生物样品测试了该成像方法的有效性。实验结果表明，我们所提出的方法与生物成像兼容，它可以拒筛出焦点以外的信号，具有切片成像的特点。最后，为了进一步提高分辨率，有必要解决结构化照明的问题。事实上，通过使用非线性阶数为 3 而不是 2 的拉曼散射信号，获得最终超分辨率图像所需的图像数量急剧增加。然后，我们研究了利用具有非标准统计特性的结构化照明的可行性，及获得有意义图像与所需的照明数量的关系。最后，我们研究了在介质中存在不均匀性的情况下，这些非自然的散斑统计可以在多大程度上保持。

总而言之，本博士论文展示了一种新的将相干拉曼散射与 SIM 相结合成像方法，通过无标签的方式实现超级分辨率，且该技术与生物样品的兼容性很强。此外，我们研究了改变散斑的统计特性对于盲 SIM 重建的影响以及它是否能在散射介质中持续存在的问题。

Contents

List of Figures

List of Tables

Chapter 1

Introduction

1.1 Introduction to microscopy imaging

Observing the world around us with pieces of glass has a very long history and dates back 4000 years. Surprisingly enough, these pieces of glass were first used to look at the sky and stars with the invention of the first telescopes [1]. A bit later in time, the invention of the first microscopes combining an objective close to the specimen and an ocular seems to come from Europe and it is claimed by several individuals like Z. Janssen, H. Martens, C. Drebbel and G. Galileo in the early 1600s. Only a few decades after, for the first time microscopes were used for biological purposes by naturalist R. Hooke [2] (see Fig.1.1.c.) and by A. Van Leeuwenhoek, an outstanding lens crafter who kept secret his manufacturing techniques. In 1900s, light microscopy had a tremendously wide range of applications that goes from the observation of nanometer-size gold particles — which led to the 1925 Nobel Prize in chemistry awarded to Adolf Zsigmondy — to the discovery of Green Fluorescent Protein found in jellyfish [3] — which was applied to biological problem after scientists managed to hash, clone [4] and express the nucleotide in biological systems [5]. Nowadays, the combination of images acquired from a physical microscope with computer science and mathematics is opening new frontiers for the exploration of biological systems with optical microscopes. As illustrated above, the field has contributions from many scientists from very broad background such as physicists, chemists, biologists and more recently mathematicians and computer scientists.

This chapter is meant to introduce the essential notions to understand the work described in this PhD manuscript devoted to optical label-free super resolution microscopy. We will first study fluorescence microscopy and label-free imaging to give a background on light microscopy. Then, we will explore more in depth the theory of coherent Raman processes and understand why they are intrinsic signals from a specimen and thus need no label. Finally, we will explore the origin of the diffraction resolution limit and describe a few methods to go beyond. We will go more in depth on structured illumination microscopy.

1.1.1 Fluorescence imaging

Since fluorescence is the most broadly used technique in bioimaging, we will introduce it so that we can better understand why for some applications we would want to use a different contrast mechanism. Fluorescence consists in the absorption of a photon so that the molecule goes from its electronic ground state to excited states. After absorption, the molecule radiates some part of the energy under non-radiative process like internal conversion and vibrational relaxation dissipating as heat. Finally, the de-excitation of the molecule can happen in two ways (See Fig.1.2):

- No photon is emitted and the molecule de-excites through non-radiative pro-

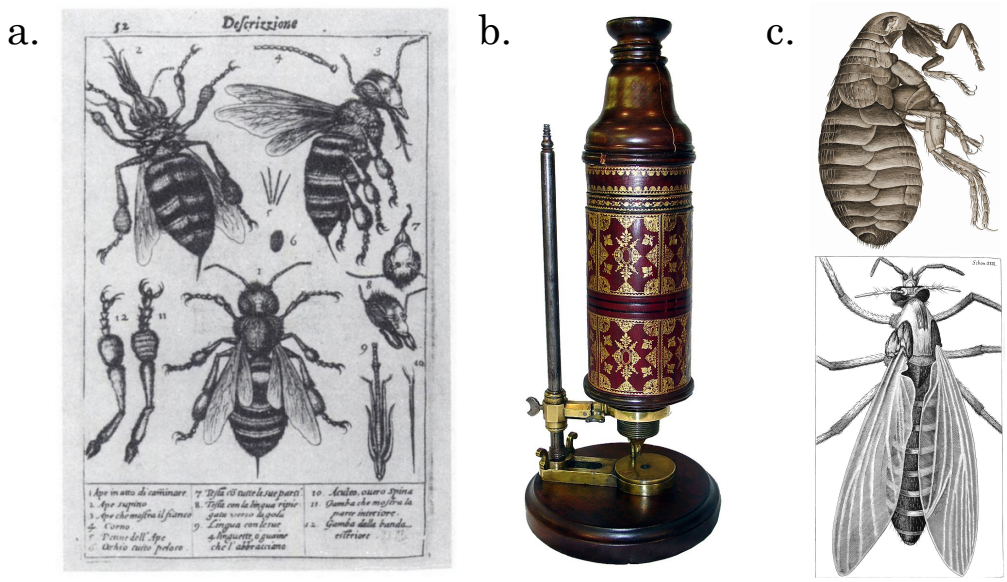

Figure 1.1: **First drawing made by using a microscope**.
a. Drawings from what Galileo saw under his microscope. **b.** R. Hooke's microscope. **c.** Images of a flea and a gnat extracted from Micrographia [2] written by R. Hooke.

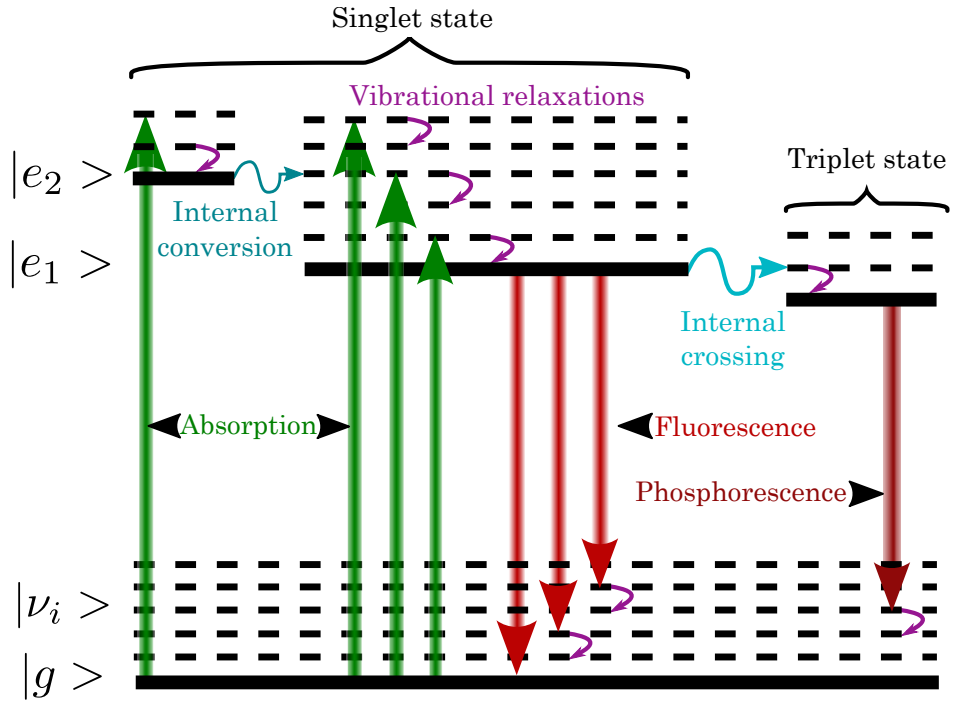

Figure 1.2: **Fluorescence Jablonski diagram**.
$|g\rangle$, $|\nu_i\rangle$ and $|e_i\rangle$ are respectively the ground state, vibrational states and excited states of the molecule. Dashed line represents vibrational state of the molecule.

cesses. It can be because of quenching which is often caused by collisions with oxygen molecules — efficient quencher due to its triplet ground state —

- Through the relaxation of the molecule from the excited state to the ground state, a photon whose energy corresponds to the de-excitation gap is emitted in an incoherent manner. But intersystem crossing can also result in the emission of a photon of phosphorescence and compete with fluorescence emission.

These complex interactions of light with matter make the creation of new markers tedious and time and resource consuming. Nevertheless, many fluorescence marker spanning the whole visible range exist and are commonly used into biological samples. As can be seen in Fig.1.3, fluorescence is in particular essential for neuroimaging using fluorescence and a lot of effort is focused on making it easier for biologists to study brain tissues. In Fig.1.3.a., we can see a 3D volume imaged using a 3 photon fluorescence (3PF) which shows ability to image at unprecedented depth of ~ 1.5 mm [6, 8] (we will develop later what are the advantages of using higher nonlinear order). In Fig.1.3.b. or c., we can see multi-color imaging coding for different synaptic circuit [7]. These colors are genetically encoded and enable to map the brain circuitry of a mouse.

Hence, fluorescence provides powerful tools to study many biological applications. However, most of the biological samples do not exhibit fluorescence naturally but it is possible to stain the tissues with markers. Those markers can bind specifically to the desired biological molecule but have detrimental effects that we are going to elaborate on in the next section.

1.1.2 Label-free imaging and Raman scattering

Fluorescence imaging has become the most popular imaging technique due to its very high efficiency and the ability to detect single molecules which led to super resolution techniques down to a resolution of a few nm. However, engineering new fluorescence marker is challenging and requires a lot of efforts so that they are efficient, bio compatible, binding to specific molecules and any other features that are desired for a given imaging application. Moreover, if illuminated for too long a fluorescence marker generally dims until it switches off completely, namely a phenomenon known as photobleaching. Furthermore, the preparation of the sample can be tedious and cumbersome and even alter the standard behavior of the cell or biological sample under study. Still, some biological tissues exhibit autofluorescence and thus fluorescence can be generated in label-free manner [9, 10]. To improve the resolution limit, we can think of using higher nonlinear order fluorescence signals like 2 photon or 3 photon fluorescence (respectively 2PF and 3PF) using the autofluorescence of the biological tissues. However, not every molecule has autofluorescence in the visible/NIR so it is limited to a reduced number of molecules and more importantly a longer wavelength has to be used to generate higher order fluorescence signals thus no significant gain in resolution is achieved

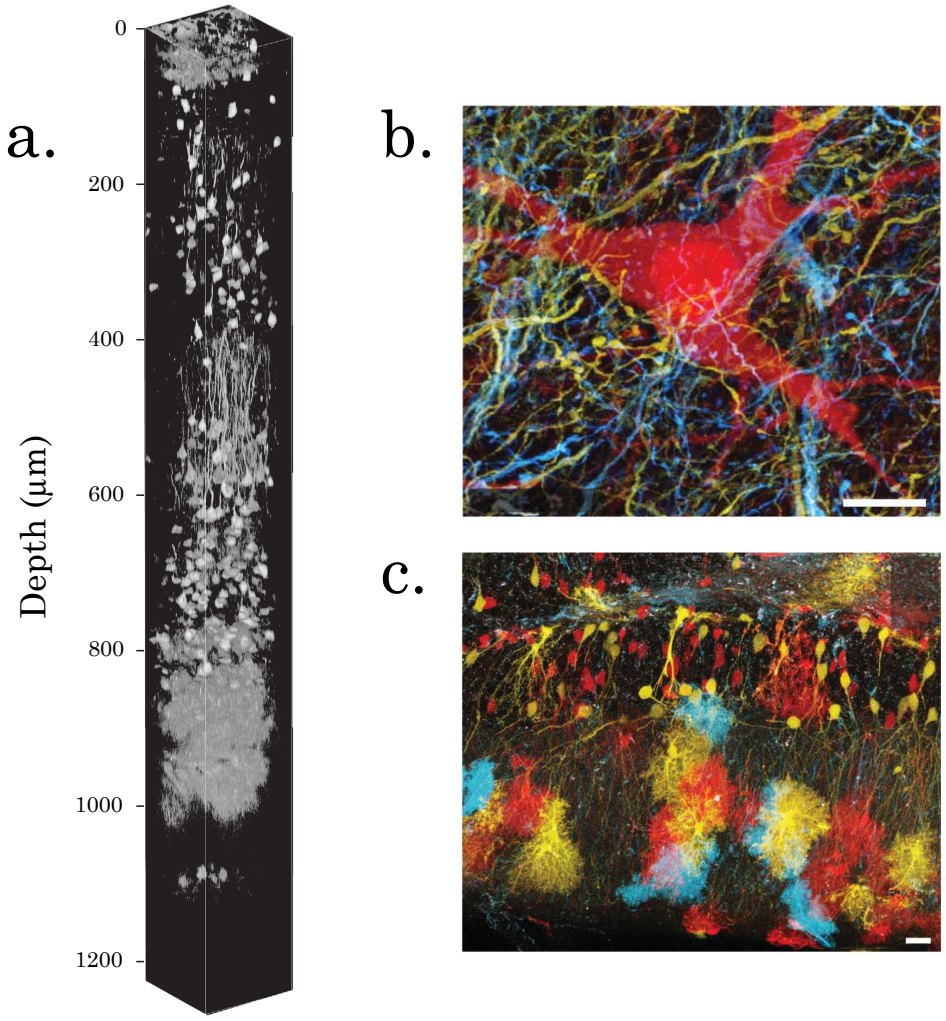

Figure 1.3: **Example of fluorescence images in mouse brain**.
a. In vivo 3PM images of RFP-labelled neurons in mouse brain. **b.** Thy1-Brainbow-1.0 transgenic mice were crossed with CreERT2-expressing animals. Tamoxifen injection led to mosaic XFP expression throughout the brain. Brainstem, line H. Scale bar, 10 μm. **c.** In Thy1-Brainbow-2.1 mice, CreERT2-mediated recombination leads to expression of multiple stochastic fluorescent proteins (XFPs). Hippocampus (dentate gyrus), line Q (labelled neurons and astrocytes). Scale bar, 20 μm. Images adapted from [6, 7]

but rather penetration depth and sectioning. In addition, second harmonic generation (SHG) [11, 12] and third harmonic generation (THG) [13, 14] can also reveal in a label-free manner some features of the architecture of a sample: organization and orientation of interfaces respectively. Indeed, SHG will reveal non centro symmetric and fairly ordered molecules like fiber architectures such as collagen or microtubules.

In contrast, label-free imaging has developed as an alternative imaging when it is

desirable to avoid markers. Label-free imaging does not require sample staining and enables to alleviate some of the issues of fluorescence imaging at the cost of conversion efficiency since label-free imaging contrast mechanisms are generally less efficient due to more subtle light-scattering processes. One of the pioneering discovery in label-free imaging was the phase-contrast microscopy [15] that was introduced by F. Zernike who was awarded the 1953 Nobel prize in Physics. It was followed by other interferometric far-field imaging techniques such as differential interference contrast, Mirau interference microscopy or modern digital holographic microscopy. However, these label-free techniques are not chemically selective which means that they are not able to segment between different kinds of molecules within the medium (see Fig.1.5). This property can be greatly beneficial for biological applications in order to distinguish between different constituents of a cell or to segment between healthy and cancerous tissues [16].

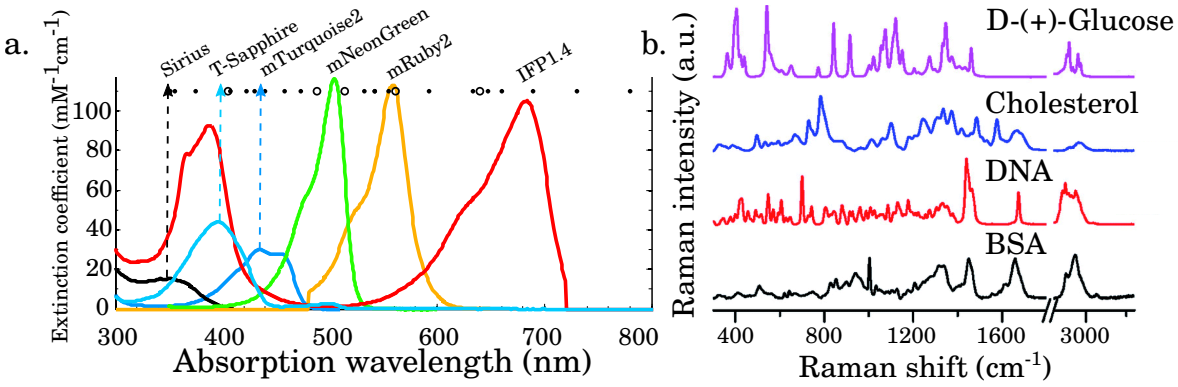

Figure 1.4: **Typical fluorescence and Raman emission spectrum**.
a. Different fluorescence emission spectrum covering the visible range from various markers. **b.** Spontaneous Raman spectrum from different biological molecules. Figure adapted from [17, 18].

As we will see later in section 1.2, molecules themselves can serve as natural marker using Raman scattering. Indeed, each molecule has a unique vibrational signature with sharp features which enables multi-spectral imaging. In comparison, fluorescence is also able to achieve chemical specificity but it rather originates from the binding mechanism. Indeed, fluorescence markers are designed to bind to specific molecules but the spectral emission from fluorescence markers is inherently broad so that it is challenging to image for more than 4 different colors [17, 19]. Basically, fluorescence emission spectrum are 1500 cm^{-1} wide while Raman spectrum resonances are only a few 10 cm^{-1} but more importantly Raman spectrum spread over thousands of cm^{-1} with many unique Raman resonance signatures which offer the possibility to distinguish between two very similar components (see Fig.1.4). Therefore, Raman scattering is a good candidate to achieve chemically selective label-free imaging. However, it is not

straightforward to combine Raman spectroscopic techniques with an imaging system for living sample. Nevertheless, as we will describe later, one of the most suitable signal for doing so is coherent Raman scattering since it is much more efficient than spontaneous Raman resulting in a few orders of magnitude faster imaging speed. Even though coherent Raman scattering requires more complex and expensive laser and imaging system, the imaging speed is a lot faster and can reach video-rate since it can go down from a few μs to a few tens of μs of pixel dwell time for single color and multi-color respectively. We can see in Fig.1.5.a. a C. elegans whose different components are segmented between lysosomes, lipids and proteins without any labeling and only exploiting Raman scattering resonances to distinguish between constituents. In addition, in Fig.1.6. we can see the different components of a cell and isolate each of them thanks to linear spectral decomposition methods. Thus, it is possible to disentangle partially overlapping spectral signals within a cell and have a quantitative value of each of the components in any pixel of the image [20]. To conclude, it is possible to obtain precise chemical quantification of biological tissue constituents at high speed in a label-free manner.

1.2 Raman scattering

In this section, we will first focus on the history of the Raman effect discovery to then explore more in depth its theoretical formalism starting with spontaneous Raman emission and then stimulated Raman effect such as Stimulated Raman Scattering (SRS) and Coherent Anti-Stokes Raman Scattering (CARS). This section is inspired by the paper from R. Singh [22], the tutorial from P. Berto et al. [23] and the book from R.W. Boyd [24].

1.2.1 History on the discovery of the Raman scattering effect

In 1923 in the context of the debate between whether wave or quantum theories of light is correct, by assuming a quantum structure of light [25], the Austrian theoretical physicist Adolf Smekal (See Fig.1.7.a.) predicted that scattered monochromatic light would consist of its original wavelength as well as of higher and lower wavelength [26]. However, the theoretical predictions from Smekal did not influence the experimental discovery of the Raman effect by Landsberg and Mandelstam or Krishnan and Raman himself [22]. Indeed, the soviet physicists Landsberg and Mandelstam were studying Albert Einstein's and Peter Debye's theories of the specific heats of solids and predicted a shift in frequency caused by wave propagating at the speed of sound. Then, the soviet physicist experimentally searched for this frequency shift in quartz but encountered a different one from what they had expected. They claimed that they discovered a new phenomenon while being uncertain of the explanation. Independantly, in 1928 in India,

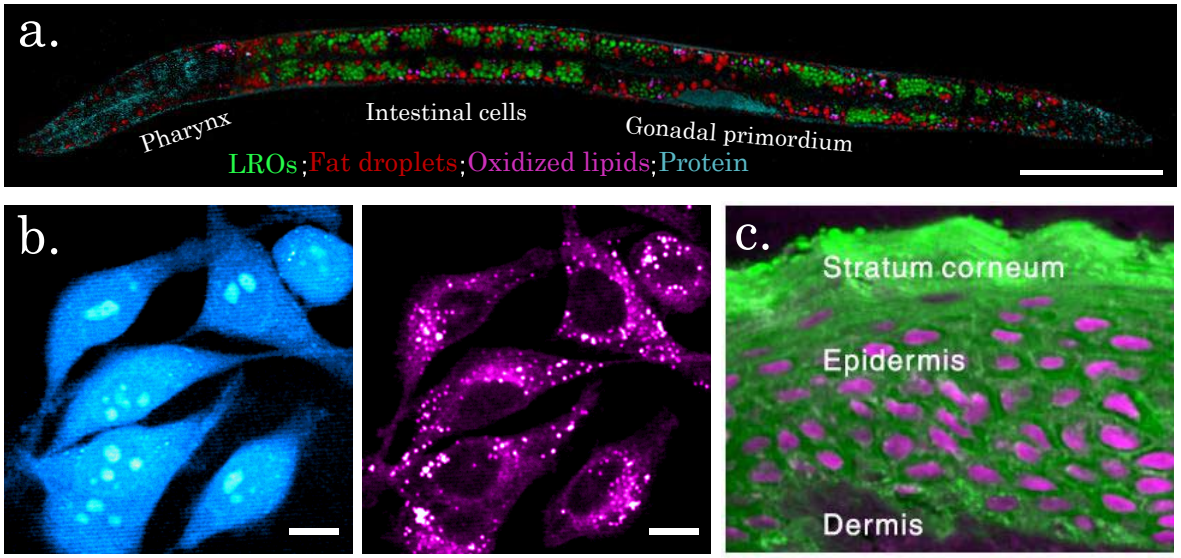

Figure 1.5: **Biological application of Stimulated Raman Scattering microscopy (SRS)**.
a. Chemical maps of intracellular compartments in C. elegans generated by hyperspectral SRS imaging and multivariate curve resolution analysis. The green, red, magenta, and cyan colors represent lysosome-related organelles (LROs), neutral fat droplets, oxidized lipids, and proteins, respectively, in the body of a daf-2 mutant. Scale bar, 50 μm **b.** SRS imaging of live HeLa cells using signals from C-D stretch vibration at 2133 cm^{-1} (left) and C-H stretch vibration at 2845 cm^{-1} (right). The C-D signal shows newly synthesized proteins by metabolic incorporation of a deuterium-labeled set of amino acids. Scale bars, 10 μm. **c.** SRS images of DNA (magenta) and lipids (green) in a normal human skin tissue section. Scale bar, 20 μm. Figure adapted from [20].

Krishnan and Raman[1] (See Fig.1.7. b. and c.) were searching for an equivalent of the Compton effect [27, 28] and reported a spectrum [29] (see Fig.1.7.g-d) which was the first reported Raman spectrum.

Indeed, we can see in Fig.1.7.d.-f. the excitation spectrum of a quartz mercury arc lamp with no sample for different optical filters. In Fig.1.7.e.-g. a sample of liquid benzene is illuminated by a quartz mercury arc lamp and we can see a set of new wavelength appearing on the right of Fig.1.7.e. or in the right of Fig.1.7.g. that are caused by Raman scattering. Shortly after this discovery, Raman was awarded the 1930 Nobel prize in physics. Even though Landsberg and Mandelstam discovered it simultaneously, Raman published before and they cited Raman's work so that the Nobel committee believed that they did not obtain their results independently. Last but not least Raman measured Raman spectrum in different states of the matter (solids,

[1]For more information on the interesting way Raman ended up in academia, from bank officer to 1930 Nobel price : read the Introduction in [22]

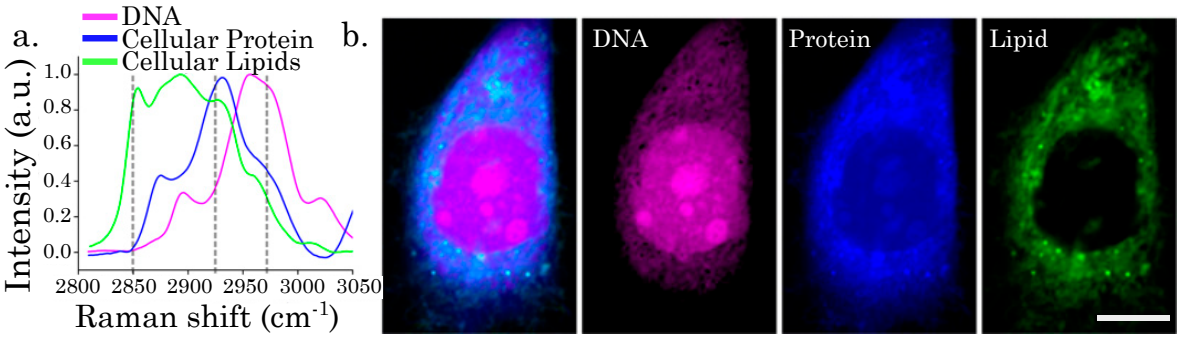

Figure 1.6: **Cell components separation in SRS**.
Label-free SRS imaging of DNA (magenta), protein (blue), and lipids (green) in live cells. SRS images at three selected Raman shifts in the CH stretching vibrational band were acquired. Linear decomposition was performed with a premeasured calibration matrix to retrieve the distribution of DNA, protein, and lipids. **a.** Raman spectra of DNA, cellular protein, and cellular lipids extracted from HeLa cells. **b.** SRS images of a live cell in interphase and the decomposed distribution of DNA, protein, lipids, and the overlay. Figure adapted from [21].

liquids, gases) thus showing the universality of the effect [22].

In the following of the section, we will describe the key features of spontaneous Raman and the fundamental principles of physics at work that will be a solid basis to then explore the physics of coherent Raman processes.

1.2.2 Spontaneous Raman scattering

At thermodynamic equilibrium, the two main types of interactions are absorption and scattering. Scattering consists in inhomogeneities modifying the direction of propagation of a photon. It can be divided in two categories:

- Elastic scattering of light is by far the predominant effect. The photons are scattered without modifying their original frequency: it is the Rayleigh scattering well known for explaining the color of the blue sky with Larmor formulae.

- Inelastic scattering of light : photons are scattered and their original frequency are changed. It is the case for Raman effect that was observed by the Soviet and Indian scientists aforementioned (see section1.2.1)

.

We can wonder where is this change in the original frequency originating from? To better understand it, we will use a simplified model using Lorentz oscillator model. In this model, an electron is bounded to a nucleus via a spring with a given stiffness and the electric field E is represented by a driving force F. In fact, the Raman effect originates

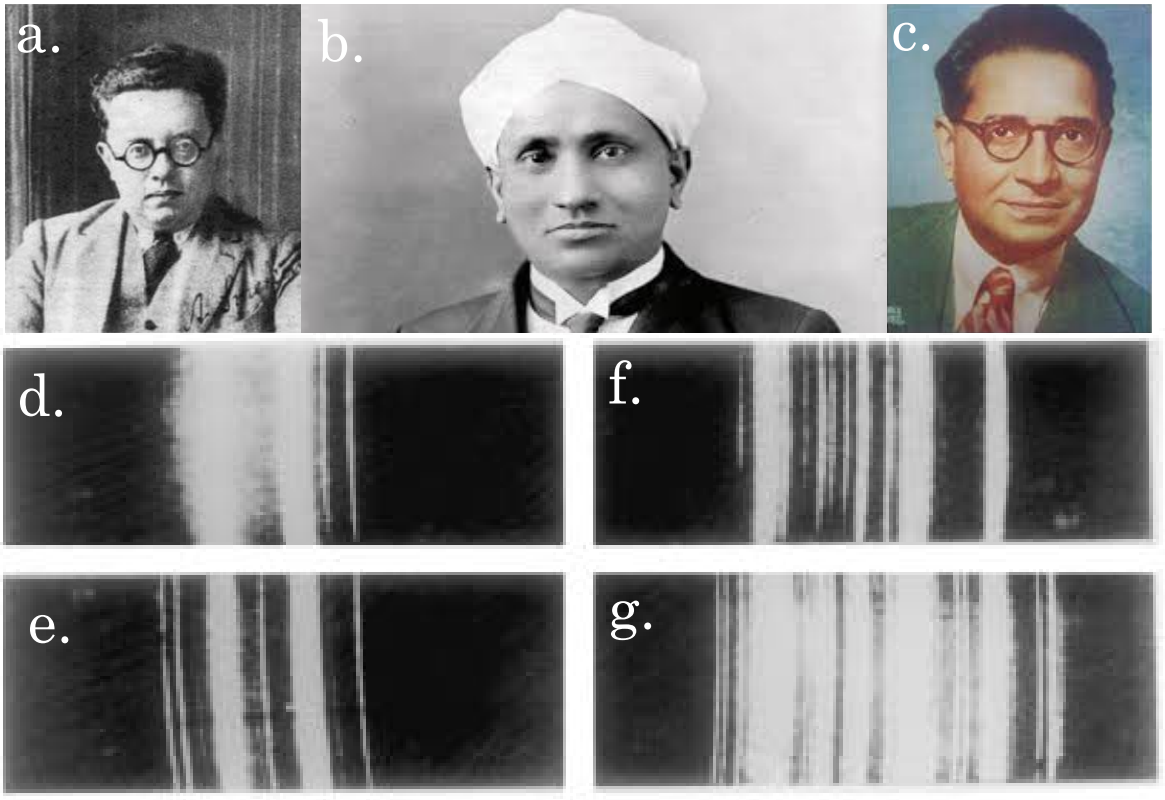

Figure 1.7: **First experimental discovery of Raman effect**.
a. Adolf Smekal **b.** Chandrasekhara Venkata Raman **c.** Kariamanikkam Srinivasa Krishnan **d.** Spectrum of filtered light from quartz mercury lamp taken with a small Adam Hilger spectroscope. **e.** Spectrum of light from quartz mercury lamp scattered on liquid benzene. **f.** and **g.** are the same as **c.** and **d.** respectively with a different filter for the quartz mercury arc lamp. Adapted from [22].

from the interaction between light and molecular vibrational resonances. These can be divided in several normal modes called roto-vibrational normal modes which form an orthogonal basis. These modes can have different resonant frequencies depending on the atomic mass, the nature of chemical bonds, molecule geometry and symmetry. Overall, any change to the stiffness of the molecule will change the vibrational energies and thus the resonant frequency. Nevertheless, the frequency span for usual molecules is in the infrared and ranges from 2.5 μm to 10 000 μm with the higher range of frequency (>25μm) only possible in gases[2].

In the model, we assume that a diatomic molecule can be represented by a harmonic oscillator with a resonant frequency ω_0 and composed of two masses m_1 and m_2 separated by a distance x_0 and linked by a spring (see Fig.1.9). The molecule does not require to intrinsically exhibit a dipole momentum, but the movement of the electronic

[2]Note that wavelength than 2.5μm are likely to excite overtone of these vibrations.

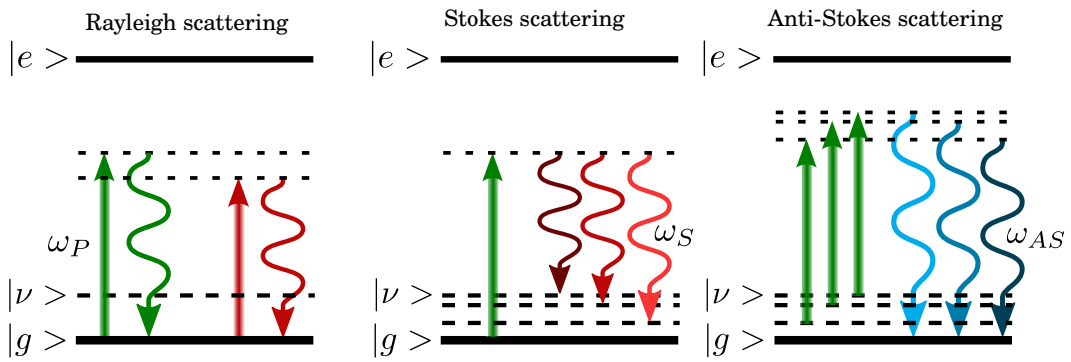

Figure 1.8: **Energy diagram for Rayleigh and Raman scattering**.
$|g\rangle$, $|\nu\rangle$ and $|e\rangle$ are respectively the ground state, vibrational state and excited state of the molecule. Dashed line represents virtual state of the molecule. **a.** Rayleigh scattering **b.** Stokes Raman scattering **c.** Anti-Stokes Raman scattering

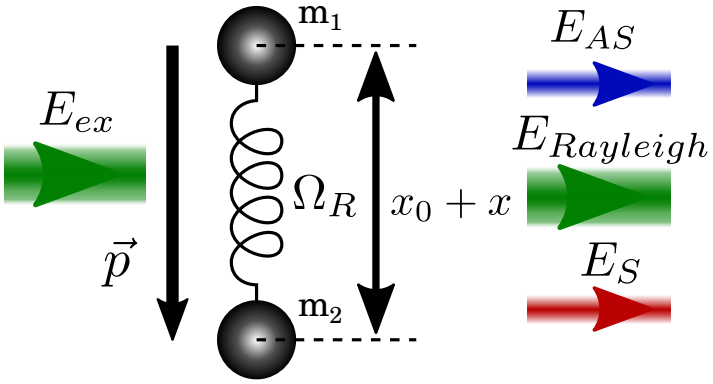

Figure 1.9: **Lorentz oscillator model for a diatomic molecule**.
Schematic of the Lorentz oscillator model for a molecule to explain Raman scattering physics with a simple harmonic oscillator model. E_{ex} is the incoming excitation field, $\vec{p}$ is the dipole moment, Ω_R is the resonant frequency of the molecule and $E_{Rayleigh}$, E_{AS}, E_S are respectively Rayleigh scattering, Anti-Stokes, Stokes Raman scattering.

cloud under electromagnetic field excitation will induce a dipole momentum. To characterize this effect we need to introduce the polarizability α of the molecule which is link to dipole momentum p by the following equation:

$$p(\vec{t}) = \epsilon_0 \alpha(t) \vec{E_0}(t) \tag{1.1}$$

Where ϵ_0 is the dielectric constant and $\vec{E_0}(t)$ the electric field.

All vectors are projected on the x axis. The system is operated at resonance frequency Ω_R such that $x(t) = x_f \cos(\Omega_R t)$ where x_f is the amplitude of x. We perform

a Taylor expansion of the polarizability in the assumption of small displacement:

$$\alpha = \alpha_0 + \left.\frac{\partial \alpha}{\partial x}\right|_{x_0} x(t) \tag{1.2}$$

Combining the two equation above (1.1) and (1.2), we finally obtain:

$$\begin{aligned} p(t) =& \epsilon_0 \left[\alpha_0 + \left.\frac{\partial \alpha}{\partial x}\right|_{x_0} x_f \cos(\Omega_R t)\right] E_0 \cos((\omega_p t) \\ =& \underbrace{\epsilon_0 \alpha_0 E_0 \cos(\omega_p t)}_{Rayleigh\ \ Scattering} + \\ & \underbrace{\frac{\epsilon_0 E_0 x_f}{2} \left.\frac{\partial \alpha}{\partial x}\right|_{x_0} \cos\Big((\omega_p - \Omega_R)t\Big)}_{Stokes\ \ Raman\ \ Scattering} + \\ & \underbrace{\frac{\epsilon_0 E_0 x_f}{2} \left.\frac{\partial \alpha}{\partial x}\right|_{x_0} \cos\Big((\omega_p + \Omega_R)t\Big)}_{anti-Stoke\ \ Raman\ \ Scattering} \end{aligned} \tag{1.3}$$

The first term oscillating at frequency ω_P which is the original frequency of the excitation corresponds to the Rayleigh scattering. The second term is oscillating at $\omega_S = \omega_P - \Omega_R$ which is of lower frequency than the original field. Thus, there is an exchange of energy between the field and the molecule which corresponds to a molecule in a higher vibrational state while a less energetic photon is created: it corresponds to the Stokes Raman scattering. On the contrary, the third term oscillating at frequency $\omega_{AS} = \omega_P + \Omega_R$ which is a higher frequency than the original one. Thus the molecule enters a lower vibrational state while a more energetic photon is created: it corresponds to the anti-Stokes scattering. Because of thermal equilibrium, the vibrational states of the molecule are populated according to the Boltzmann statistics hence the higher vibrational states are less populated than lower ones i.e. the higher the vibrational state the least populated. Therefore, the anti-Stokes part of the spectrum is typically less probable to be observed experimentally as it needs the molecule to be in a higher vibrational state than the Stokes Raman scattering resulting in a lower intensity. Speaking of intensity, spontaneous Raman effect is very weak compare to 1 photon fluorescence with cross section of 10^{-30}cm^{-2} and 10^{-16}cm^{-2} respectively [30]. Thus, spontaneous Raman has limited applications in imaging because it is a much more challenging contrast mechanism.

1.2.3 Coherent Raman scattering

Spontaneous Raman has a very weak signal compare to 1 photon fluorescence, but in 1962 — shortly after the invention of the first lasers (1960) — a much more intense Raman effect was discovered [31]: coherent Raman scattering was accidentally discovered and more precisely what we call Stimulated Raman Scattering (SRS) nowadays. Nevertheless, spontaneous Raman was for long the only Raman scattering effect used in practice and no imaging technique was using these coherent signals. Indeed, in the following decades after its discovery, SRS was used for spectroscopy purposes and it is only in 2007 after Poletz's paper [32] that it was truly used for imaging purposes. In parallel, Coherent Anti-Stokes Raman scattering (CARS) was discovered in 1965 by Maker and Terhune [33]. Similarly to SRS, it was used for spectroscopy, but, even though it was discovered a few years after SRS, CARS was used first as a signal for imaging since its detection scheme is less complex. In 1982 Duncan et al. [34] managed to obtain CARS images of onion slices but it is only in 1999 that Zumbusch et al. developed the modern way of generating CARS signal [35] i.e. co-propagating beams tightly focused. Another difference between spontaneous and coherent Raman scattering is that the spontaneous process leads to emission in the form of a dipole radiation pattern, whereas the coherent process leads to emission in a well defined directions (that are dictated by the excitation and scattering center geometries). In addition to directional emission, coherent process increases the rate of photon emission drastically. Overall, these features of coherent emission further improve the ability to do fast imaging since more photon can be collected in a finite sized detector.

Coherent Raman processes are nonlinear optical effects meaning that they appear when the electric field becomes large compared to the intra-molecular field. This is the reason why the discovery of lasers triggered so many discoveries in the field of nonlinear optics since most of them were discovered between 1960 and 1965. To understand the physics of coherent Raman processes, we will derive a simple damped harmonic oscillator model driven by an periodic force $F(t)$ and where x describes the position of the electronic cloud of the diatomic molecule:

$$\frac{d^2x}{dt^2} + 2\gamma\frac{dx}{dt} + \Omega_R^2 x = \frac{F(t)}{\mu} \tag{1.4}$$

where $\mu = \frac{m_1 m_2}{m_1+m_2}$ is the reduced mass of the system. Using complex notation for $F(t) = F_0 e^{-i\omega t}$ where F_0 is the amplitude of the force $F(t)$, $x(t) = x(\omega)e^{-i\omega t}$ and inserting them in (1.4) near resonance and with a small damping factor ($\gamma \ll \Omega_R$) we get:

$$x(\Omega) \simeq \frac{1}{2\mu\Omega_R}\ \frac{-F_0}{(\Omega - \Omega_R) + i\gamma} \tag{1.5}$$

where $\Omega = \omega_p - \omega_S$ is the beating frequency of the Pump and Stokes laser fields respectively. Now, let's express the force $F(t)$ resulting from two incoming fields on the system, here a diatomic molecule [24]:

$$F(t) = \frac{dW}{dx} = \epsilon_0 \frac{\partial \alpha}{\partial x}\bigg|_{x_0} \Big[A_p A_S^* e^{i(Kz-\Omega t)} + C.C.\Big] \tag{1.6}$$

where W is the energy to create an oscillating dipolar moment, $K = k_P - k_S$ and $C.C.$ is the complex conjugate. Thus, inserting equation (1.6) into (1.5) we get:

$$x(\Omega) \simeq \frac{\epsilon_0}{2\mu\Omega_R} \frac{\partial \alpha}{\partial x}\bigg|_{x_0} \frac{A_p A_s^*}{(\Omega - \Omega_R) + i\gamma} \tag{1.7}$$

In this simplified model, when $\Omega = \Omega_R$, the vibration of the molecule becomes large which induces a nonlinear response of the molecule and more precisely nonlinear polarization of the molecule. From the formulae (1.7), we derive the nonlinear polarization which leads us to the four different coherent Raman processes that we will explore more in depth in the next sections. For a molecular density N in the medium and using equations (1.1) and (1.2), we derive the general polarization which is composed of linear and a nonlinear term:

$$\begin{aligned} P(z,t) = Np(z,t) &= N\epsilon_0 \Big[\alpha_0 + x(z,t)\frac{\partial \alpha}{\partial x}\bigg|_{x_0}\Big] E(z,t) \\ &= P^L + P^{NL} \end{aligned} \tag{1.8}$$

where $E(z,t) = A_p e^{i(k_P z - \omega_P t)} + A_S e^{i(k_S z - \omega_S t)} + C.C.$, P^L the linear polarization, P^{NL} the nonlinear polarization. Further expanding this expression leads to 4 different

nonlinear polarizations that radiate at 4 different frequencies:

$$
\begin{aligned}
P^{NL}(z,t) = & \underbrace{N\epsilon_0 \frac{\partial \alpha}{\partial x}\bigg|_{x_0} x(\Omega) A_P e^{i(2k_P - k_S)z} e^{-i(2\omega_P - \omega_S)}}_{Coherent\ Anti-Stokes\ Raman\ Scattering\ (CARS)} + \\
& \underbrace{N\epsilon_0 \frac{\partial \alpha}{\partial x}\bigg|_{x_0} x(\Omega)^* A_S e^{i(2k_S - k_P)z} e^{-i(2\omega_S - \omega_P)}}_{Coherent\ Stokes\ Raman\ Scattering\ (CSRS)} + \\
& \underbrace{N\epsilon_0 \frac{\partial \alpha}{\partial x}\bigg|_{x_0} x(\Omega) A_S e^{ik_P z} e^{-i\omega_P}}_{Stimulated\ Raman\ Loss\ (SRL)} + \\
& \underbrace{N\epsilon_0 \frac{\partial \alpha}{\partial x}\bigg|_{x_0} x(\Omega)^* A_P e^{ik_S z} e^{-i\omega_S}}_{Stimulated\ Raman\ Gain\ (SRG)}
\end{aligned}
\tag{1.9}
$$

These 4 nonlinear signals happen simultaneously on different regions of the spectrum and each has its own pros and cons that we will develop further in the next sections. However, we will not study the CSRS since it radiates in the infrared for the wavelength we use and the detector in that region of the spectrum are noisy and not suitable for our applications.

Stimulated Raman Scattering

Here we will study the specific features and explore more in depth the stimulated Raman scattering (SRS) which is subdivided in two processes that are interdependent: the stimulated Raman Gain (SRG) and Stimulated Raman Loss (SRL) processes. Most of the derivations will be skipped and the reader can refer to Boyd 2008 [24] or the tutorial by Rigneault et al. [23] for a more complete derivation.

The molecule reaches the vibrational excited state by the beating of the Pump and Stokes beams and then coherently converts a Pump shifted photon into a Stokes shifted photon while going back to the ground state as is depicted in Fig.1.10.a. First, we define the nonlinear susceptibilities based on the induced polarization :

$$P_{NL}(\omega_P) = 6\epsilon_0 \chi_R^{(3)}(\omega_p) |A_s|^2 A_p e^{ik_P z} \tag{1.10a}$$

$$P_{NL}(\omega_S) = 6\epsilon_0 \chi_R^{(3)}(\omega_s) |A_S|^2 A_s e^{ik_S z} \tag{1.10b}$$

where $\chi_R^{(3)}(\omega_P)$ and $\chi_R^{(3)}(\omega_S)$ are the third order nonlinear susceptibilities of SRG and SRL respectively. It is a tensor describing the interaction between the medium and incoming Pump and Stokes fields. As it can be noted from the two above equations, the two induced polarizations oscillate at the same frequencies as the incoming beam.

Hence, it means that the nonlinear signal will be measured on top of the incoming field. Moreover, there are coherently generated meaning that they can interfere with the strong incoming field. Using this we can derive expression for the intensities of both SRG and SRL at resonance that highlight the link between the two processes:

$$I^{SRL} \propto \left|A_P + A_P^{(3)}\right| \propto \left|A_P\right|^2 + \left|A_P A_P^{(3)}\right| \cos(\pi) \propto I_P - 2\sqrt{I_P I_P^{(3)}} \tag{1.11a}$$

$$I^{SRG} \propto \left|A_S + A_S^{(3)}\right| \propto \left|A_S\right|^2 + \left|A_S A_S^{(3)}\right| \cos(0) \propto I_S + 2\sqrt{I_S I_S^{(3)}} \tag{1.11b}$$

where $A_S^{(3)}$ and $A_P^{(3)}$ are the amplitudes of the induced fields. As it can be seen from the aforementioned equations, the names Raman loss and stimulated Raman Gain originate from depletion experienced by the Pump beam and the gain experienced by the Stokes beam.

Now if the interaction takes place in a nonlinear medium of length L, by using the following propagation equations:

$$\frac{\partial A_P}{\partial z} = \frac{i\omega_P}{2n_P\epsilon_0 c} P(\omega_P) e^{-ik_p z} \tag{1.12a}$$

$$\frac{\partial A_S}{\partial z} = \frac{i\omega_P}{2n_s\epsilon_0 c} P(\omega_P) e^{-ik_s z} \tag{1.12b}$$

And inserting the nonlinear polarization we get:

$$\frac{\partial A_p}{\partial z} = 3\frac{i\omega_p}{n_p C}\chi_R^{(3)}(\omega_p)|A_s(z)|^2 A_p(z) \underbrace{e^{i\Delta k z}}_{Phase\ matching} \tag{1.13a}$$

$$\frac{\partial A_s}{\partial z} = 3\frac{i\omega_s}{n_s C}\chi_R^{(3)}(\omega_s)|A_p(z)|^2 A_s(z) \underbrace{e^{i\Delta k z}}_{Phase\ matching} \tag{1.13b}$$

where Δk is the phase matching term. In the case of SRS, the phase matching requirement is always met since $\Delta k = \Delta\vec{k}\cdot\vec{e}_z = \left[(\vec{k_P} - \vec{k_P}) + (\vec{k_S} - \vec{k_S})\right]\cdot\vec{e}_z = \vec{0}$. In the context of microscopy, it is very convenient for a nonlinear signal to always be in phase at any distance in a medium. With the assumption that neither the Pump nor the Stokes are depleted and $\chi_R^{(3)} = \chi_R^{(3)}(\omega_P) = \chi_R^{(3)}(\omega_S)^* = \Re\left(\chi_R^{(3)}\right) + i\Im\left(\chi_R^{(3)}\right)$ we further derive the expression for the fields:

$$A_P(L) = A_P(0) exp\Big[-\frac{3\omega_P}{n_P c}\Im\left(\chi_R^{(3)}\right)|A_S(0)|L\Big] exp\Big[\frac{3\omega_P}{n_P c}\Re\left(\chi_R^{(3)}\right)|A_S(0)|L\Big] \tag{1.14a}$$

$$A_S(L) = A_S(0) exp\Big[+\frac{3\omega_S}{n_S c}\Im\left(\chi_R^{(3)}\right)|A_P(0)|L\Big] exp\Big[\frac{3\omega_S}{n_S c}\Re\left(\chi_R^{(3)}\right)|A_P(0)|L\Big] \tag{1.14b}$$

From these equations we can observe that the imaginary part of $\chi_R^{(3)}$ is the relevant quantity for the amplitude loss and gain. On the other hand, the real part is inducing

a refractive index change that is known as crossed phase modulation (XPM) which can induce focusing and defocusing effects by one beam on the another and lead to a small non resonant background [36]. In microscopy, the length L is generally small and it is possible to perform a first order development:

$$\Delta I_P(L) = -\frac{3\omega_P L}{2n_P n_S \epsilon_0 c^2} \Im\left(\chi_R^{(3)}\right) I_S(0) I_P(0) \tag{1.15a}$$

$$\Delta I_S(L) = +\frac{3\omega_S L}{2n_P n_S \epsilon_0 c^2} \Im\left(\chi_R^{(3)}\right) I_S(0) I_P(0) \tag{1.15b}$$

These equations are linked by $\Delta I_P = \frac{\omega_S}{\omega_P} \Delta I_S$ showing better the energy transfer between the Pump beam into the Stokes beam. These two equations will be the ones we will use later in chapter 3 to derive a forward model for the super resolution imaging technique.

Coherent Anti-Stokes Raman Scattering

To improve even further the transverse spatial resolution, it is better to use CARS signal. Hence, we will go through the theory of CARS signal to understand the core principles and what are the important features to take into consideration when using it for super resolution experiments.

Here we will study the specific features and the fundamental derivation of CARS physics. Similarly as in the previous chapter, most of the derivations will be skipped and the reader could refer to Boyd 2008 [24] and the tutorial by Rigneault [23].

Similarly to SRS, the beating between the Pump and Stokes beams promotes the molecule into the excited vibrational state corresponding to the resonant frequency Ω_R. It is then probed by the Pump beam and generates a scattered photon with the energy $\hbar\Omega_{AS}$ (see Fig.1.10.c.). There is an important difference with SRS though. In fact, there is a possibility to generate the same photon energy $\hbar\Omega_{AS}$ with a different route (see Fig.1.10.d.) thus creating a parasitic signal which is called non resonant background. Indeed, this route does not resonate with the vibrational excited state of the molecule but rather an instantaneous electronic response of the medium.

Now let us explore more the derivation of the CARS signal and observe its main features. First of all, for a totally polarized Raman line and with Pump and Stokes beams propagating along the z direction with the same linear polarization we can write the nonlinear polarization as follow :

$$P(\omega_{AS}) = 3\chi^{(3)} A_P^2 A_S^* e^{i(2k_P - k_S)z} \tag{1.16}$$

where $\chi^{(3)}$ is the overall susceptibility and can include a non negligible non resonant

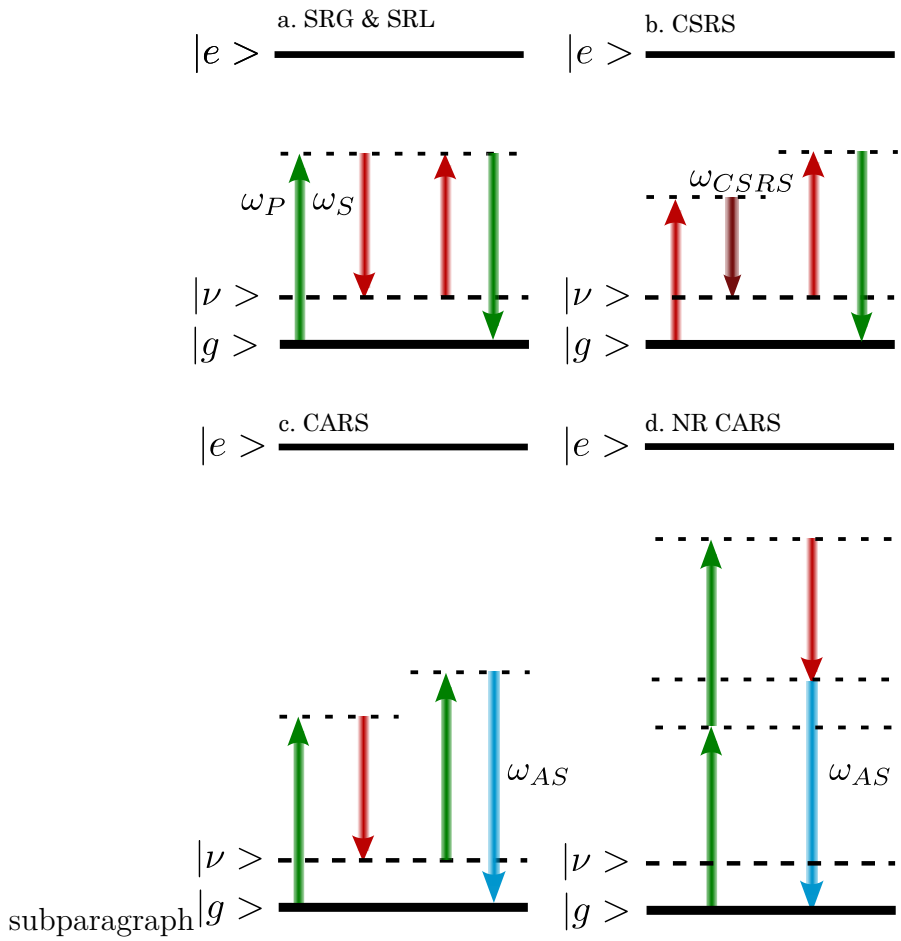

Figure 1.10: **Energy diagrams for coherent Raman scattering processes**. $|g\rangle$, $|\nu\rangle$ and $|e\rangle$ are respectively the ground state, vibrational state and excited state of the molecule. Dashed line represents virtual state of the molecule. **a.** Stimulated Raman Gain (SRG) and Stimulated Raman Loss (SRL) **b.** Coherent Stokes Raman Scattering (CSRS) **c.** Coherent Anti-Stokes Raman scattering (CARS) **d.** Non Resonant CARS background (NR CARS) ω_P, ω_S, ω_{CSRS} and ω_{AS} are respectively the Pump, Stokes, CSRS and CARS angular frequencies.

term as we will see at the end of this section. Similarly as in section 1.2.3, we study the anti-Stokes field generation and propagation under the slowly varying envelope approximation. The anti-Stokes field propagation and equation (1.16) give:

$$\frac{\partial A_{AS}}{\partial z} = \frac{3i\omega_{AS}}{2n_{AS}c}\chi^{(3)}(\omega_{AS})A_P^2 A_S^* \underbrace{e^{i\Delta kz}}_{Phase\ \ matching} \tag{1.17}$$

where A_{AS} is the amplitude of the anti-Stokes field $E_{AS} = A_{AS}e^{i(k_{AS}z-\omega_{AS}t)} + C.C.$ and $\Delta k = \Delta\vec{k}\cdot\vec{e}_z = (2\vec{k}_P - \vec{k}_S - \vec{k}_{AS})\cdot\vec{e}_z$.

The field propagates in a medium of length L then :

$$I_{AS}(L) \propto |\chi^{(3)}(\omega_{AS})|^2 L^2 \mathrm{sinc}^2\Big(\frac{\Delta kL}{2}\Big) I_P^2 I_S \tag{1.18}$$

Contrary to SRS, we can note that the phase matching condition is not always met. Thus, the CARS signal is efficiently generated only if $\sin^2$ is close to 1 which means $\frac{\Delta kL}{2\pi} \ll 1$. Indeed, since CARS is a coherently generated signal, the emitters need to interfere constructively along the z direction and any emitter out of phase will damage the CARS signal. When it comes to CARS microscopy imaging though, since the beam are tightly focused, a broad angular spectrum of wave vector $\vec{k}$ open the possibility for many combination to meet the phase matching condition. Furthermore, since the beams are tightly focused the excitation volumes are extremely small so "L" is very small and thus the condition $\frac{\Delta kL}{2\pi} \ll 1$ can be met.

The other main difference between SRS and CARS is the non negligible non resonant background. As can be seen in Fig.1.10.d., there is another route to generate a photon energy $\hbar\omega_{AS}$. Hence, the emitted CARS signal has two origins : a resonant signal at Ω_R with susceptibility $\chi_R^{(3)}$ and a non resonant signal with susceptibility $\chi_{NR}^{(3)}$ which is a pure real non resonant signal and not originating from an electronic transition. Thus we derive the following equation for the CARS signal:

$$\begin{aligned} I_{AS} &\propto \Big|\chi_R^{(3)} + \chi_{NR}^{(3)}\Big|^2 \\ &\propto \underbrace{\Big|\chi_R^{(3)}\Big|^2}_{Resonant\ term} + \Big|\chi_{NR}^{(3)}\Big|^2 + \underbrace{2\chi_{NR}^{(3)}\Re\Big(\chi_R^{(3)}\Big)}_{cross\ term} \end{aligned} \tag{1.19}$$

Since one would want to have access to the resonant contribution, the most interesting are the resonant and cross terms. Indeed, this would enable to obtain quantitative data of the chemical present in the media. However, as it is shown in Fig.1.11. the CARS spectrum is distorted and shifted compared to the standard Raman spectrum. In fact, we can note that the peak intensity of the CARS signal is blue-shifted and this shift depends on the non resonant signal thus obscuring the quantitative interpretation of any spectrum. In chapter 4, we will explore means to tackle this issue and remove these artifacts from CARS imaging techniques.

1.3 Super resolution imaging

The diffraction limit is a physics fundamental limit that prevents to spatially distinguish two distinct objects and it will defined more precisely in the next section. In this manuscript, every technique that enables to go beyond the diffraction limit is called a super resolution method whether the achieved super resolution still depends on the diffraction limit (SIM: 2x the diffraction limit) or not (PALM, STORM: precision of

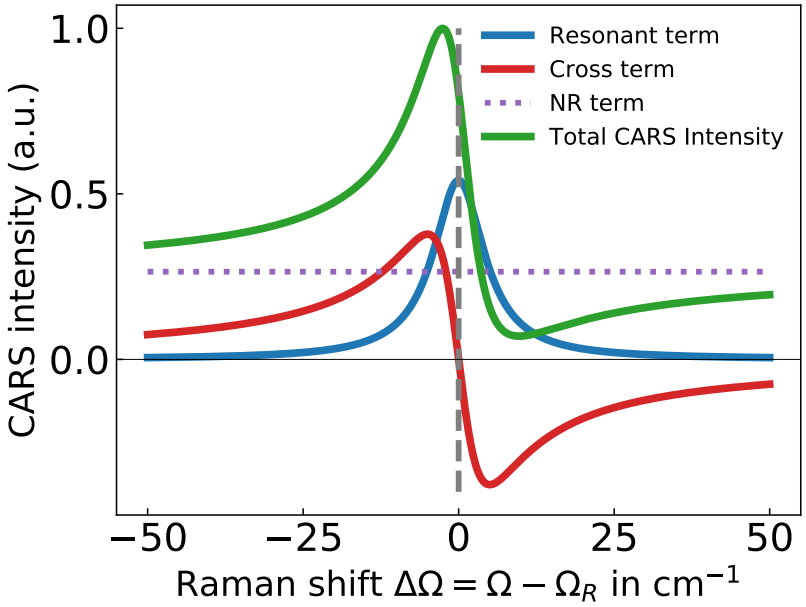

Figure 1.11: **Simulation of non resonant background effect on CARS signal**. In this simulation, $\chi_R = \frac{a}{(\Omega-\Omega_R)+i\gamma}$ where $a = 1$, $\chi_{NR} = 0.14$ and $\gamma = 5\ cm^{-1}$

localization). It was long thought that the diffraction limit would never be overcome. In the nineteenth century, several eminent scientists including Abbe and Helmholtz stated that the far-field resolution limit for an optical system is limited to $\frac{\lambda}{2NA}$. And only at the end of the twentieth century, the super resolution race started after the work from Pohl et al. [37] who made an experiment similar to an idea proposed by Synge in 1928 [38] who was himself encouraged by Albert Einstein. He proposed a miniature aperture (10^{-6}cm) illuminated from below with intense light and placed very close to the specimen under study. He claimed that it could reach resolution down to 10nm and Pohl et al. used the same principle to demonstrate near-field scanning optical microscopy (NSOM) where they managed to resolve detail down to $\frac{\lambda}{20}$ instead of $\frac{\lambda}{2.3}$ for a conventional microscope. NSOM is a label-free technique that has played a key role in the race toward super resolution technique. However, it can only offer surface imaging which is limiting for most biological applications. Indeed, it is still a near-field microscopy technique but it proved that something was possible. Following this achievement, the first demonstrations of far-field super resolution were focused on axial super resolution (4π confocal microscope [39, 40, 41], I^5M and inspirations [42, 43, 44]) but with poor transverse resolution improvements. In the 1994, it was the first transverse super resolution method where Hell et al. [45] proposed a new type of scanning microscopy that overcame the diffraction limit. The idea consisted in employing a stimulated emission depletion (STED) to inhibit the fluorescence process in outer regions of the excitation PSF thus reducing the effective volume of the PSF

and it was first shown experimentally by Klar et al. in 1999 [46]. It paved the way for other super resolution techniques that have developed until now such as PhotoActivated Localization Microscopy (PALM) [47, 48], STochastic Optical Reconstruction Microscopy (STORM) [49] and led to the 2014 Nobel Prize in Chemistry awarded jointly to E. Betzig, S.W. Hell and W.E. Moerner for their pioneering work in super resolution microscopy.

1.3.1 Origin of diffraction-limited resolution

Before the pioneering work that started in the 1980s from several scientists in the field and the 2014 Nobel prize, the diffraction limit was established as an unbeatable limit. Indeed, this limit arises from wave propagation that can be seen as a low-pass filter for the spatial frequencies carried by the emitted beam and also the imaging system is itself a low-pass filter for spatial frequencies. Let us see the derivation of the wave equation that lead to this fundamental limit. Starting with the wave equation:

$$\left(\nabla^2 - \frac{1}{c^2}\frac{\partial^2}{\partial t^2}\right)E(\mathbf{r},t) = 0 \tag{1.20}$$

where $E(\mathbf{r},t) = A(\mathbf{r})e^{i\omega t}$ is the electromagnetic field by using the separation of variable technique [50]. We derive equation 1.20 and get two equal fractions depending on two independent variables which implies that the ratios are equal to a constant that we call $-k^2$ without loss of generality:

$$\frac{\nabla^2 A(\mathbf{r})}{A(\mathbf{r})} = \frac{1}{c^2 e^{i\omega t}}\frac{d^2(e^{i\omega t})}{dt^2} = \ Constant \ = -k^2 \tag{1.21}$$

Thus, we obtain the two following equations called the Helmholtz equation and the dispersion relation:

$$\begin{cases} \nabla^2 A(\mathbf{r}) + k^2 A &= 0, \text{ Helmholtz equation} \\ k^2c^2 - \omega^2 &= 0, \text{ Dispersion relation} \end{cases} \tag{1.22}$$

Again, using the principle of separable variable but this time in Cartesian orthogonal coordinates $(\vec{u_x}, \vec{u_y}, \vec{u_z})$ we can solve the Helmholtz equation with $A(\mathbf{r}) = A_x(x)\cdot A_y(y)\cdot A_z(z)$:

$$\frac{\frac{d^2A_x(x)}{d^2x}}{A_x(x)} + \frac{\frac{d^2A_y(y)}{d^2y}}{A_y(y)} + \frac{\frac{d^2A_z(z)}{d^2z}}{A_z(z)} + k^2 = 0 \tag{1.23}$$

where each ratio is equal to a constant denoted $-k_i^2$ with $i = x, y \ or \ z$. This leads

to the following system of equations:

$$\begin{cases} \frac{d^2A_x(x)}{d^2x} + k_x^2 & = 0 \\ \frac{d^2A_y(y)}{d^2y} + k_y^2 & = 0 \\ \frac{d^2A_z(z)}{d^2z} + k_z^2 & = 0 \\ k_x^2 + k_y^2 + k_z^2 & = k^2 \end{cases} \tag{1.24}$$

Finally, the solution for the above system can be written in a complex exponential form:

$$\begin{aligned} A(x,y,z) =& Ue^{ik_xx}e^{ik_yy}e^{ik_zz} \\ =& Ue^{i(k_xx+k_yy)} \underbrace{e^{\pm iz\sqrt{k^2-k_x^2-k_y^2}}}_{key\ for\ diffraction\ limit} \end{aligned} \tag{1.25}$$

In this last equation, the term $e^{\pm iz\sqrt{k^2-k_x^2-k_y^2}}$ is an exponential decay for spatial frequencies such that $k_F^2 = k_x^2 + k_y^2 > k^2$. When the above condition is met, the wave exponentially decays — evanescent waves — as it propagates so that high frequencies are only available near the emitter which is the key reason why near-field microscopy is not limited by diffraction while far-field microscopy is. The propagation of light can be seen as a low pass-filter for spatial frequencies. And for $k_F^2 < k^2$, the resolution is limited by the imaging system and more precisely the amount from this propagating spherical wave that is emitted it can catch. Hence imaging systems act as a spatial frequency low pass filter whose cutting frequency depends on the NA of the objective, that is why microscopy needs high NA objectives resolution at fixed wavelength for better resolution.

1.3.2 Background on STED imaging

Microscopy is often inspired from astronomy but one of the main difference is the ability of microscopist to alter and engineer the source and the illumination part of their inventions. Indeed, since the beginning of imaging, the illumination pattern used to shine a sample has always been one of the main tool at our disposal. In 1900s, when illuminating a sample with an halogen lamp, the filament of this lamp would be imaged onto the sample. But back in 1893, August Köhler invented the Köhler illumination principle so that at the sample plane the illumination is homogeneous and this technique has been the backbone of optical microscope. In the last decades, the illumination pattern has been extensively structured in different ways to extend the capabilities of modern microscopes.

In the case of STED, the illumination is engineered such that fluorophores are se-

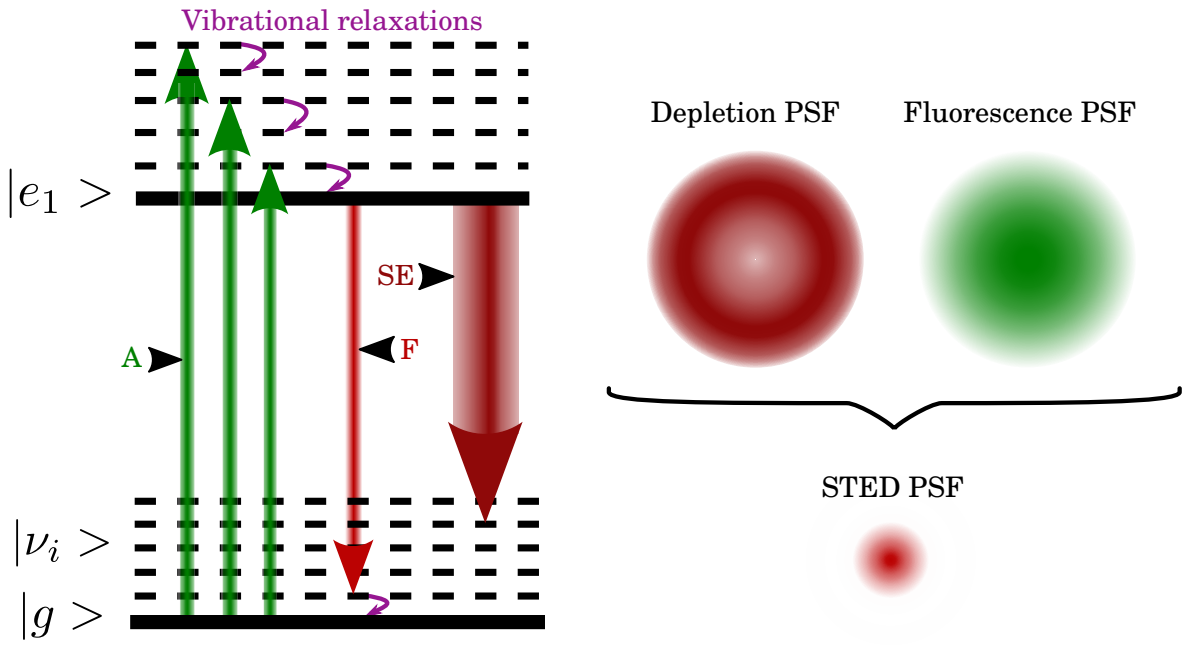

Figure 1.12: **STED Jablonski diagram**. $|g\rangle$, $|\nu_i\rangle$ and $|e\rangle$ are respectively the ground state, vibrational states and excited state of the molecule. A, F, SE respectively stand for absorption, fluorescence emission and stimulated emission.

lectively deactivated in the outer part of the PSF of the imaging beam. More precisely, STED consist in two beams which are overlapped and copropagating with one selectively deactivating fluorophores and the other beam is the imaging beam. To deactivate the fluorophores, the beam wavelength is tuned such that electron in the excited states are stimulated to de-excite into a high vibrational state of the electronic ground state (see Fig.1.12). Thus, the stimulated photon is red shifted compared to a regular fluorescence photon. Fluorescence photon are then selectively filtered to be detected by the single photon sensitive detector.

Then, the deactivation beam is spatially shaped into a doughnut by using diffractive optical element such as an optical vortex in combination with a circular polarization. However, the depletion beam needs to be powerful enough to enhanced the resolution and S. Hell developed the following formulae [45]:

$$\Delta r = \frac{\lambda}{2NA\sqrt{1 + I/I_S}} \tag{1.26}$$

where I_S is the saturation intensity of the fluorophores. In fact, to deplete efficiently the stimulated emission has to win the competition with the spontaneous emission which happens at nanosecond scale after excitation. For instance, to switch off half of the fluorophores with a 4 ns excited-state lifetime and 25 cm^2/J stimulated emission cross-

section requires 10 MW/cm^2 light intensity (saturation intensity) [51]. We clearly see that there it needs a lot of power and there is a direct link between this high intensity illuminating the sample and the resolution.

1.3.3 Background on conventional SIM

Similarly to STED microscopy, SIM is based on clever way to illuminate the sample which generally consists in stripe pattern but the technique requires more computational involvement and is not only used for super resolution. In combination with computational techniques applied to the images, structured illumination has been able to provide to widefield microscope features such as optical sectioning, surface profiling, phase imaging or super-resolution while not requiring heavy modification and often being only a simple add-on onto a conventional microscopes (see Fig.1.13).

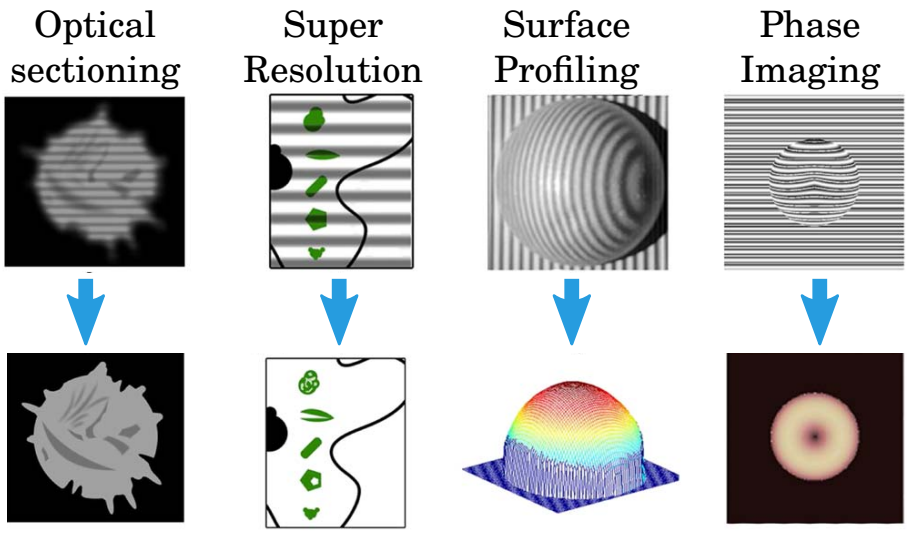

Figure 1.13: **Different use cases for SIM**. Top row represent raw images taken in respective technique and bottom row represents reconstructed images extracting the feature enable by the structured illumination. Image taken from [52].

In the following of the section, we will focus on structured illumination dedicated to super-resolution microscopy first by deriving a theoretical approach of the well known Structured Illumination Microscopy (SIM) and then we will introduce the more recent technique using less *a priori* information called blind-SIM.

In general, the image formation mechanism for any widefield microscope consist in shining a spatially varying distribution of photon sensitive element $\rho(\mathbf{r})$ with a light source of intensity $I(\mathbf{r})$ and then imaging the illuminated sample through an imaging

system of PSF $h(\mathbf{r})$ resulting in the following equation:

$$M(\mathbf{r}) = \Big(\rho(\mathbf{r}) \cdot I(\mathbf{r})\Big) \star h(\mathbf{r}) \tag{1.27}$$

where M is the observed image and $\star$ denotes the convolution operator.

The conventional super resolution SIM consists in shining a sample with stripe patterns that are limited by diffraction effects. The stripe pattern is generated by the interferences between two beams — usually split from the same source — and thus have a sinusoidal profile in one direction.

$$I(\mathbf{r}) = I_0(1 + \alpha \sin(2\pi k_0 \mathbf{r} + \phi)) \tag{1.28}$$

What is the effect of such a structured illumination pattern ? By using a Fourier transform of the PSF, we access the optical transfer function (OTF) of the system which has two components: the phase transfer function (PTF) and the modulation transfer function (MTF) which corresponds to the amplitude of the OTF and defines how well each frequencies are expressed in the image. The MTF support limits the maximal spatial frequency detectable — the passband — by the imaging system which is limiting the resolution of the image.

If we take equation (1.27) and go to the Fourier space, we can clearly see that some high frequencies of the object are down-modulated by k_0 into the "observable" frequencies meaning they now fall into the accessible spatial frequency domain of the imaging system characterized by h.

$$\tilde{M}(\mathbf{k}) = I_0 \tilde{h}(\mathbf{k}) \Big[\tilde{\rho}(\mathbf{k}) + \frac{\alpha}{2}\tilde{\rho}(\mathbf{k} - k_0)e^{i\phi} + \frac{\alpha}{2}\tilde{\rho}(\mathbf{k} + k_0)e^{-i\phi}\Big] \tag{1.29}$$

In the equation above, we can see that the first term corresponds to the frequency spectrum of a spatially unmodulated illumination while the second and third terms correspond to spatially modulated illumination thus are shifted by $\pm k_0$ which explores the spatial frequency space bringing higher frequency content into the pass band of the imaging system. A raw image of one single sinusoidal pattern is a mix of these three terms and to separate the frequency information it is required to acquire 3 different phases in the same direction. Hence, it will be possible to computationally separate the distinct contributions to yield an extended detection frequency spectrum.

We can represent the MTF support as a circle where the low spatial frequencies are at the center and the higher frequency content is toward the edges of the circle, see Fig.1.14

To make sure the illumination of the object is homogeneous in real space, and that the Fourier space is well explored, 9 illumination patterns are needed. These 9 patterns are composed of 3 pattern with the stripes in the same direction but with 3 different phases to illuminated homogeneously in that direction and it is necessary to repeat

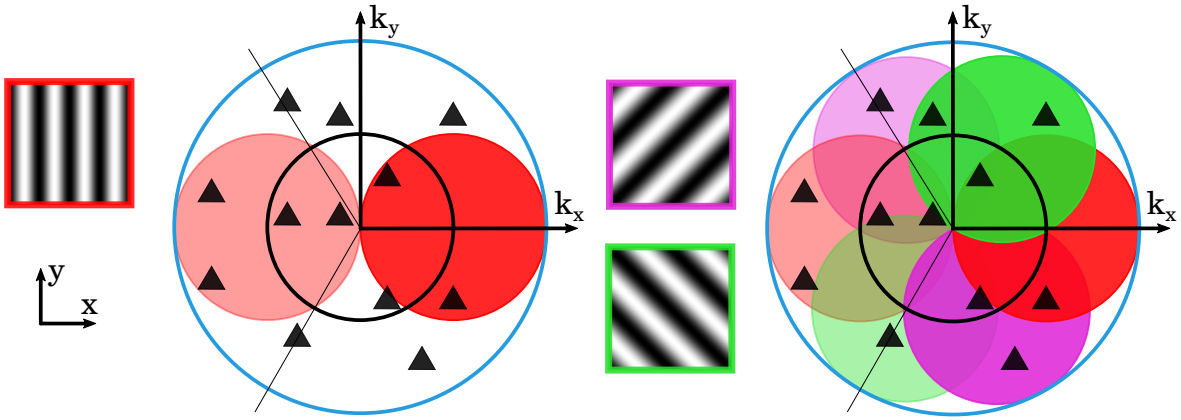

Figure 1.14: **Fourier plane representation of SIM**. Illustration of MTF support expansion through the use of structure illumination pattern. The radius of the circles correspond to $\frac{2NA}{\lambda}$ and are centered at a distance k_0 from the central circle whose direction depends on the direction of the stripes of the illumination patterns resulting in a doubling of the MTF support.

this operation for 3 different directions. It has been shown that this number can even be reduce to 4 patterns [53] and further speeds up the imaging speed capabilities.

Finally, SIM is able to achieve diffraction limited super resolution (2× below diffraction limit) independent of the power used to illuminate the sample contrary to STED which needs high laser power to achieve depletion of the given state (see equation 1.26). Indeed for STED, the greater the depletion laser intensity, the better the spatial resolution. This is problematic since it leads to higher probability of photobleaching. Moreover, the better the spatial resolution the smaller the focal volume of scanning which then implies higher spatial sampling rate thus decreasing the speed of the technique. For all the reasons aforementioned, the final chosen candidate to develop a label-free super-resolution technique is SIM over localization methods and STED-like methods. But the super-resolution SIM is very sensitive to phase changes from the material and artifacts can arise from scattering coming from the biological tissues when imaging opaque and/or deep inside tissues. Indeed, the illumination pattern needs to be well known by the algorithm to computationally reconstruct an image with as few as possible artifacts. To correct for that, some methods have been developed to actively correct the SIM pattern such as adaptive optics methods (AO) for SIM [54, 55, 56] or blind-SIM which we will develop in the next section.

1.3.4 Blind Structured Illumination Microscopy

As we developed in the previous section, SIM is a very flexible method to achieve label-free super-resolution. It does not scale with beam intensities which is relevant to avoid photodamage and thus it is interesting for biological imaging. Nevertheless, biological

tissues are generally scattering and it only increases as one would like to image deep inside tissues. One of the main requirement for SIM to work properly is that the pattern illuminating the sample is well-known and can be given to the reconstruction algorithm. Such a requirement is easy to achieve when the sample is optically thin and without scattering but it is unlikely to hold in biological tissues. It is possible to compensate for weak scattering effects with adaptive optics but it is only able to compensate for low order perturbations. Instead of actively correcting for it, it is possible to lower the requirements of the reconstruction algorithm and even use unknown patterns as illumination pattern: this is called blind-SIM which was first demonstrated in 2012 by Mudry et al. [57]. The principle is to replace the sinusoidal illumination by a speckle which naturally arises from biological tissues due to scattering (for more details on what a speckle is refer to 1.5.3). The price to pay for relaxing the requirement is to ensure an homogeneous illumination of the sample on average which consequently needs more than the 9 illumination patterns of SIM, we will develop more about this point in section 3.1.3. Indeed, it usually requires a few tens to several hundreds of images of different speckle realizations to ensure homogeneous illumination. Nevertheless, no sacrifice is made on the achievable spatial resolution and the experimental setup is greatly simplified since generating a speckle can be done by using just a diffuser or a spatial light modulator (SLM). No calibration step is required anymore and the method is insensitive to aberrations induced by the sample or the optics.

However, it is not enough to have a technique which is scattering resilient. Indeed, in biology most of the samples are 3D and one important feature a super-resolution technique would like to have is the ability to distinguish between different depths: this is called sectioning.

1.4 Label free super resolution

There is a high interest in studying biological specimen in their most natural environment and this also includes microscopy imaging. Indeed, one of the most broadly used imaging technique is fluorescence imaging but it requires markers that bind themselves to the molecule of interest. It can alter the standard behavior of the cells or whatsoever that is imaged and thus there is an increasing interest in label-free super resolution methods. As a consequence, all the techniques like PALM, FPALM, STORM and similar techniques that need engineered markers to switch on and off cannot be label free. It is the same for STED or RESOLFT [58] (reversible saturable optical fluorescence transitions) which generally use a fluorescence signal. It is possible to use autofluorescence STED techniques but it is limiting the number of substances that can be imaged and we seek here a more general principle to obtain super resolution in a label-free manner.

1.4.1 STED-like SRS imaging

Nevertheless, STED-like Raman approaches have been explored and successful at reaching super resolution without marker but only on very robust material like metals or glass but never on biological sample. Indeed, fluorescence based STED already uses a lot of power, and Raman signals are much less efficient than fluorescence signal. Consequently, the probability to induce photodamages to biological tissues is as much higher and it is probably not suitable for standard type of biological tissues. To illustrate this

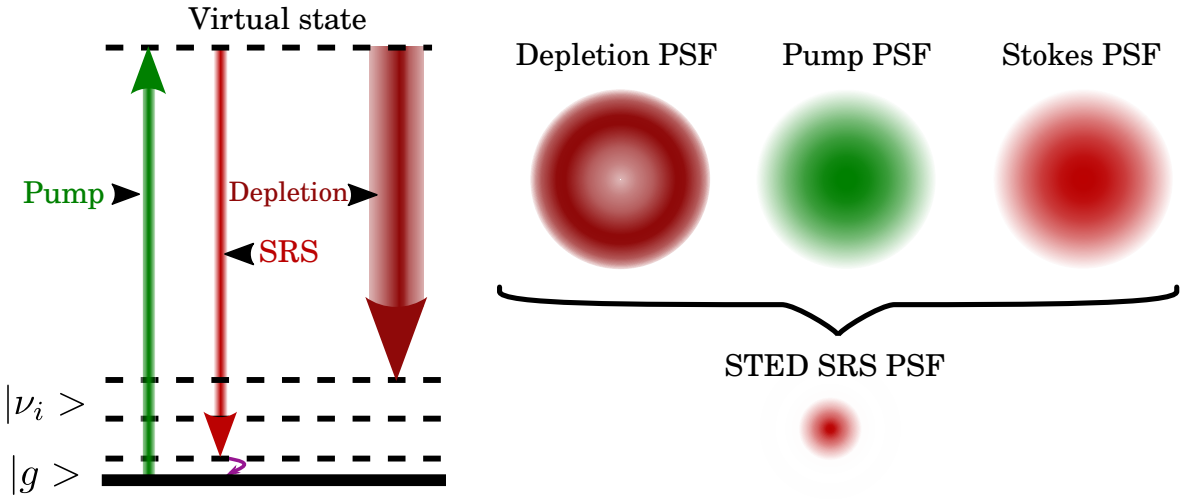

Figure 1.15: **STED SRG Jablonski diagram**. $|g\rangle$ and $|\nu_i\rangle$ are respectively the ground state, vibrational states of the molecule. Dashed line represents a virtual state that mediates the light matter energy exchange. Pump, Depletion and SRS respectively stand for Pump beam, depletion beam and SRS emission.

idea, Table 1.1 lists the works on Raman based label-free super resolution techniques. In the early 2010s, we can observe that most of the STED-like papers were theoretical suggestions and that overall not much has been done experimentally. Nonetheless, we can focus on two experimental realizations of STED-like SRS from Silva et al. [59] and Kim et al. [60]. Generally, these methods are playing with the coherence of 2 vibrational states corresponding to 2 Raman resonances as depicted in Fig.1.15. Similarly to STED fluorescence, a competition starts between the 2 vibrational states for populating the one which is not actively imaged with a doughnut shaped beam, the depletion beam.

In Fig.1.16.c., Silva et al. are effectively able to improve the resolution and reach resolution below the diffraction limit when the decoherence beam is on. A 1.6-1.7 resolution improvement is achieved compared to the reference measurement. But, they only performed 1D image perpendicular to the junction between glass and diamond as depicted in Fig.1.16.a. Indeed, the pixel dwell time for such measurement is on

the order of several seconds for each data point. Regarding the power, in addition to the regular SRG technique which uses 2 beams, a third beam with a density power of 20-33W/cm^2 as depletion beam. However, the source laser is only 1kHz of repetition rate so the energy per pulse is extremely high and very likely harmful for biological tissues. Furthermore, the objective that are used for this proof of principle have a much lower NA than the ones that are generally used for super resolution imaging. Indeed, a 0.25 and 0.4 NA are used here while it is more common to use water immersion or oil immersion objective with a NA$>$ 1.

Nevertheless, Silva et al. is the only paper doing imaging in a STED-like configuration while Kim et al. is more revolving around proving that it is possible to deplete the signal. In the work from Kim et al., they managed to reduce the depletion beam power required but the issues with STED-like approach remains the same (see Fig.1.17). They could not use high NA objective and the low NA that they use are underfilled (they use a NA$=$ 0.3 but effective NA$=$ 0.1), the repetition rate of the laser is 50Hz — even lower than Silva et al. — and consequently it is very likely harmful for biological tissues. In their follow-up paper [61], they elucidate more the physics at play and state that for higher NA objective it is near impossible to meet biological compatible powers. Indeed, the depletion effect is expected to be weaker since the higher NA means lower focal volume. They showed an efficiency of 64% with a NA$=$ 0.1 and estimate that for an objective of NA$=$ 1 the efficiency would drop to 0.5%. This low efficiency would produce very low resolution improvements unless a very high power is issued by the depletion beam. They are exploring new methods including the use of external media with higher Raman gain which would result in a non label-free method. Finally, the 3 beams required for the method are very sensitive to the alignment and the well defined beam shape for the depletion beam would not hold well in a scattering biological tissue.

For all the reasons mentioned here, we decided not to explore STED-like super resolution methods to reach label-free super resolution method for biological tissues.

1.4.2 SIM-like SRS imaging

There are now two super resolution techniques left: PSF engineering and SIM.

- PSF engineering consists in cleverly designing a phase mask that will shape the beams in the sample plane so that it improves the resolution. In the case of biological tissues, optical aberrations and scattering will modify the carefully design phase mask quickly as it propagates inside the medium and results in an different PSF than the engineered one without an active correction of the wavefront.

- Standard SIM which consists in illuminating the sample with known pattern. It has exactly the same issue as PSF engineering since it requires to know what

Ref	Method and mode SR	Theo. /Exp.	Theo Resolution/ nm	Exp.Super resolution/ nm	PDT /us	Energy	Year
Beeker [62]	STED-like CARS	Theo					2009
Beeker [63]	STED-like CARS	Theo					2010
Hajek [64]	SIM CARS	Theo					2010
Raghunathan [65]	PSF engineering	Theo					2010
Liu [66]	STED-like CARS	Theo					2011
Clef [67]	STED-like CARS	Theo					2012
Kim [68]	PSF engineering	Exp, no tissue	167	130			2012
Yavuz [69]	SIM CARS	Theo					2012
Gong [70]	STED-like SRS	Theo					2014
Gong [71]	STED-like SRS	Theo					2015
Yonemaru [72]	Saturated CARS	Exp, no tissue	174	DL/1.27 (Theo)	100		2015
Watanabe [73]	SIM spont Rman, C-H	Exp, 1D-only	218	DL/1.4 (Theo)	$7.5{\cdot}10^4$		2015
Silva [59]	STED-like SRS	Exp, no tissue	1370	930 (Exp)	2000		2016
Kim [60]	STED-like SRS	Exp, no tissue		No imaging			2017
Beams [74]	PSF engineering	Exp, no tissue	∼167	∼147			2017
Choi [75]	STED-like CARS	Exp, no tissue		No imaging			2018
Rao [76]	STED-like SRS	Theo					2018
Rao [77]	STED-like CARS	Theo					2018
Gong [78]	Saturated SRS, chlorophyl	Exp		255	0.4	>350 pJ	2019
Würthwein [79]	Saturated SRS	Exp, no tissue		DL/2		> 1nJ	2019
Lim [61]	STED-like CARS	Exp, no tissue		No imaging		1 nJ	2020
Xiong [80]	STED-like,Raman Fluorescence	Exp	331	180	1000	∼50 pJ	2021
Graefe [81]	STED-like SRS	Exp, no tissue	1760	1500	$3{\cdot}10^4$		2021

Table 1.1: **State of the art of far-field label-free super-resolution methods in Raman-based microscopy.**
STED-like means any process that exploits dynamics control beam, therefore using three-beam geometries (values are only quoted for resolution gain demonstrations). DL means diffraction-limit resolution. Theo, Exp, stands for theoretical and experimental demonstrations respectively.

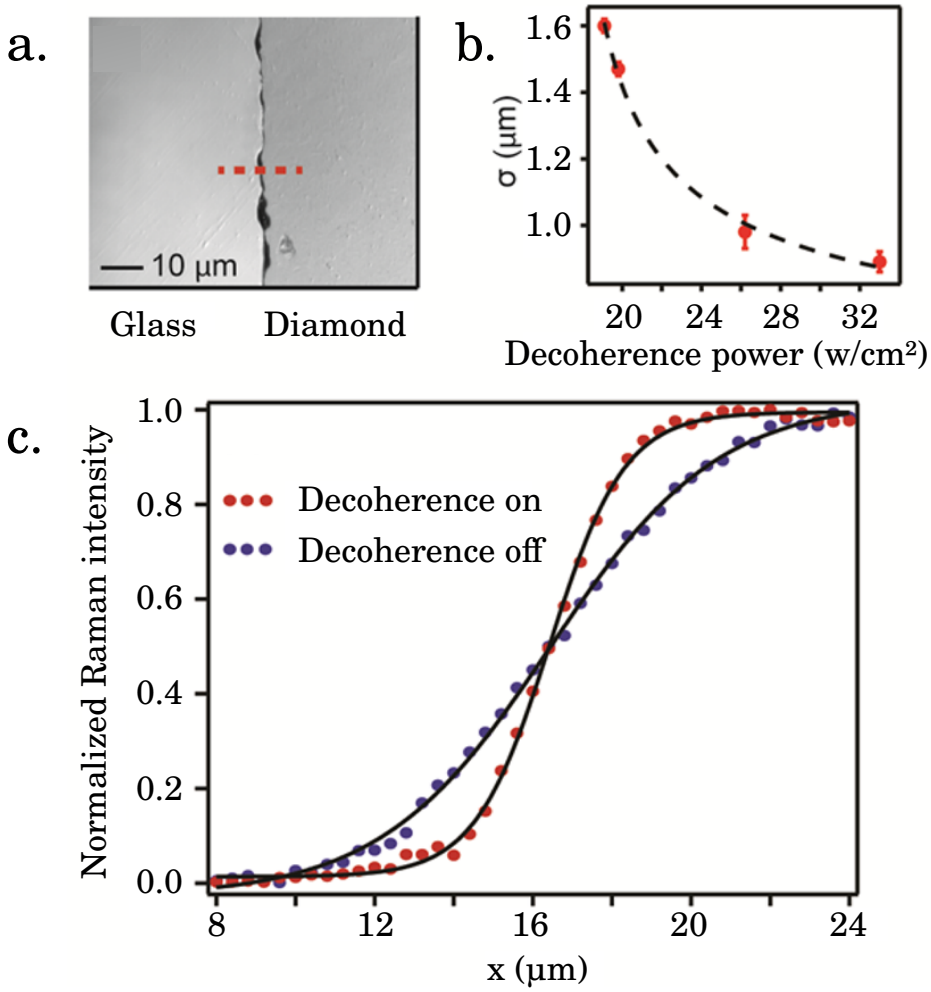

Figure 1.16: **Experimental demonstration of STED SRS by Silva et al.**. a. Optical microscope image of diamond plate. b. Spatial resolution improvement, represented as the fitted value from a sigmoidal curve, as a function of decoherence beam power. c. Line scan across diamond plate, showing clear improvement of resolution with the addition of the decoherence beam. It was taken with a 800 nm Raman Pump pulse with a power of 13.1 W/cm^2, an 800 nm decoherence beam with power of 33 W/cm^2, and a 2s acquisition time per point. A 20x objective with a numerical aperture of 0.40 was used for these scans. Adapted from [59]

pattern illuminated the sample in order to reconstruct an image without artifacts. Nevertheless, there is a method to ease this requirement that is called blind-SIM and will be introduced in the next section.

In the Table.1.1., we can see that SIM was proposed from the very beginning by Hajek et al. [64] and Yavuz et al. [69] in theoretical works. It is proposed a wide field illumination configuration using CARS signal since it is a higher nonlinear dependency in intensity and thus can reach higher resolution improvement. However, CARS mi-

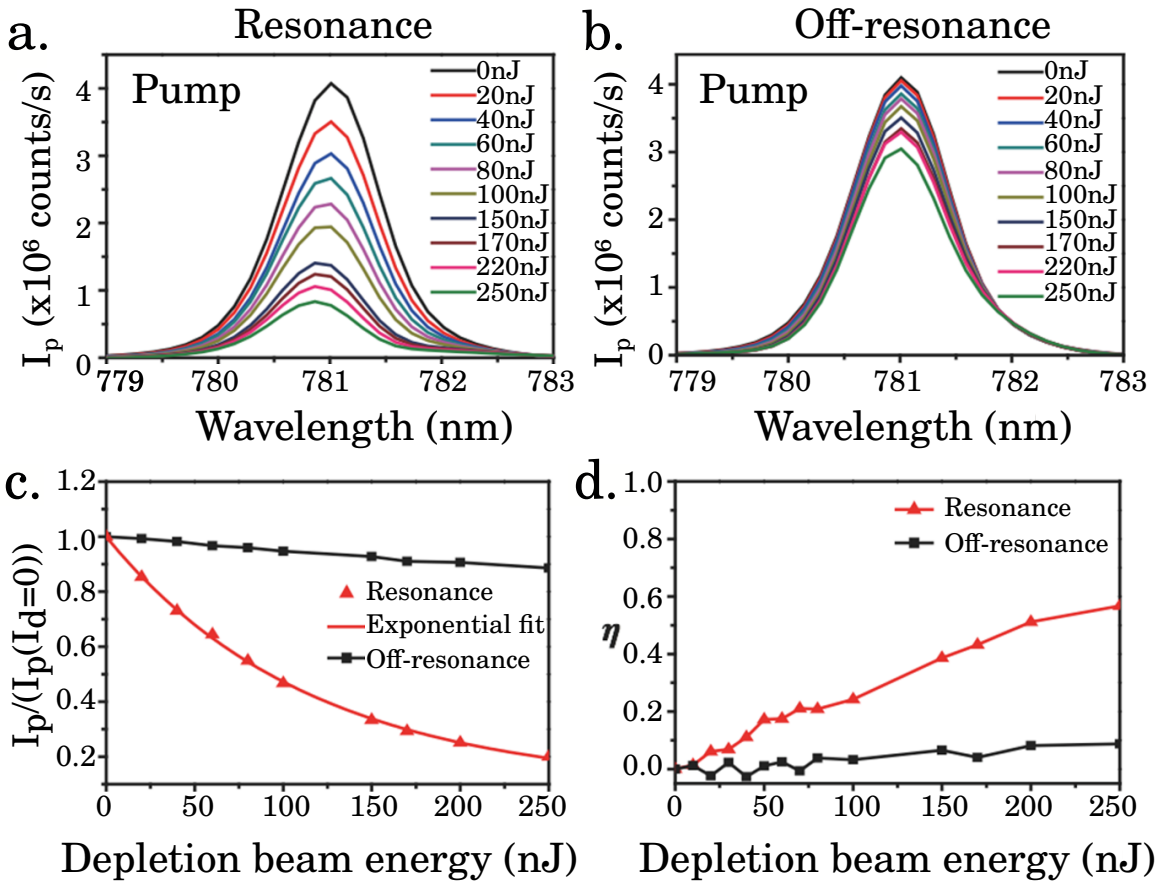

Figure 1.17: **Experimental demonstration of STED SRS by Kim et al.**. Resonant versus off-resonant conditions. a.b. Pump pulse spectra transmitted through pure benzene liquid with 0-250 nJ depletion pulse energy at the resonant a. and off-resonant b. conditions. c. Integrated Pump beam intensities at the resonant (red) condition in panel a. and the off-resonant (black) condition in panel b. plotted with respect to the depletion pulse energies. The data in the resonant condition are well-fitted with a single-exponential function with decay constant of 114.5 nJ. d. SRG suppression efficiencies under the resonant (red) condition and off-resonant (black) condition. Adapted from [60]

croscopy is a scanning point configuration method because of its nonlinear nature and that is probably why no experimental demonstration has been achieved thus far. On the experimental side, Watanabe et al. [73] managed to achieve truly label-free super resolution using SIM in spontaneous Raman with a high NA objective (NA= 1.27, water immersion). They implemented structured line illumination in slit-scanning Raman microscopy where a line-shaped focus illuminates the sample and scanning in one axis produces a two-dimensional (2D) Raman image. However, it takes between 5 to 10 seconds to image one line of the image and from 1 to 2 hours for the complete images

shown in Fig.1.18. In this structured-line-illumination (SLI) approach, the resolution improvement happens only in one direction unless the sample or the line-scanning are rotated by 90° thus doubling the acquisition time. Similarly to confocal imaging, the out of focus signal rejection is present but the effective signal is already so weak and the acquisition time so long that the slit cannot be further closed and the sectioning is weak. Watanabe et al. managed to perform label-free super resolution imaging on biological samples such as mouse brain (see Fig. 1.18) proving that Raman SIM was achievable in biological tissues while offering spectroscopic capabilities.

To conclude, the most favorable technique to do label-free super resolution imaging with chemically selective signal like Raman effects seems to be SIM because of its high versatility, the independence of the super resolution ability on intensity of the excitation beams and compatibility with spectroscopic measurement.

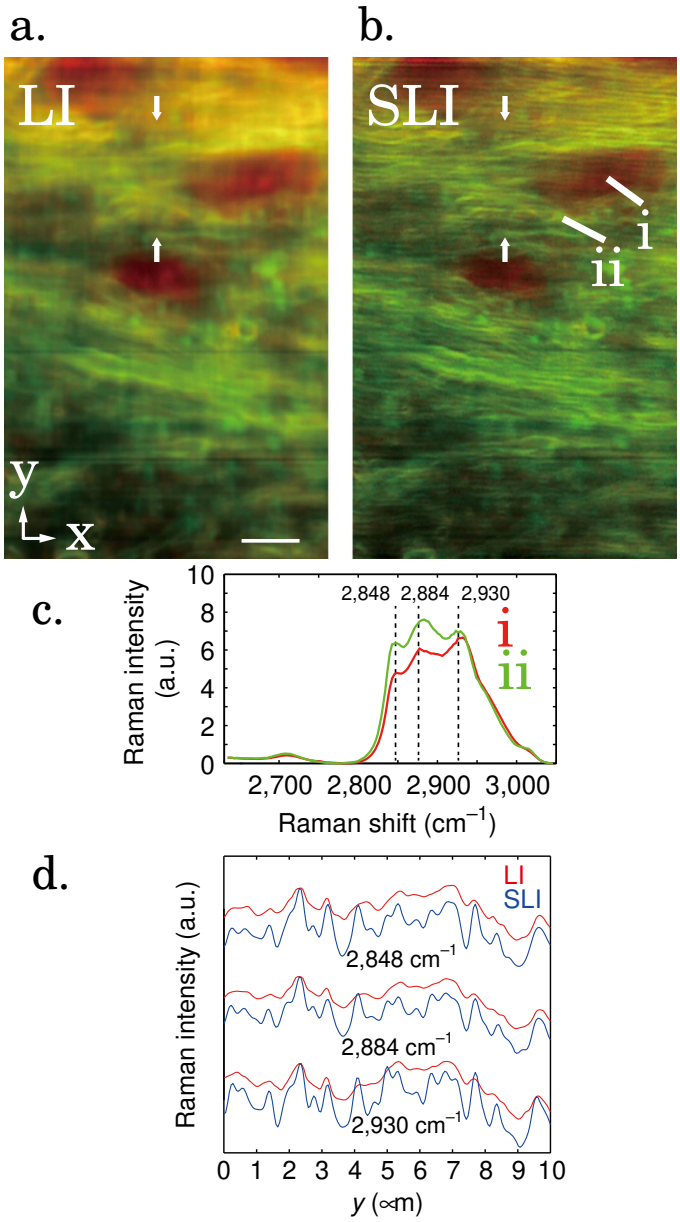

Figure 1.18: **Spontaneous Raman images of a mouse brain slice**. a.,b. The intensity distribution of Raman peaks at 1682 cm^{-1} (red) and 2848 cm^{-1} (green) imaged by the LI (a) and SLI (b) microscopes (Scale bar, 5 mm). Raman peaks at 1682 cm^{-1} and 2848 cm^{-1} can be assigned to amide-I and CH_2 stretching vibrational modes, respectively, predominantly observed in protein beta sheets and lipids. c. Raman spectra measured in b. d. The line profiles of three major Raman peaks given in the CH stretching region. The intensity distributions between the two arrows in a. and b. are shown. Adapted from [73]

1.5 Imaging in biological tissues

To better understand why it is difficult to work with biological tissues, we need to focus on scattering in biological tissues. Indeed, scattering often is the limiting factor to deep imaging with optical systems. Then, we will discuss depth sectioning in biology which enable imaging system to take into account only for the photons generated at the focal spot. Finally, we will explore what has already been achieved in super resolution at depth.

1.5.1 Effects scattering in biological tissues

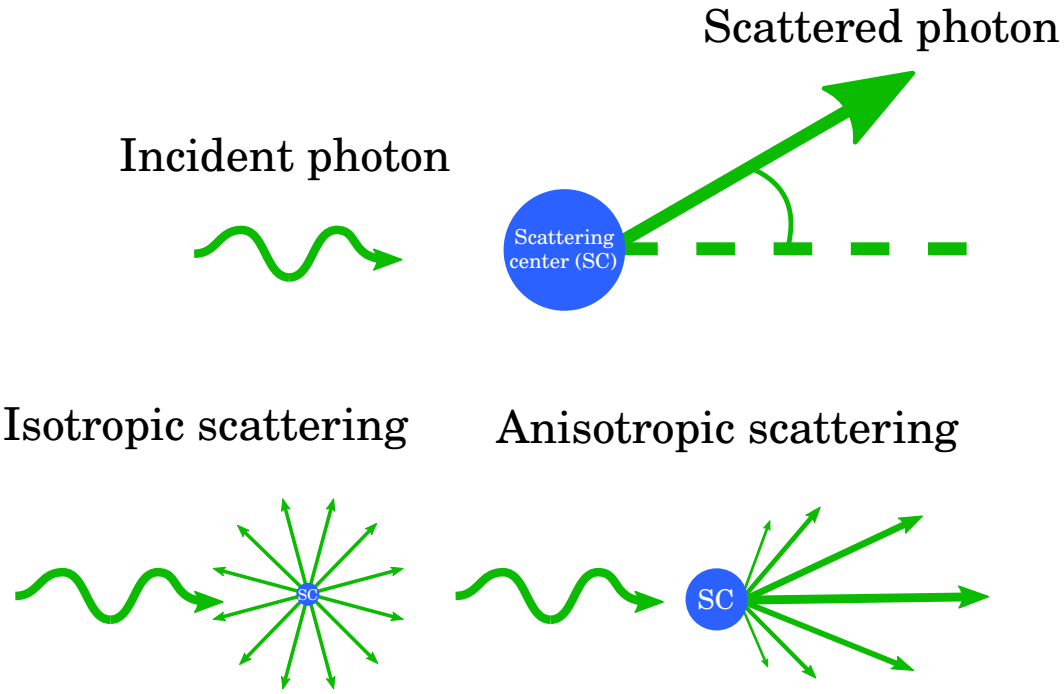

Figure 1.19: **Isotropic and anisotropic scattering**.

First, the absorption of light in biological tissues is negligible compared to scattering and more so with the wavelength that are used in this manuscript i.e. near-infrared light — 800 nm and $\sim$ 1050 nm. Indeed, we work in the *optical therapeutic window* which spans from 600 nm below which hemoglobin strongly absorbs to 1300 nm above which water strongly absorbs as can be seen in Fig.1.20.

However, light propagation in biological tissues suffers from scattering which is the result of photon direction changes caused by inhomogeneities of the refractive index. Photons can be elastically or inelastically scattered, the former is the scattering we will study here and the latter is responsible for Raman scattering signals and we studied it in a previous section 1.2.2..

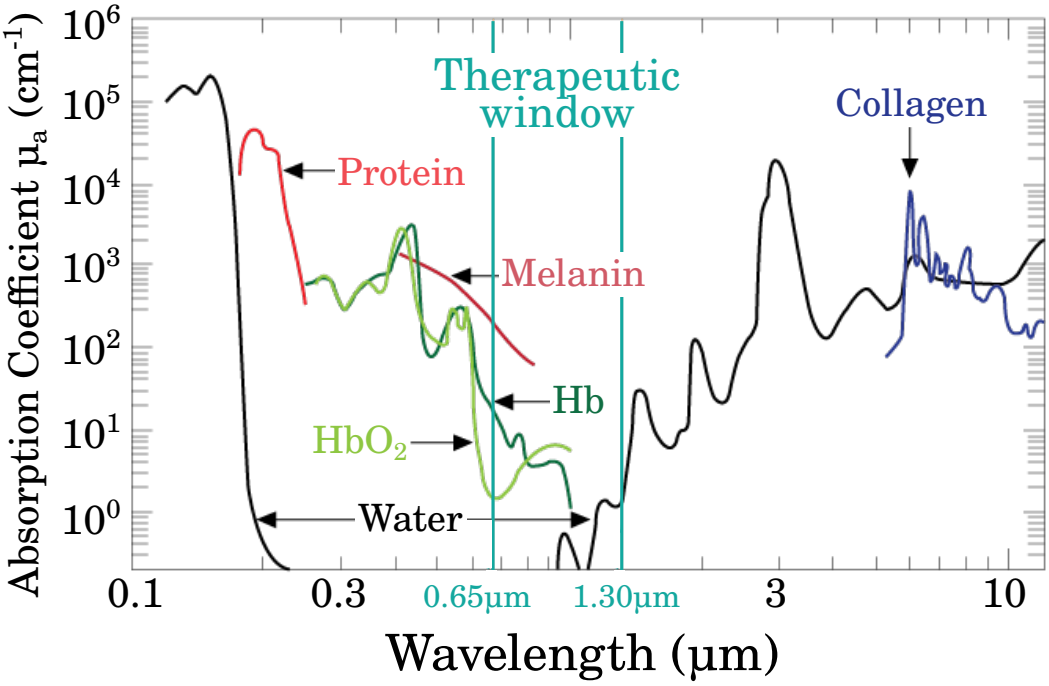

Figure 1.20: **Absorption coefficient of different component of biological tissues**. Adapted from [82]

First, let us characterize the strength of the scattering i.e. the average distance between two events of scattering which is called the "scattering mean free path" l_s. When compared to the optical thickness of the medium L, the characteristic length l_s defines three scattering regimes:

- $L \ll l_s$ is the ballistic regime where most of the photons are unaffected,
- $L \approx l_s$ is the single scattering regime where most photons are scattered once,
- $L \gg l_s$ is the multiple scattering regime where most photons are multiply scattered.

The higher the density of inhomogeneity and/or the higher their index mismatch with inhomogeneities the higher the scattering strength and thus the lower the distance l_s. Regarding the direction of the scattering and its distribution, it depends on the ratio of the characteristic size of the inhomogeneities and the wavelength of illumination. After one or several scattering events, the photon can "loose" its origin direction memory, this distance is called "transport mean free path" l_t and it depends only on the scattering mean free path and how much a single scattering event can make the photon loose memory of the direction it is coming from. It is called the isotropic parameter g.

Thus, the transport mean free path can be derived as $l_t = \frac{l_s}{1-g}$ where $g = \langle cos(\theta) \rangle$ is the anisotropy parameter which measures the amount of light going forward or backward.

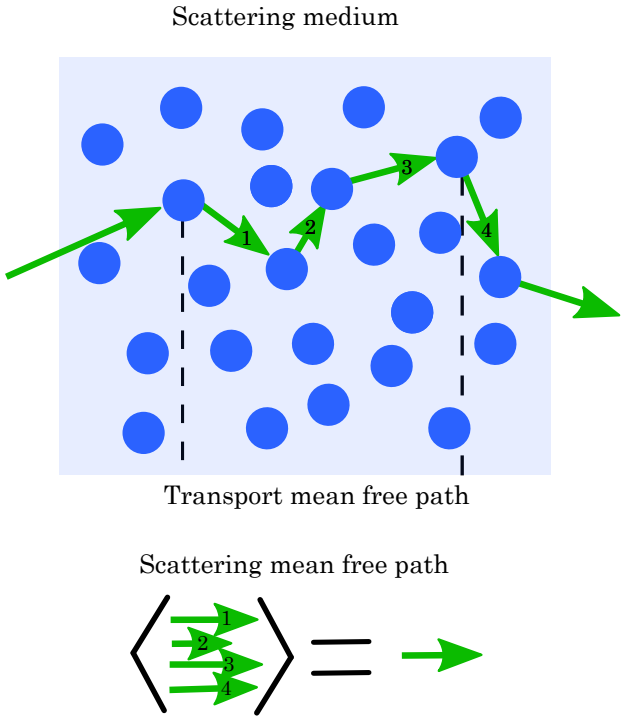

Figure 1.21: **Scattering medium effect on light**.

- If g is small $g \ll 0$, $l_t \approx l_s$ so it means that any scattering event make the photon loose its origin direction memory and it correspond to the isotropic scattering case.
- if $g \approx 1$ i.e. $\lim_{g \to 1} l_t = +\infty$, the photon keeps its origin direction memory over a long distance which means the photon is always forward scattered which correspond to the limit case of anistropic scattering.

If an object is small before the wavelength the scattering direction distribution will converge toward isotropic scattering while it will be mostly forward scattering when the object is large before the wavelength as illustrated in Fig.1.19. In general, biological samples in the *optical therapeutic window* have the following optical properties [83]:

n	Refractive index	1.33 - 1.5
l_a	Absorption length	$1 - 10$ mm
l_s	Scattering mean free path	$5 \cdot 10^{-2}$ mm - $2 \cdot 10^{-1}$ mm
l_t	Transport mean free path	1 mm
g	Anisotropy factor	$0.8 - 0.99$

Table 1.2: **Optical properties of biological tissues**.

For example, in brain tissues $g \approx 0.9$ [84] so the scattering direction is mostly in the forward direction and it is the case for most of the biological tissues for visible and infrared wavelengths.

In any case where $g < 1$, scattering leads to an increase in PSF aberration [85] and a drop in ballistic light reaching the focus due to an increased likelihood of photons being scattered. Thus, as one would want to image deeper and/or do super resolution, it will be more and more difficult to rely on power (STED-like approach) or known patterns (regular SIM). Indeed, the ballistic power exponentially decays with the imaging depth following a Beer-Lambert law:

$$P_{focus} = P_0 e^{-\frac{z}{l_s}} \tag{1.30}$$

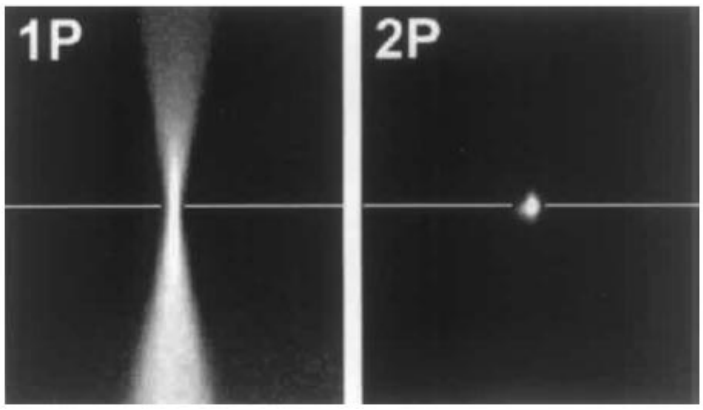

Figure 1.22: **Sectioning capabilites illustrated with 1PF and 2PF in a fluorescine-filled tube**. Figure extracted from [86].

where P_0 is the power just before entering the scattering medium. It is interesting to note that l_s is the parameter that controls the power decay and not l_t since even a very small deflection from the original direction would make the photon miss the focal volume.

1.5.2 Sectioning in biological tissues

In biology, the possibility to image 3D objects is one of the most sought feature for biological imaging of tissues. When one images complex 3D samples, if the imaging technique does not inherently separate plans in the longitudinal direction the result will be an average image of the whole 3D volume projected on a 2D plan. To distinguish between each longitudinal plane, the optical technique requires to exhibit so called sectioning behavior which can be achieved by many different means including nonlinear signals like 2PF, 3PF, SRS or CARS. This is why in 1.3.a. where they image 1.5 mm deep inside mouse brain the authors used 3PF and more generally this is the most important benefit for higher nonlinear order processes in imaging. Thus, the signal

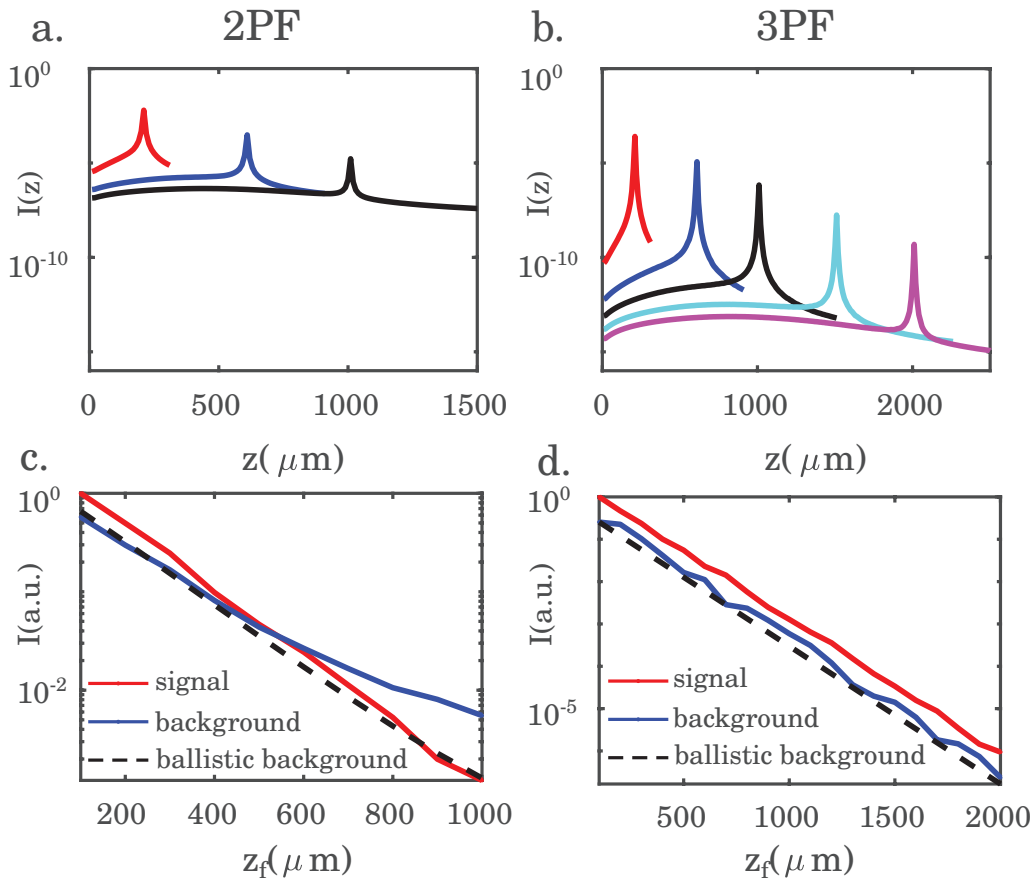

Figure 1.23: **Relationship between nonlinear order and background rejection**. Simulations of two-photon and three-photon signal in a multiple scattering medium with excitation wavelength centered at 1200 nm ($l_s = 264\mu m$) and 1700 nm ($l_s = 400\mu m$) respectively with an objective of NA = 0.6 and $g = 0.9$. **a**. 2PF $I(z)$ for three different focus positions. **b**. 3PF $I(z)$ for five different focus positions. **c-d**. Signal (red), background (blue) and background coming only from ballistic light (dashed black). Figure adapted from [87].

is preferentially generated in high intensity zone i.e. close to the focus as highlighted in Fig.1.22 (right) because of the nonlinearity of the 2PF signal. Whereas in 1PF, the signal is generated linearly with the exciting intensity thus any intensity in the focusing beam is contributing equally whether the intensity is high or low as it can be noted in Fig.1.22 left — $I_{1ph} \propto I_{exc}$ while $I_{2PF} \propto I_{exc}^2$. Consequently, in 2PF it is possible to optically "section" the sample to reconstruct 3D structures of the object. But in the multiple scattering regime, this sectioning ability is different depending on the nonlinear order [87]. Indeed as shown in Fig.1.23.a.-c., 2PF signal is generally limited in depth by the signal coming from layers between the entrance and the focal volume of the scattering medium. The 2PF signal is thus limited by the signal to noise

ratio as one would want to go deeper. On the contrary, in 3PF the signal outside of the focal volume is very much attenuated thus most of the signal is coming from the focal volume itself. As shown in 1.23.d., the imaging depth is not limited by the signal from outside the focal volume but by the PSF degradation. Thus to greatly improve the depth of imaging it is favorable to go for higher nonlinear order and super resolution technique resilient to PSF degradation.

1.5.3 Light propagation in scattering media

We describe briefly here the propagation of monochromatic and spatially coherent light through a scattering medium for a single polarization [88]. When light propagates in a scattering medium like a biological tissue, the phase of the incoming wavefront is scrambled resulting in a statistically uniform distribution of the phase between [0 2π]. As a result, light describes a complex but deterministic interference pattern which is called speckle (Depicted in Fig.1.24). In fact, although it is a random phase interference, it has well defined properties:

- The probability density function (PDF) of the speckle follows a Rayleigh law such that $P(\frac{I}{\langle I \rangle}) = e^{-C \cdot I/\langle I \rangle}$ (see Fig.1.24, right).
- Fluctuation of the speckle intensity is equal to the average intensity resulting in a contrast $C = 1$.
- The speckle grain size is limited by diffraction.

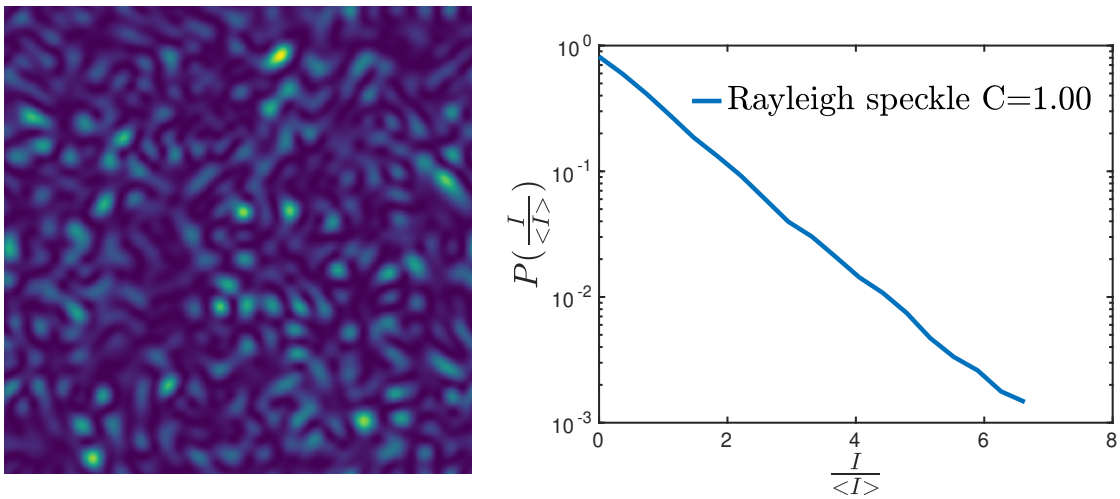

Figure 1.24: **Speckle pattern and its statistics**.

Finally, speckle pattern naturally arise from random scattering and it thus very robust in scattering medium. Indeed, any additional scattering medium will add random phases contributions which will always result in a speckle pattern.

Chapter 2

A multi-modal nonlinear microscope

In the previous chapter, we stressed the need for new label-free super resolution imaging techniques that are compatible with biological samples. Here, we will first describe the setup that I have built during my PhD and what it was used for. Then, we will go further in details in blind-SIM specific feature in the setup and a brief description about the different sample preparations. Finally, we will see that the multi-modal microscope scheme can be used for speckle tailoring experiments in combination with blind-SIM techniques. Later, chapter 5 will give an introduction of the other possibilities to use the setup for. Indeed, it was designed to be used in many other contrast mechanisms than SRS like CARS, 2PF and 3PF, SHG or even THG and each of these signals in single or two-color excitation scheme in combination with blind-SIM and speckle tailoring.

Note: For experimental images we will be using a "inferno" colorbar and a "viridis" colorbar for simulation images. Both colorbars are perceptually sequential uniform. Indeed, researchers have found that the human brain perceives changes in the lightness parameter to scale linearly with linear changes in the data whereas changes in the hue are not perceived linearly. Therefore, colormaps which have monotonically increasing lightness through the colormap will be better interpreted by the viewer [89].

2.1 General overview of the setup

In this section, we will describe the main parts of the setup. A detailed layout of the setup is depicted in Fig 2.1. In the idea of designing a proof of concept experiment for super resolution imaging in biological tissues, we envisioned a multi modal nonlinear microscope that is versatile. To this end, there is a need for short pulsed lasers for any multi-photon processes and an adjustable wavelength to target different Raman resonances in a stimulated manner. The combination of a femto-second laser with an optical parametric oscillator (OPO) fits the above mentioned requirements. Then, we can control the spectral shape of the pulse using a combination of grating, digital micro-mirror device (DMD) and a mechanical slit, thus, we can do chemically selective images. And finally, the introduction of a spatial light modulator in the setup enables us to make use of wavefront shaping and speckle distribution tailoring techniques. The setup is designed such that it is easy to swap between modalities or to combine different modalities and foster their complementarity. There are two configurations that were mainly used during the PhD, we will refer to them as the conventional and the blind-S^3 technique. Those two configurations will be explained later in the dedicated chapter.

2.1.1 Illumination part

Laser and OPO

The basic block of the setup is a femto-second laser (P, Coherent, Chameleon Ultra

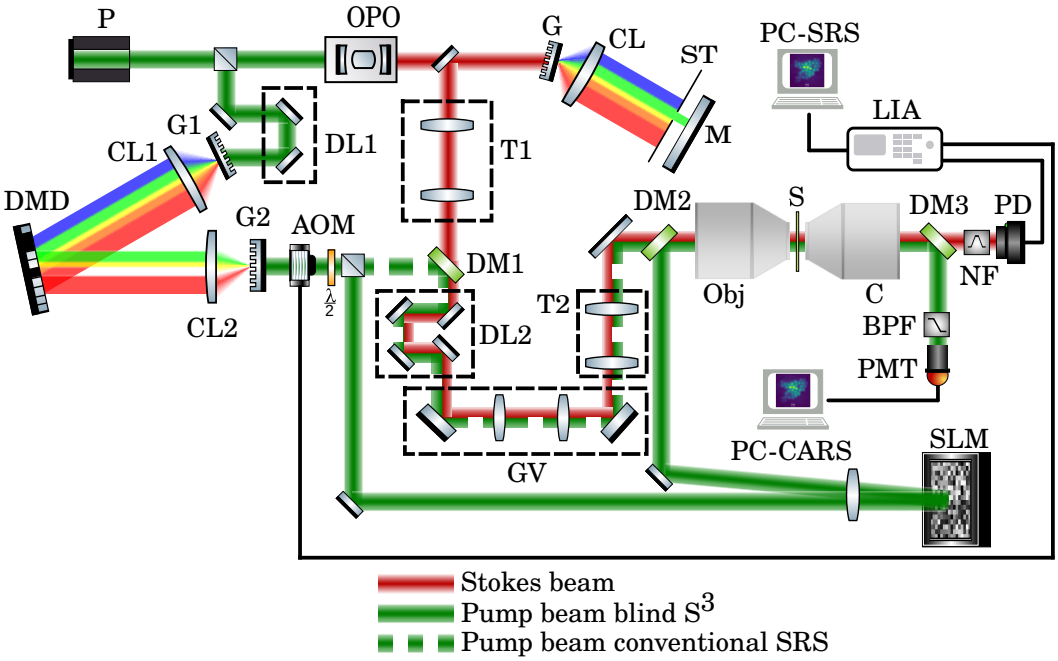

Figure 2.1: **Detailed scheme of the setup used to perform experiments.** Legend: P=Pump laser, OPO=optical parametric oscillator, DL=delay line, T=telescope, DMD=digital micro-mirror device, AOM=acousto-optic modulator, G=grating, CL=cylindrical lens, M=mirror, DM=dichroic mirror, SLM=spatial light modulator, Obj=microscope objective, C=condenser, LPF=long-pass interference filter, NF=notch interference filter, PD=photodiode, LIA=lock-in amplifier, PC-SRS=computer SRS signal, BPF=Band pass filter, PMT=Photomultiplier tube, PC-CARS= computer CARS signal.

Vision) centered in wavelength at 800 nm with a repetition rate of 80 MHz and a pulse duration length of 150 fs.

We will refer to this laser beam as the "Pump" or "Pump beam" hereafter. A fraction of the Pump beam power feeds an OPO (APE, MIRA-OPO) that generates a second laser beam in the near infrared — from 900 nm to 1300 nm— that we will call the "Stokes" or "Stokes beam" from now on. Depending on the molecule under study, the Stokes beam will be set such that the difference in energy with the Pump beam matches the Raman resonance of that molecule (see section 2.3 for more details). A feedback loop ensures the stability of the OPO wavelength for the duration of the experiment.

2.1.2 Spatial and temporal overlap

Delay lines, telescopes and dichroic mirrors

In multi photon processes, the signal generated scales non-linearly with the intensity of the excitation beams. Therefore, it is essential to have the different pulses well overlapped in time and spatial domain. To achieve the temporal overlap, we make use of two delay lines, one for the conventional scheme of Raman process (DL1) and another one for the blind-S^3 scheme (DL2). Then, to merge the two beam paths, we use two dichroic mirrors similarly to the delay lines, one for the conventional technique (DM1) and one for the technique we developed (DM2).

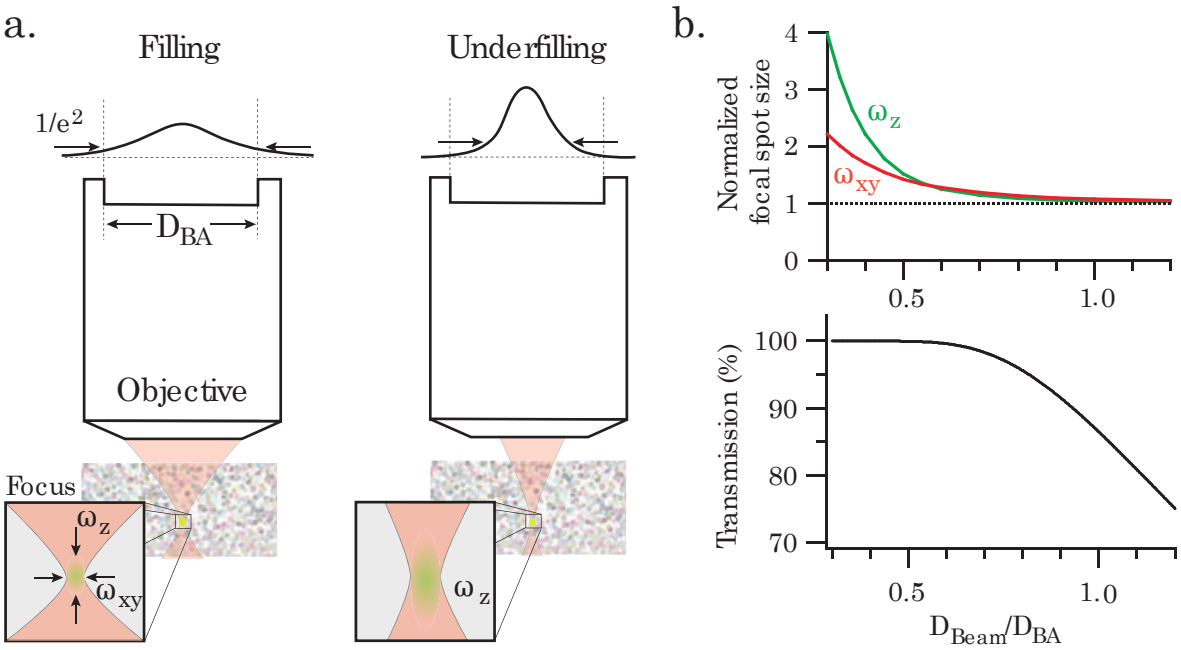

Figure 2.2: **Beam size dependency to the filling factor of the back aperture of the objective [90].** (**a**) Scheme on the relationship between beam size and filling factor. (**b**) Focal spot size and power transmission as a function of the fill factor, the ratio between D_{Beam} ($1/e^2$ - width) and D_{BA} . Radial width (ω_{xy}) and axial width (ω_z) of the focal volume are normalized to the values for a uniformly filled back aperture. For fill factors around 0.7, nearly all power is transmitted with only minor losses in lateral and axial resolution.

Finally, we use several independent telescopes for the different beams to match their waist diameters (T1) and to fulfill the back aperture of the microscope (T2). By doing that, the back aperture of the objective is overfilled and thus the focal spot reaches the optimum intensity with high resolution. Indeed, the filling factor of the back aperture of the objective — ratio between diameter of the beam and diameter of the back aperture — ensures minimal spot size while giving up some energy (see Fig.2.2 adapted from [90]).

2.1.3 Spectral shaping

Pairs of gratings in combination with a DMD or a slit

To target specific Raman spectrum resonances (see section 1.2.3), one needs to reduce the number of vibrational resonances that can be excited. We achieve this task by reducing the spectral content of the pulses, meaning filtering out portions of the spectrum. In the setup, we use two different techniques to achieve this goal.

For the Stokes beam, we use a grating (G, LightSmyth, T-1000-1040), a cylindrical lens (CL) and a silver mirror (M) to back propagate the beam through the cylindrical lens, grating and recombine the different wavelength into a collimated beam. Just before the silver mirror, — i.e. right before the back reflection — we positioned a mechanically adjustable slit onto a 1D stage to select the width and region of the Stokes spectrum.

For the Pump beam, unlike the Stokes beam, we wanted to change quickly the selected region of the spectrum. Accordingly, instead of using a mechanical slit we used a digital micro-mirror device (DMD). A DMD is a matrix of independently controlled micro-mirrors that can rotate $\pm 12°$ around their diagonal axis (see bottom images in Fig 2.3.a.). Each micro-mirror is mounted on an independent complementary metal-oxide-semiconductor static random-access memory (CMOS SRAM) cell and electro-statically triggered depending on whether a "1" or a "0" is written into the cell. For the mirrors to move, a gap between the mirrors of the matrix is left opened. These gaps give rise to a 2D grid structure that acts as a blazed grating for light. In other words, it means that the specular reflection and diffraction orders are not overlapped in space without taking care of this diffraction effect. Since we work with multi photons processes, we cannot afford to loose energy and we optimized the orientation of the DMD to overlap the 0^{th} order of the blazed grating with the specular reflection on the mirrors to maximize the output energy from that pulse shaper [91]. To better understand how to align the DMD, we ran a 1D simulation using blazed grating equation :

$$\sin(\theta_i) + \sin(\theta_m) = \frac{m\lambda}{d} \tag{2.1}$$

where θ_i and θ_m denotes incident and m^{th} diffraction angle respectively, m the order, λ the wavelength and d the DMD pixel size (10.8μm in our case).

To overlap the specular reflection and the 0^{th} diffraction order, one needs to meet two conditions: m is an integer (equation 2.1) and angles follow $\theta_m = 2\theta_i - \alpha$. To sum up these conditions, we derived the following equation :

$$\mu = \left| \frac{2d}{\lambda}(\sin(\theta_i) + \sin(2\theta_i - \alpha))\ [1] - 0.5 \right| \tag{2.2}$$

where $|\cdot|$ is absolute value and $[\cdot]$ stands for modulo 1.

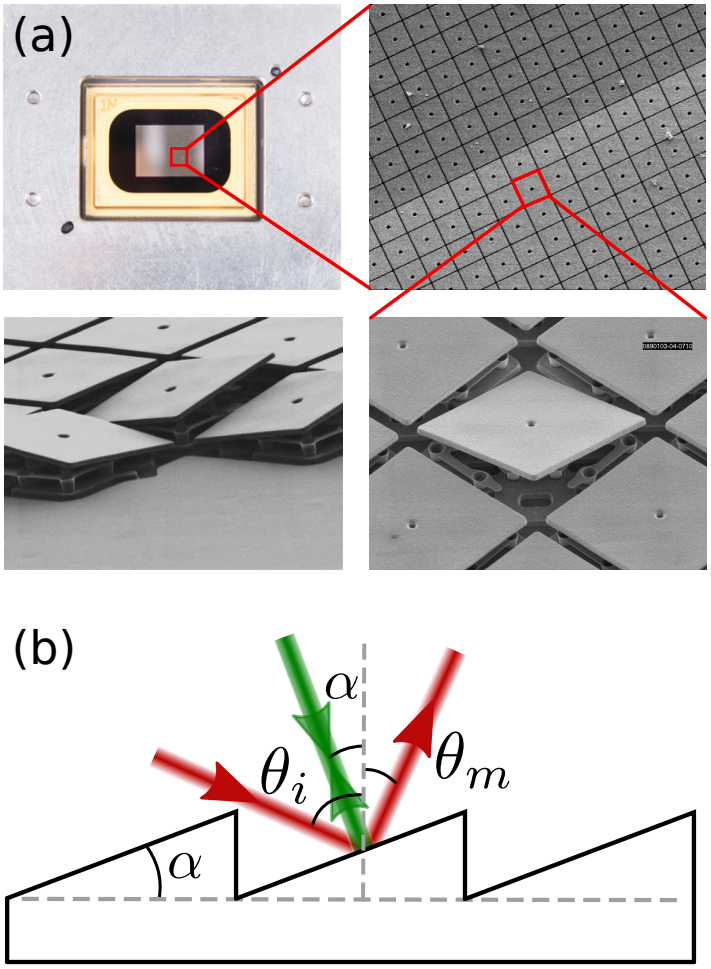

Figure 2.3: **Digital Micromirror Device and blazed grating scheme.** (**a**) View of the DMD under different scales. (**b**) Scheme of the blazed grating structure of the DMD. Green is the Littrow configuration, Red is the general case.

To find the optimal incident angle, we need to find the points that are around 0.5 and the closest from the center (see Fig 2.4.a.). The red line represents the Littrow configuration, meaning the incident angle is equal to the blazed angle α thus the specular reflection happens in the same direction as the incident angle. This direction is quite off from a diffraction angle so the output power would be low. It is the same case if the incident angle was set perpendicular to the DMD plane, which is represented by the orange line. Those two configurations are experimentally convenient but not optimal. The optimal cases are located at $-11.3°$ and $34.5°$ represented by the green line.

Finally, we used a pair of gratings (G1 and G2, LightSmyth Technologies, T-1400-800) and cylindrical lenses (CL1 and CL2) to access the spectral component of the

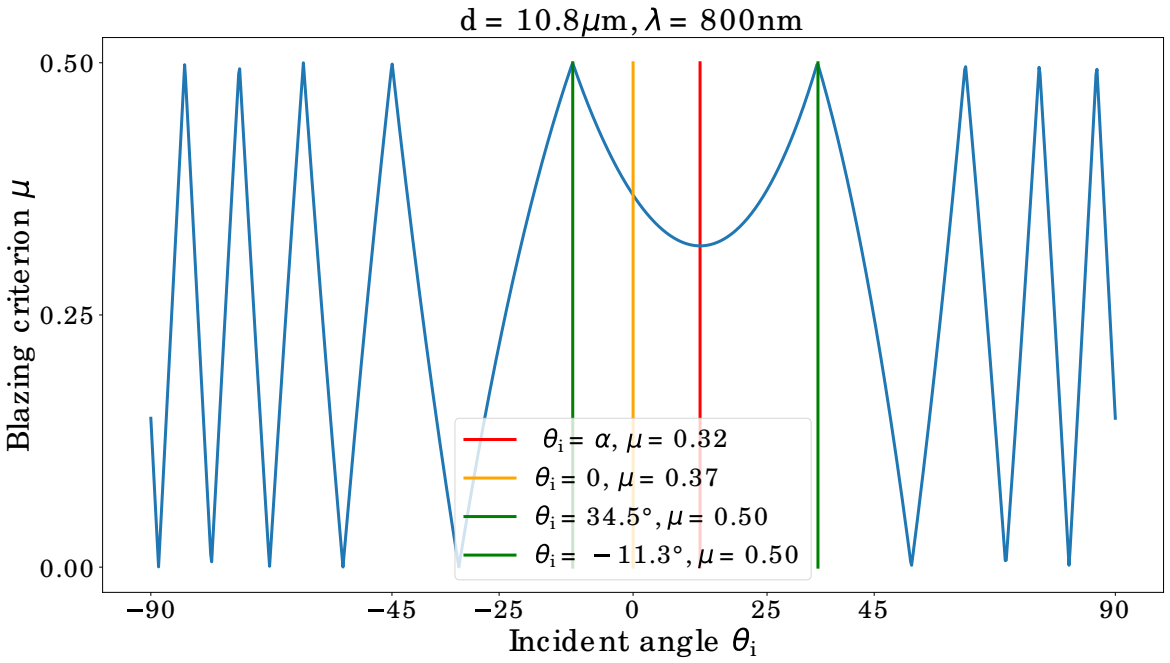

Figure 2.4: **Simulation of blazed grating conditions.** (**a**) Simulation of the blazed grating conditions to overlap the specular and diffraction orders. Red bar is Littrow configuration. Orange is illumination perpendicular to the plane of the DMD. Green are the two optimal angles for to obtain a great energy output.

beam on the DMD and recombine the selected wavelengths in a collimated beam after the second grating. Note, we used a telescope with two cylindrical lenses to correct for the slight asymetry that we had at the output of the pulse shaper.

2.1.4 Wavefront shaping and speckle tailoring

SLM and 4f system

To have the ability to implement wavefront shaping and to have a programmable FOV for the blind-S^3 on the multi-modal setup, we introduced a spatial light modulator (SLM) and used a 4f system to image the SLM in the back-focal plane of the objective. The SLM is then used to generate speckle pattern in the sample plane (S) as we apply random phase pattern onto the SLM. Note that we are not using a scattering medium here because we need high output power and also the ability to control the speckle envelope of the speckle pattern — the spread of the power. Plus, we need an easy and fast way to change the speckle realization. We were careful to remove as much as possible non modulated light from the SLM to avoid specular reflection off the SLM window that could have induced. In the last chapter, we use the SLM to engineer the wavefront of the beam to generate arbitrary speckle intensity distribution.

Note that there is not the same issue to overlap the specular reflection and diffraction orders as in section 2.1.3 since the plane of the SLM always stays flat and thus does not introduce an angle between the specular reflection and the 0^{th} order.

2.1.5 Scanning the sample plane

Galvanometric mirrors and microscopy objectives
During my PhD, we mainly work on multi photons processes hence we used high NA water immersion objectives (Obj, Nikon, Plan APO IR, 60x, NA=1.27 and Zeiss, Plan APO IR, 40x, NA=1). Since the quality of the focus is of tremendous importance, the objective was corrected for chromatic aberration — i.e. apochomatic objective. As we have experimentally noticed, without this correction it would not be possible to overlap the two beams used for SRS in the near infrared (NIR). In the experiments, we use point scanning technique to build up an image as it is usually the case for nonlinear imaging. To raster scan the beam, we use a set of galvonometric mirror (GV) mounted in a 4f system to ensure the beam stays as stable as possible in the back-focal plane of the objective thus limiting non homogeneous deposition of energy in the sample plane — i.e. vignetting effect. Typical average power measured before the objectives were 13 mW (conventional) and 41 mW (blind-S^3) for the Pump, and 25 mW for the Stokes beam in both cases. Note that the power for the Pump beam is spread over a wider region as it is a speckle pattern whose diameter is controlled by the size of the SLM pixels grouped together consequently the power density on the sample is lower for blind-S^3 scheme.

2.1.6 Remarks for two-tight-focus-overlap experiments

As many nonlinear imaging system, it is of particular importance to be very careful at the spatio-temporal overlap of the two beams. Indeed, the precision of the alignment has to be correct at sub-wavelength length-scale at the focus in order to reach high intensity. Hence, it is necessary to check and optimize again the alignment each and every time an experiment is run. Indeed, slight changes in the air temperature or humidity can induce optical path difference and more importantly it can induce expansion or contraction of the optical element that will result in a misalignment. It can result in a significant drop in the already low signal in this very sensitive experiment, especially in the femto-second regime since temporally speaking it requires more precision.

2.2 Blind structured illumination scheme

In the previous section, we presented what is common between each scheme we used. In this section, we will explore more in detail each specific feature of the setup starting with the different temporal regime we operated in and then SRS and coherent anti-Stokes Raman scattering (CARS) specific characteristics.

2.2.1 Spectroscopy implementation

Chemical selectivity is one key feature from SRS and CARS that is highly desirable for microscopy imaging (see section 1.1.2 for more details). The pico-second pulse regime is well known to be the best candidate for highly chemically selective coherent Raman imaging [92]. Since we work with femto-second laser, the implementation of two pulse shapers enables us to easily switch between pic-second and femto-second regime by closing the mechanical slit or changing the pattern on the DMD.

2.2.2 Stimulated Raman Scattering

Experimentally, the main difference between SRS and CARS lies in the detection scheme of the signal. First, to detect the small ΔI_{SRG} (see equation (1.15)), it is required to use a modulation/demodulation scheme. Thus in the setup, an acousto-optic modulator (AOM, MT80-B30A1,5 VIS, AA Opto-electronic) was operated at 1MHz frequency in the part of the Pump which is shared between conventional and blind-S^3 scheme. Consequently, the Pump beam — 0^{th} order — is intensity modulated and demodulated by a lock-in amplifier (LIA, Zurich Instruments, MFLI). Secondly, since both the Pump and Stokes beams are collected by a 1.4 NA oil-immersion condenser, the Stokes is directed to the SRS detection scheme while the Pump beam is directed to the CARS detection scheme for alignment purposes (see section 2.2.3) using a dichroic mirror (980nm longpass, Semrock). Then, we filter out (NF, two NF808-34 and two FELH0950, Thorlabs) the Pump beam in order to detect the SRG signal. Indeed, since we modulate in intensity the Pump beam, it is not possible to see the SRL in the Pump beam. Third, to detect SRS signal one needs a large-area photodiode (PD, Thorlabs, DET100A2) for two reasons [93]. Indeed, to detect the small ΔI_{SRG} a high dynamic range (ratio 10^4) is required. In addition, it prevents parasitic signals like cross phase modulation (XPM). Indeed, the two copropagating beams are tightly focus and may induce a change in the refractive index seen by the other beam. It results in a shift of the focus in the longitudinal direction and a defocus beam on the photodiode. If the area of the photodiode is too small, such defocus induces a false signal which is not from the sample nor chemically selective.

2.2.3 Coherent Anti-Stokes Raman Scattering

The CARS signal can be collected simultaneously with the SRS signal. The setup was designed to do so but it was not used in this PhD. After the condenser collected both beams, the Pump beam is separated from the Stokes beam with a dichroic mirror (DM3). The Pump beam is steered at the photo multiplier tube (PMT) only used for alignment purposes. It is then filtered out (BPF, FBH650-40, Thorlabs) just before the PMT to let only the CARS signal go through.

2.3 Sample preparation

During the PhD, we mainly worked with three different samples that are described in the following sections. Each of them has its own utility in the assessment process of the newly developed imaging technique.

2.3.1 Polystyrene beads

First, we use a set of polystyrene beads of several diameters in order to start with large diameter beads and to go down in size to challenge the capabilities of the technique. Namely, we used 1μm, 0.5μm and 0.239μm beads. Since the nominal diameter of these beads is well calibrated, it enabled us to make sure the technique worked properly. For bead diameters larger than the diffraction limit, we also use the conventional SRS (resp CARS) signal to control the quality of the reconstructed images. Regarding the sample preparation, we use a "drop casting" methodology meaning we drop a liquid containing the polystyrene beads in suspension onto a cover-slip. Then, we let the liquid dry, glue a double face tape spacer of 120μm-thick and fill in with so called 'heavy-water' — deuterium oxide, ^2H_2O (D_2O). This solvent was of great importance during the super resolution experiment. Indeed, using heavy-water shifts the wide Raman resonance from water molecules, since the water molecule is heavier the vibrational states change (see Fig. 2.5.**c**). Thus, less signal generated by water molecules was coming from the spacing between the polystyrene beads and enabled us to perform super resolution. In Fig.2.5, we send a speckle pattern and scan the Stokes beam inside a thick deionized water sample and a heavy water sample. We can see in **a**. that the deionized water is emitting signal. Using exactly the same settings, we can see that using heavy water enables us to reduce substantially the signal coming from water molecules. Note that this signal is weak as we were using twice the power and 10 times higher integration time than for any blind-SIM acquisitions showed later.

Finally, we sealed the sample with another cover-slip coming on top the spacer.

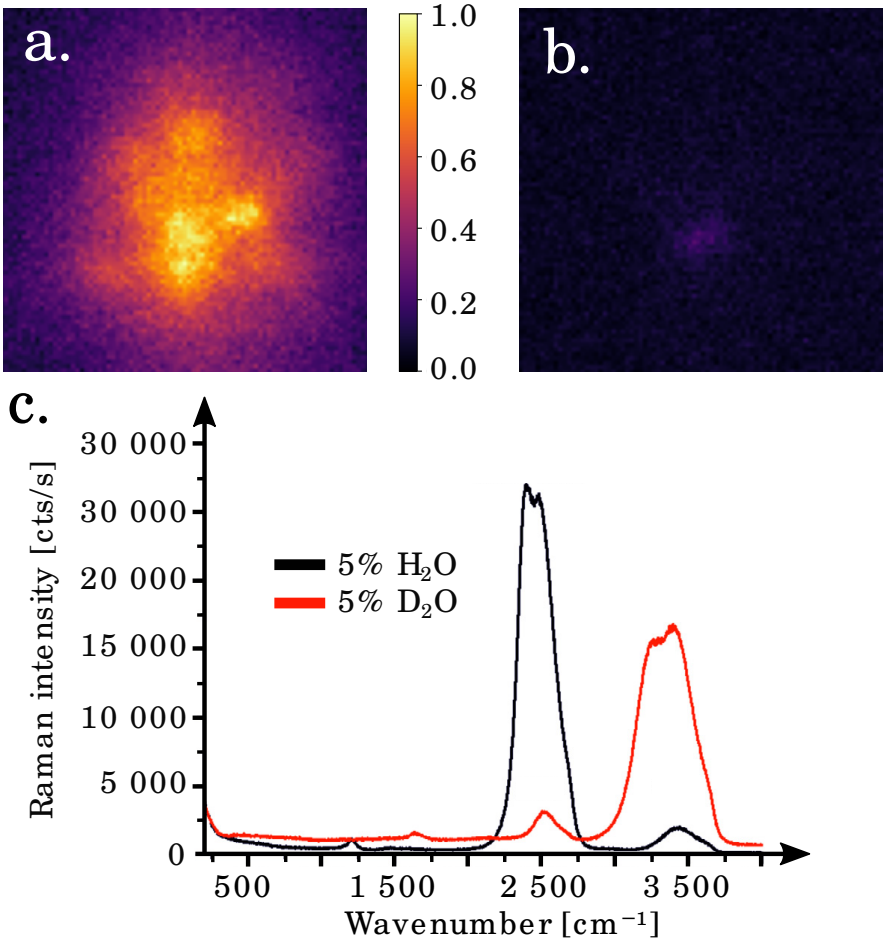

Figure 2.5: **Comparison between water and heavy water SRS signal. a**. Deionized water signal normalized from a speckle pattern. **b**. Heavy water signal from a speckle pattern. Normalized by the maximum of deionized water signal. **c**. Spontaneous Raman spectra of 5% H_2O diluted in D_2O (black line) and 5% D_2O diluted in H_2O (red line), adapted from [94]

2.3.2 Biological sample

Two different biological samples were imaged over the course of this PhD thesis: HeLa cells and mouse brain slices.

These biological samples were kindly provided by Abdou Rachid Thiam, Mohyeddine Omrane (HeLa cells) and Laurent Bourdieu (Brain slices).

HeLa cell preparation

HeLa cells are the first in-vitro immortal human cell lines that are broadly used in biological imaging for proof of concept experiments. These were originally taken from the cervical cancer of Henrietta Lacks without her consent in early 1951. This cell

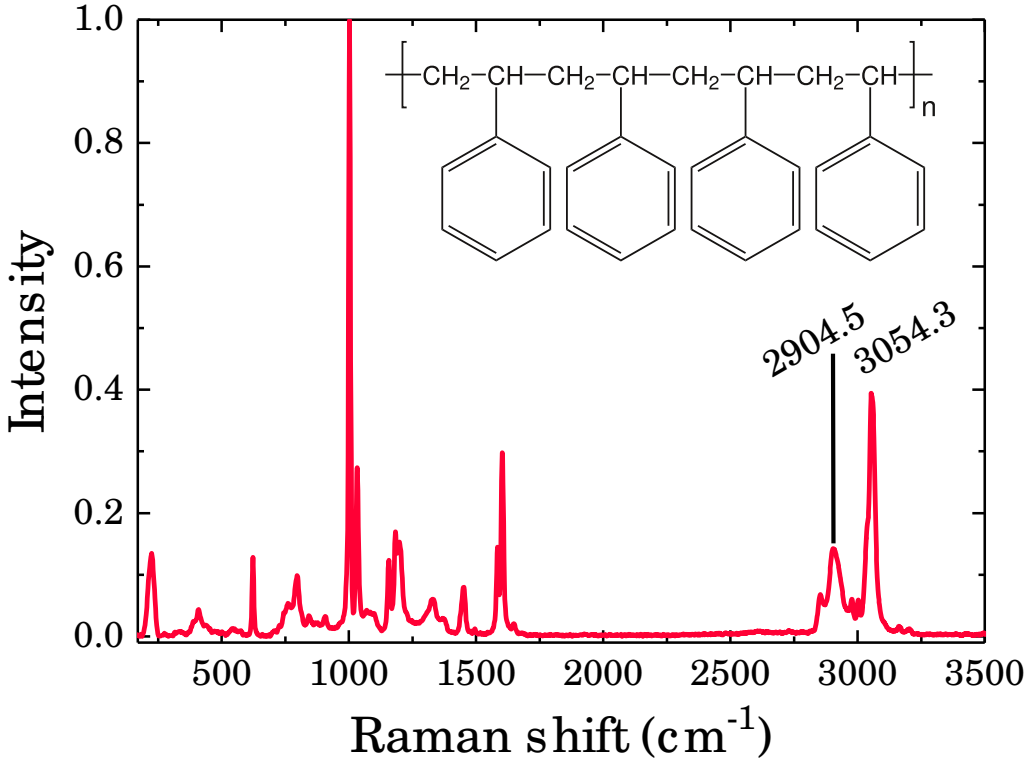

Figure 2.6: **Polystyrene Raman spectrum.**
Normalized intensity Raman spectrum of polystyrene molecules. The experiments described in this manuscript always use one of the two following Raman resonances at 2904.5cm^{-1} and 3054.3cm^{-1}

line led to key discoveries in the field of virology, cancer and played a central role as a testing sample for the polio vaccine that helped to mostly eradicate the disease.

HeLa cells (non profit organization ATCC) were incubated with 400 μM oleic acid, washed, fixed with 4% para-formaldehyde, and stored at 4°C before imaging. During the incubation procedure, cover-slips were put at the bottom of the tank so that HeLa cells fall onto it. We then place a spacer in the center of the coverslip that we fill with Dulbecco's Phosphate-Buffered Saline (DPBS). It is intended to provide a buffer system for maintaining the HeLa in the physiological range of $7.2 - 7.6$ potential of hydrogen (pH). It is used in maintaining mammalian cells when a chemically-defined and balanced salt solution provides the appropriate media to sustain the physiological and structural integrity of cells in vitro for a limited period of time. In the work, we mainly focused on lipid droplets as they have the strongest Raman resonance. Indeed, we are doing a proof of concept so more difficult and weak Raman resonances will be addressed in later work.

Mouse brain preparation

Mice brain slices were kindly provided by Laurent Bourdieu and experimental procedures were conducted in accordance with the institutional guidelines and in compliance with French and European laws and policies. All procedures were approved by the 'Charles Darwin' Ethics Committee (project number 26667). More precisely, 6-months old C57BL6 male mice were sacrificed, the extracted brain was then stored overnight in a solution of 4% para-formaldehyde and finally rinsed in DPBS. Coronal slices of thickness 100μm were then cut and stored in DPBS. Prior to experiments, the slices were placed between two cover slips with a 120-μm-thick spacer. The space between the cover slips was filled in with a mixture of DPBS and 2% of low melting point agarose in order to prevent the structure of the brain to move during the imaging procedure.

Chapter 3

Blind Structured Illumination in Stimulated Raman Scattering

We now have a multi purpose microscope and it will be used to demonstrate super resolution experiment in a label-free manner on a biological sample. For that, we used blind structured illumination and SRS in combination. To begin with, we give a detailed description of the principle of the technique, describe the mathematical framework this experiment fits in and explore the principle of the underlying algorithm used here. Then we ran simulations on Siemens star and virtual beads to make sure it could work in a well controlled environment. And finally, we tested this new methodology on real life samples. First, we show super resolution experiments on calibrated sample such as polystyrene beads where we highlight the remarkable features of the technique. After that, we moved to biological samples such as HeLa cells and mouse brain tissues. In the end, we conclude this chapter by a discussion about what this work has achieved compared to the current state of the art in the literature. This chapter is based on the paper Guilbert et al. [95] currently under review.

3.1 Background on the methodology

In this section, we will introduce the main concepts that are needed for this experiment. It ranges from what happens physically in the microscope to the mathematical formulation of the image formation mechanism and to the algorithm used here.

3.1.1 Principle

As shown in Fig.3.2., there are two different beam paths in our optical setup. Indeed, we need to compare our methodology — namely blind-S^3, right hand part of Fig.3.2. — with the standard way of imaging with SRS contrast mechanism — namely conventional SRS, bottom left hand corner of Fig.3.2. To highlight the differences between conventional SRS and blind-S^3, we will first describe the former.

For standard SRS technique, a Pump beam and a Stokes beam are overlapped and co-propagating. Both beams enter a scanning element which is here composed of two galvanometric mirrors imaged with a 4f system. This enables us to move the focus in the image plane of the objective without clipping on the back-focal plane of the objective (for more details about the galvanometric mirror, objective see sections 2.1.2). There, the two focused and overlapped beams will probe the sample Raman resonance that is targeted and result in a given level of signal. Then the signal is collected by a single-pixel detector and demodulated by a LIA to observe the ΔI_{SRS} which corresponds to the signal for one pixel of an image (see section 1.2.3). Finally, the two beams are shifted in the image plane of the objective to acquire another pixel and build up a full sized image.

In the case of the blind-S^3, nothing changes for the Stokes beam. However, the Pump beam is not going through a scanning element but is steered at a SLM with a

random phase mask, the SLM is imaged with a 4f system in the back-focal plane of the objective and it is recombined with the Stokes beam after it went through the scanning element. Consequently, to make one image, the Stokes beam is the only one that is moving in the image plane of the objective while the Pump beam is a static speckle pattern shining the sample. The spread of the speckle pattern is controlled by the size of the macro-pixels used to generate the random phase mask on the SLM (see Fig.3.1).

Whenever the Stokes beam is overlapped with a speckle grain from the Pump beam and the sample under study — assuming they match the Raman resonance — a ΔI_{SRS} will be detected. At this point, we collected one image of low resolution (see section 3.1.2). Furthermore, since blind-S^3 needs several realizations (see section 1.3.4), a new random phase pattern is set on the SLM in the Pump beam path resulting in a new speckle pattern in the image plane that will be scanned by the Stokes beam and give a low resolution image and so on and so forth.

We have here presented the conventional way of doing SRS and our new methodology to achieve super resolution. Mainly, we presented what is happening physically on the setup, which beams are moving, and which beams are producing speckle patterns. But, since we are acquiring multiple images and we want to merge all the information from this stack of images, we need to find an algorithm that would fuse the information into a single super resolution image. To that end, we will study the image formation mechanism and the reconstruction algorithm in a more formal manner in the next two subsections.

3.1.2 Mathematical framework and forward model of blind-S^3

We start here with a derivation of the image formation model to understand what kind of algorithm could merge the information from the stack of image into a single one. In SRS, the signal detected is a modulation transfer between the Pump and Stokes beams (ΔI_S) at one pixel location (of the un-processed image) is given by [96]:

$$\Delta I_S \propto \Im\{\chi^{(3)}\} I_P I_S \tag{3.1}$$

where $\Im\{\chi^{(3)}\}$ is the imaginary part of the complex-valued nonlinear susceptibility of the sample (related to the Raman cross-section), I_P and I_S the intensity of the Pump and Stokes beam, respectively.

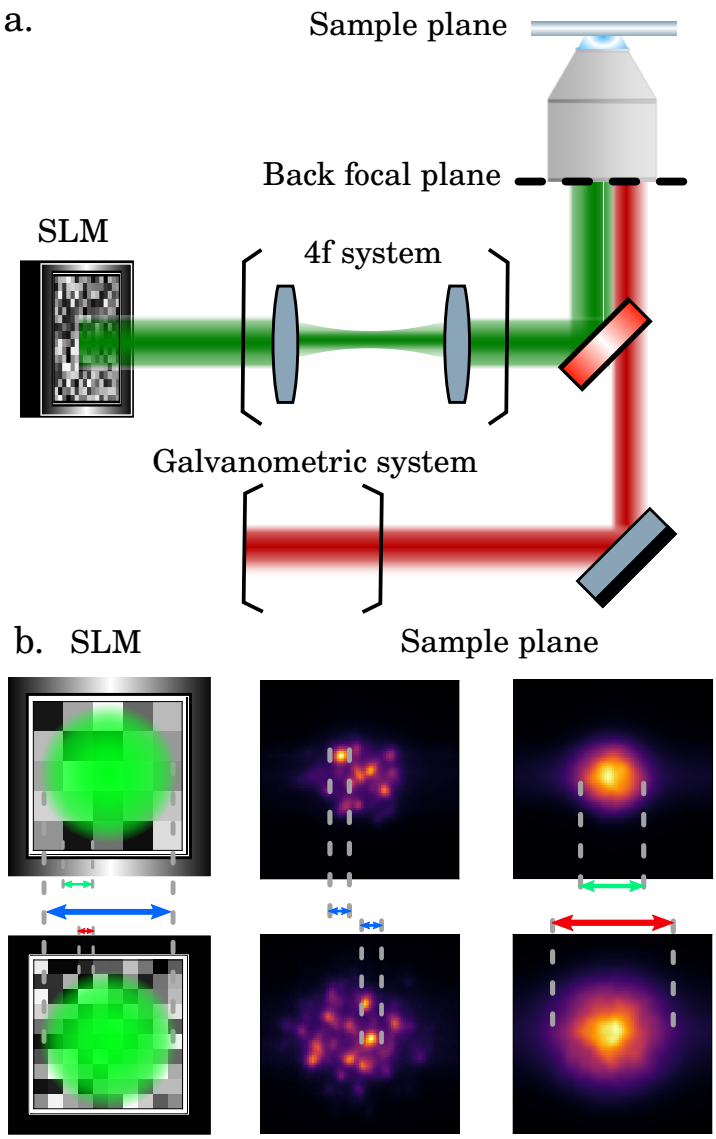

Figure 3.1: **Controlling the spread of the speckle with the SLM**. **a**. Scheme of the setup for blind-S^3. The pump beam shines a random phase SLM pattern and imaged by a 4f system. The Stokes beam is scanned by the galvanometric system and recombined with the Pump beam, thus only the Stokes beam is scanning. **b**. On the left column, a schematic of the SLM shone by a Gaussian laser beam. In the two cases, the beam spreads on the same area of the SLM (Blue arrow) while the size of the macro-pixel is different (Green and Red arrow). The middle column is an experimental 2 photon speckle realization in the thin film of Fluorescein. The spread on the SLM (left column) is inversely proportional to the speckle grain size, noted by the blue arrow. The right column corresponds to the mean over 100 realizations. The average width of the illumination — we can call it field of view (FOV) — is determined by the macro-pixel size of the random phase pattern on the SLM.

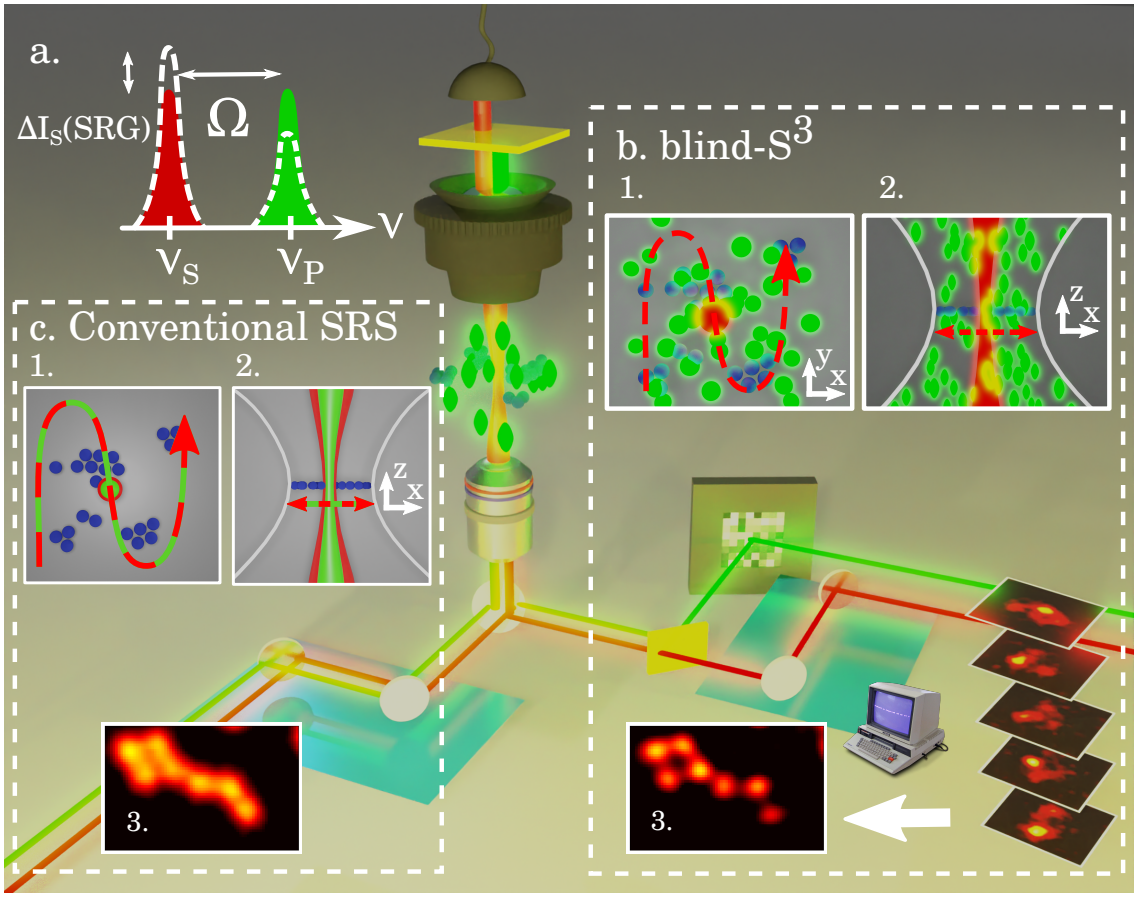

Figure 3.2: **Principle of blind-S^3**. Schematic of the setup to achieve super resolution using the SRS process stimulated Raman Gain (SRG) (**a**) based on a single-pixel SIM scheme. Transverse (**b**1) and longitudinal (**b**2) planes of the scanning Stokes beam trajectory (red dash) over the stationary Raman-active specimen (blue) and structured Pump (green), in this case a speckle pattern. For every speckle realization, an SRS image is acquired forming an image stack that is passed to a SIM algorithm to reconstruct a super-resolved image (**b**3). (**c**) Conventional SRS, consisting in raster scanning co-propagating Pump and Stokes beams, is used as a control to demonstrate the increase in resolution when compared to standard imaging. Transverse (**c**1) and longitudinal (**c**2) planes of the Stokes and focused Pump beams (green and red dash) scanning trajectory over the stationary Raman-active specimen (blue).

In the case of blind-S^3, a static speckle pattern generated by the Pump beam spreads at the sample image plane where the Stokes beam is focused and scanned. To derive an image formation model, we assume a scalar approximation for the local intensity in one blind-S^3 image:

$$\begin{aligned}\Delta I_S(x,y) &\propto \iint \Im\{\chi^{(3)}(x',y')\} I_P(x',y') I_S(x-x',y-y')\,dx'\,dy' \\ &\propto \left(\Im\{\chi^{(3)}\} I_P\right) \circledast I_S,\end{aligned} \tag{3.2}$$

where $\circledast$ denotes the convolution operator, (x,y) the pixel position in the image ΔI_S. In this approximation, we disregard coherent effects as SRS processes are inherently phase-matched.

This so-called forward model presented in Eq. 3.2 is mathematically identical to commonly used models in blind SIM reconstruction algorithms [57, 97] :

$$M_l = \left(\rho \cdot I_l^{illumination}\right) \circledast h_{detection} \tag{3.3}$$

where M_l is one image, ρ the density of fluorophores for example, $I_l^{illumination}$ a speckle pattern and $h_{detection}$ the PSF of the system detection in our case the Stokes beam.

We can see the correspondences between the different terms such a $\Im\{\chi^{(3)}\}$ and ρ which are representing the object under study.

In conclusion here, we can use well-established blind-SIM algorithms from the literature. Indeed, we have identified a sampling scheme that has the same forward model as typically used in SIM. While this is mathematically equivalent, the new sampling scheme comes with differences from the conventional SIM like the sectioning ability which will be further developed in section 3.2.3.

3.1.3 Blind Structured Illumination Microscopy algorithm

Blind-SIM algorithms solve an ill-posed problem by adding up a condition that is required to be met in order to finally obtain a well-posed problem. Indeed, as we can see in equation 3.3, if we acquire N images then we have N equations with N unknown illuminations and one unknown object which means N+1 unknown for N equation as shown below:

$$\begin{cases} M_1 &= \left(\rho \cdot I_1^{illumination}\right) \circledast h_{detection} \\ M_2 &= \left(\rho \cdot I_2^{illumination}\right) \circledast h_{detection} \\ &\vdots \\ M_N &= \left(\rho \cdot I_N^{illumination}\right) \circledast h_{detection} \end{cases} \tag{3.4}$$

To solve this system of equations, there are several options and we will have to look more specifically at two algorithms [57, 97]. The additional condition consists in having a homogeneous illumination, meaning that the sample is uniformly illuminated on average during the acquisition phase. If not, the uniformity will be mirrored in the reconstruction as additional noise for example. In sections 3.3 and 3.2, we will talk about the Gaussian shaped envelope of the reconstructed image and this is due to the Gaussian envelope of the Pump beam and the homogeneous illumination assumption made at the algorithm level. The assumption takes the following form:

$$\sum_{l}^{N} I_l^{illumination} = I_{mean} \cdot N \tag{3.5}$$

Thus, the Nth equation can be re-written as :

$$\begin{cases} M_1 & = \left(\rho \cdot I_1^{illumination}\right) \circledast h_{detection} \\ M_2 & = \left(\rho \cdot I_2^{illumination}\right) \circledast h_{detection} \\ & \vdots \\ M_N & = \left(\rho \cdot \left[N \cdot I_{mean} - \sum_l^{N-1} I_l^{illumination}\right]\right) \circledast h_{detection} \end{cases} \tag{3.6}$$

Remarkably, I_N is gone and it is possible to jointly estimate all the unknown in an iterative process. The algorithm by Mudry et al. [57] then solves the equation system by a gradient descent algorithm to find the density of fluorophores ρ and the speckle patterns $I_l^{illumination}$. We presented this algorithm since it is an intuitive approach to understand the issue to solve this undetermined system. But we decided to use another algorithm from Yeh et al. [97] based on covariance estimation because there is an explicit constrain on the spatial frequency space to ensure that the reconstructed image does not have non physical spatial frequency content whereas in Mudry et al. it is by stopping the iteration before artifacts appear. Consequently, we will only describe this algorithm in the following of the chapter. The algorithm runs in two phases :

- Phase 1: Estimation of the speckle patterns based on the acquired images
- Phase 2: Computational reconstruction of the object bases on the estimation of the speckle patterns

We will explore the main concept of the above mentioned two phases and we will skip a few steps but for a complete explanation you can refer to [97] especially if you are interested in the way to optimize the Tikhonov parameters or see how it performs compared to other reconstruction algorithms available in literature.

Phase 1:

To obtain a first estimation of the object that we want to recover, we take the mean of the stack of images that we acquired. We are going to derive the mean image and use the assumption that the illumination is homogeneous to derive the following equation:

$$\begin{aligned} I_{mean}(\mathbf{r}) = \langle I_l(\mathbf{r})^{illumination} \rangle_l &= \Big[\rho(\mathbf{r}) \cdot \langle p_l(\mathbf{r}) \rangle_l\Big] \circledast h_{detection}(\mathbf{r}) \\ &\approx \Big[\rho(\mathbf{r}) \cdot p_0\Big] \circledast h_{detection}(\mathbf{r}) \end{aligned} \tag{3.7}$$

where $\langle . \rangle_l$ denotes the average with respect to l and $p_0 \approx \langle p_l(\mathbf{r}) \rangle_l$ make use of the homogeneous illumination assumption. Looking at the result of equation (3.7), it tells us that doing the mean operation over the stack of images is equivalent to illuminate a given density of fluorophores ρ with a widefield illumination p_0 and detected with an objective whose PSF is $h_{detection}(\mathbf{r})$. We then deconvolve the object with the PSF and obtain a first approximation of the object that we will use in the next step: the speckle pattern estimation. We now want to find the speckle pattern that was shining the sample through an optimization algorithm with the following cost function $f(p_l)$ and a constraint on the Fourier support of that speckle pattern:

$$\begin{aligned} \min_{p_l} \; f(p_l) &= f_{diff}(p_l) + \mathbb{I}_C(p_l) \\ &= \sum_r \Big| I_l(\mathbf{r}) - [o_{est}(\mathbf{r}) \cdot p_l(\mathbf{r})] \circledast h_{detection} \Big|^2 + \mathbb{I}_C(p_l) \end{aligned} \tag{3.8}$$

where $f_{diff}(p_l)$ is the least square error between the measured image and the predicted image given the current estimation of the speckle pattern and $\mathbb{I}_C(p_l)$ is the Fourier support constraint according to:

$$\mathbb{I}_C(p_l) = \begin{cases} 0, & p_l \in C \\ +\infty, & p_l \notin C \end{cases}, \; C = \left\{ p_l(\mathbf{r}) \;\middle|\; \tilde{p}_l(\mathbf{u}) = 0, \; \forall \mathbf{u} > \frac{2NA}{\lambda_{illu}} \right\} \tag{3.9}$$

which means that if a spatial frequency of the reconstructed speckle pattern is outside of the disk limit by the Abbe diffraction limit in the Fourier space, the cost function takes $+\infty$ penalty leading to another iteration to find a better minimum to the cost function in equation 3.8. This constraint is very important to ensure that the reconstructed speckle is diffraction limited.

Phase 2:

In this phase, the focus will be put on reconstructing the object and find out what resolution can be achieved. After execution of phase 1, we now have a reconstructed speckle pattern and the stack of raw images acquired experimentally. Intuitively, we can guess that when there is a high signal in the raw image and a high signal in the

reconstructed speckle there is a high probability that the object is there. Furthermore, it can be further confirmed if a large number of raw images are showing the same behavior. Moreover, when for some reason there is a peak in the reconstructed speckle due to a poor reconstruction, it is then mitigated because it is not further confirmed by the stack of images and vice versa. That is why the algorithm will use the covariance of the raw stack of images and the reconstructed speckle patterns with the assumption that they are two random variables for a given position $\mathbf{r}$. It can be written as follows:

$$\begin{aligned} I_{cov}(\mathbf{r}) &= \langle \Delta p_l(\mathbf{r}) \cdot \Delta I_l(\mathbf{r}) \rangle_l \\ &= \iint o(\mathbf{r}') \langle \Delta p_l(\mathbf{r}) \Delta p_l(\mathbf{r}') \rangle_l \cdot h_{detection}(\mathbf{r} - \mathbf{r}')\, d^2\mathbf{r}' \\ &= p_0 \iint o(\mathbf{r}') \cdot h_{cov}(\mathbf{r} - \mathbf{r}')\, d^2\mathbf{r}' \end{aligned} \tag{3.10}$$

where $\Delta I_l(\mathbf{r}) = I_l(\mathbf{r}) - \langle I_l(\mathbf{r}) \rangle_l$, $\Delta p_l(\mathbf{r}) = p_l(\mathbf{r}) - \langle p_l(\mathbf{r}) \rangle_l$ and $h_{cov}(\mathbf{r} - \mathbf{r}') = \langle \Delta p_l(\mathbf{r}) \Delta p_l(\mathbf{r}') \rangle_l \cdot h_{detection}(\mathbf{r} - \mathbf{r}')$.

From the last part of equation 3.10, we can see that the resolution is determined by the so-called h_{cov} which itself depend on the product of $h_{detection}$ and the spatial correlation between the speckle patterns used to illuminate the sample. If they are perfectly correlated then $\langle \Delta p_l(\mathbf{r}) \Delta p_l(\mathbf{r}') \rangle_l = K$ and thus the regular resolution limit for widefield illumination microscopy $h_{detection}$ so it is diffraction limited. On the contrary, if the patterns are perfectly uncorrelated $\langle \Delta p_l(\mathbf{r}) \Delta p_l(\mathbf{r}') \rangle_l = \delta(\mathbf{r} - \mathbf{r}')$ the PSF h_{cov} becomes a delta function. Consequently, it is central to know what the spatial correlation is for our setup since it determines the achievable spatial resolution. As it is demonstrated in [97], it can be written as follows:

$$\langle \Delta p_l(\mathbf{r}) \Delta p_l(\mathbf{r}') \rangle_l \propto \Big(h_{illumination} \star h_{illumination} \Big)(\mathbf{r} - \mathbf{r}') \tag{3.11}$$

where $\star$ is the autocorrelation operator and together with equation 3.10 lead to the following final equation:

$$\begin{aligned} I_{cov}(\mathbf{r}) &= \langle \Delta p_l(\mathbf{r}) \cdot \Delta I_l(\mathbf{r}) \rangle_l \\ &\propto \iint o(\mathbf{r}') \underbrace{\Big[(h_{illumination} \star h_{illumination}) \cdot h_{detection} \Big](\mathbf{r} - \mathbf{r}')}_{h_{cov}(\mathbf{r} - \mathbf{r}')}\, d^2\mathbf{r}' \end{aligned} \tag{3.12}$$

Where we denote $h_{cov} = \Big(h_{illumination} \star h_{illumination} \Big) \cdot h_{detection}$ the PSF of the reconstructed image. Since we have $FWHM_{cov} < FWHM_{det}$, where $FWHM$ stands for Full Width at Half Maximum of the PSFs, Yeh et al. blind-SIM algorithm is able to retrieve resolution beyond the diffraction limit.

We have seen in this section how a blind-SIM algorithm works and the assumptions that are made to required to it. In the next section, we will use the reconstruction

algorithm on simulated data.

3.1.4 Simulations results

To ensure blind-S^3 could reach a higher resolution than the conventional methodology, we made some simulations to have a well controlled environment. We are going to image a Siemens star, which is a conventional object to use to asses the resolution capabilities of a technique. Indeed, the shape of it makes it so that a high spatial frequency content is located at the center of the image and progressively reduced to lower spatial frequency on the edge of the image while respecting a radial symmetry which is prevalent in optics. A raw Siemens star pattern is shown on the left of Fig.3.3. We will simulate an imaging process using the conventional SRS and blind-S^3 methodology in order to compare them. In the conventional methodology case, we computed the convolution product between the Siemens star and the product of the PSFs of the Stokes and Pump beams. In the blind-S^3 case, we previously derived the equation for the forward model (equation.3.3) that we are going to use to create the stack of images needed to use the blind-SIM algorithm. To break it down, we shine the Siemens star object with 335 speckles realizations meaning we do a dot product between each speckle realization and the object. Then we compute the convolution of each of this dot product with the PSF of the Stokes to obtain one blind-S^3 realization. And finally, we provided these images to the reconstruction algorithm. The result is shown in the Fig.3.3. and we can clearly see an improvement in the resolution of the blind-S^3 reconstruction compared to the conventional SRS. The red circle corresponds to the limit of diffraction for conventional SRS and the dashed blue circle corresponds to the resolution limit reached by the blind-S^3 technique. More precisely, the ratio of the red diameter and the blue diameter is very close to the theoretical value of $\sqrt{2}$ which is the expected improvement in resolution.
As demonstrated in the above two sections, we developed a new methodology that fits into a well known mathematical framework and according to the good result in simulation would pave the way to realize an experimental super resolution image in a label-free manner.

3.2 Proof of principle on calibrated sample

After demonstrating in simulation that the technique could work, we moved to the most challenging and laborious part: the experimental demonstration. Indeed, it was very time consuming to develop the first SRS microscope in the group with a laser source that is not well adapted for the experiment. We will develop later in the chapter what new source will be used in the future for this microscope in order to go beyond what

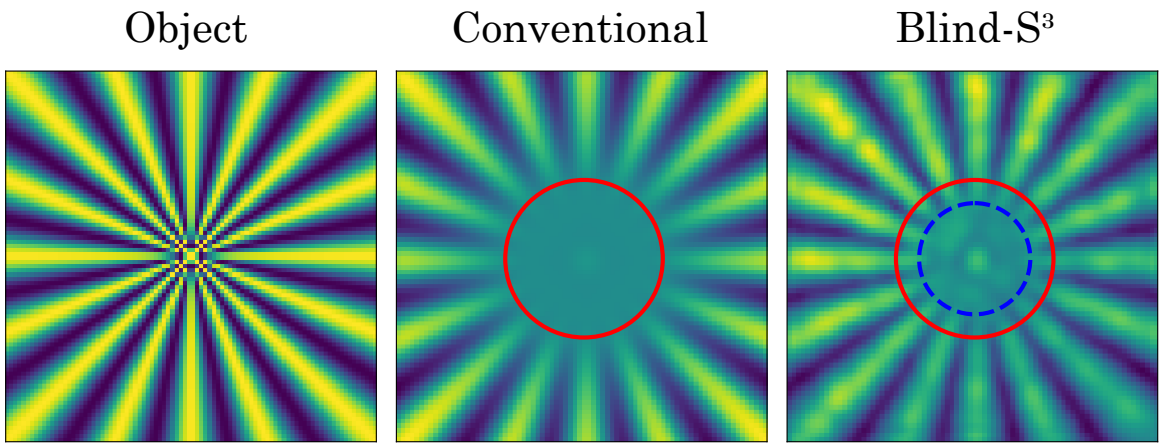

Figure 3.3: **Resolution comparison between conventional SRS and blind-S^3 in simulation**. On the left, the Siemens star object used for the simulation. In the middle, conventional SRS image and on the right blind-S^3 technique applied to a Siemens star object. The red circle represent the diffraction limit for conventional SRS and the blue circle represent the achieved resolution for the blind-S^3

has been achieved during this PhD thesis. In this section, we will be using plastic samples and more precisely well calibrated polystyrene beads.

3.2.1 Transverse resolution

We first want to demonstrate the super resolution experimentally which was a very challenging task. As a matter of fact, in the literature, an extensive work has been achieved in simulation for label-free super resolution techniques but fewer experimental realizations exist and none with plastic samples as we will demonstrate here (see section 3.4). In fact, we noticed that these plastic bead samples were more sensitive to excessive power than biological samples imaged in the later sections.

To this end, we started to image beads larger than the diffraction limit of the conventional SRS. Indeed, we need to make sure the reconstruction algorithm works properly with experimental images which are much more noisy than the simulations we made. We prepared samples of polystyrene beads with a diameter of 750nm and 1μm immersed in water. We imaged both sample with the conventional SRS and blind-S^3 so that we could ensure the fidelity of the reconstruction algorithm is high. As illustrated in Fig.3.4, we could confirm a high fidelity of the reconstruction with an improvement in resolution.

For the blind-S^3 images (right column in Fig.3.4), we can note a drop in signal the farther the beads are from the Green star which correspond to the center of the FOV. In fact, this is due to the static speckle illumination. Since the speckle beam has a Gaussian intensity envelope and the Stokes beam is scanning over it, it results in this

Gaussian shaped envelope in the reconstructed image. This is absent in conventional SRS (left column in Fig.3.4) since the two focused beams are scanned together along the whole image so the intensity in each pixel is the same. But this effect could be counterbalanced by engineering the beam profile into a flat top intensity distribution, for example by using a commercially available beam-shaping device [98].

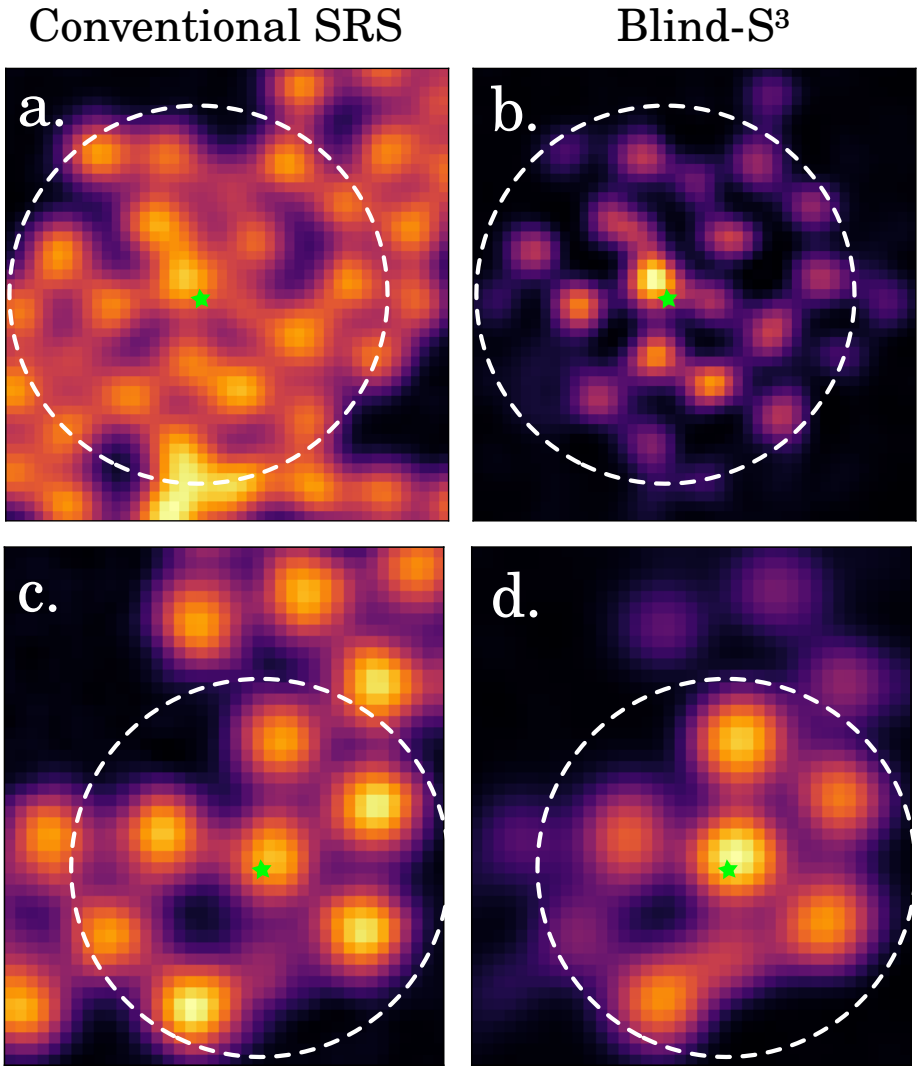

Figure 3.4: **Reconstruction of large polystyrene beads.**. Images of polystyrene beads of 750nm and 1μm diameter immersed in water and probed at Raman resonance 2903cm^{-1}. The white dashed circle represents the FOV of the blind-S^3 technique, highlighting the Gaussian envelope energy distribution of the fixed speckle patterns. The green star is the center of the white dashed circle. **a.** Conventional SRS on 1μm polystyrene beads. **b.** Blind-S^3 on 1μm polystyrene beads. **c.** Conventional SRS on 750nm polystyrene beads. **d.** Blind-S^3 on 750nm polystyrene beads.

In super-resolution microscopy it is not straightforward to compare the recon-

structed images with a "ground truth" object. A well calibrated target can be used but they are generally not usable for label-free technique. Moreover, the FOV in blind-S^3 is determined by the speckle envelope, as previously mentioned, which is much smaller than the FOV the conventional SRS microscopy can reach. To overcome this small envelope issue, and assess whether there was a true super-resolution for particles that were below the best resolution achieved in conventional SRS, we have developed a strategy to confirm super-resolution. We imaged commercially available calibrated polystyrene beads of various sizes, which are well-known to aggregate and form close-packed structures. Therefore, we can use the bead close contact distance as a proxy for the bead diameter. We measured the close contact distances of several beads for several sizes ranging from smaller than to several times the resolution limit, and also for two different objectives with different NAs. The objective was to make sure the retrieved diameter is close to the nominal diameter of the bead given by the manufacturer. Each data point on the graph is an average between 3 to 6 close contact distances. Although the method is somewhat subjective, we were careful to chose "spot centers" that indeed seemed in close contact. Following this procedure, we noticed that maximum spot-to-spot center were indeed limited by the bead size, that is, in the 350 nm bead diameter we did not see any 240 nm spatial fluctuations. The outcome of this procedure is shown Fig. 3.5 and the agreement between the nominal bead diameter and the retrieved diameter further confirms that the features observed in the blind-S^3 reconstructions indeed correspond to physical features.

Now that we confirmed the technique works well experimentally, we can image much more difficult samples that is too say a sample under the diffraction limit of the SRS microscope. To this end, we prepared a sample of polystyrene beads with a diameter of 239 nm immerse in deuterated water to prevent the Raman resonance of dionized water from bringing up the background signal (see section 2.3.1 for more details) and imaged it with the two modalities. Now, we demonstrate the improvement in the transverse resolution by imaging 239nm diameter beads thus surpassing the diffraction-limit of usual SRS microscopy. In order to evaluate the gain in resolution, we compared blind-S^3 to the conventional scanning methods. For conventional SRS, the theoretical transverse resolution is $\Delta r^{Conv} = 307$ nm. This theoretical value is technically challenging to achieve with high numerical aperture (NA) objectives in the near-IR because the wavelengths of the two beams differ by hundreds of nanometers (spectral span necessary for fast quantification of lipids, proteins, and nucleic acids in SRS microscopy). Conversely, blind-S^3 transverse spatial resolution results from the doubling in resolution dictated by SIM and the speckle grain size limited by diffraction, leading to $\Delta r^{blind\ S^3} = 217$ nm (see section 1.3.4 for more details). Clearly, conventional SRS (Fig.3.4a.) cannot resolve the beads transversely as the bead size is smaller than the theoretical resolution limit. On the other hand, after multiple speckle pattern illuminations, we feed the resulting images to the blind SIM algorithm to reconstruct

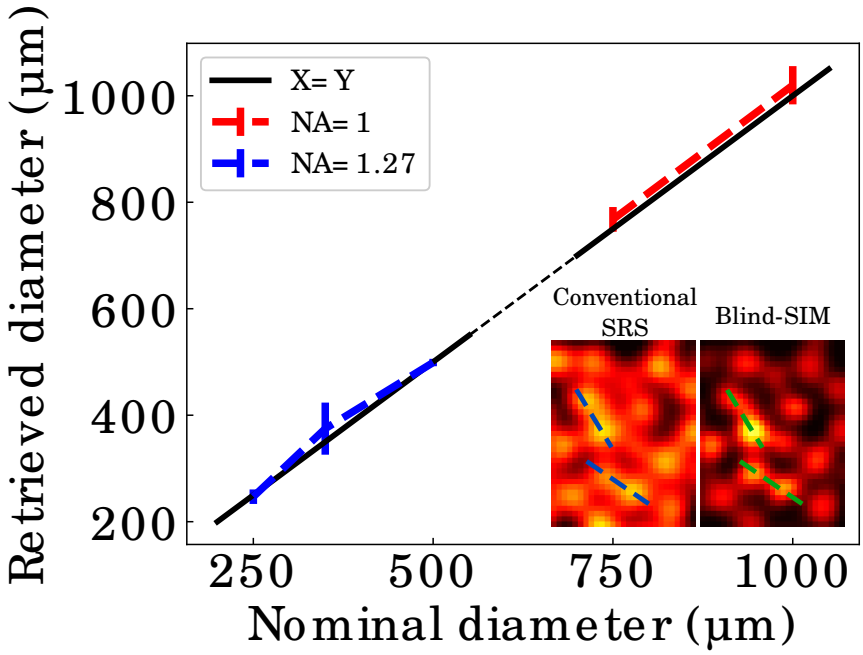

Figure 3.5: **Transverse resolution analysis for blind-S^3 on several polystyrene diameter sizes**. Outcome analysis of the images of various close-contact beads pairs: We use close-contact distances as a proxy for the bead diameter. The inset shows representative images used for analysis, with the dashed lines representing some of the beads chosen for evaluation.

a super-resolved image. Notably, blind-S^3 methodology (Fig. 3.4b.) resolves several beads in the in-focus layer. The line profiles reveal the distance between the centers of the beads (242 nm) which matches well to the distance of close contact between two beads.

We note that the effective region-of-interest (ROI) of blind-S^3 is modulated by the speckle envelope, hence decreasing the similarity of the two images in the edges of the bead cluster as aforementioned, yet not affecting the resolution gain (a resolution quantification of multiple beads size and NA is presented in Fig.3.5). The present findings show that the blind-S^3 methodology goes beyond the fundamental far-field diffraction-limit resolution of SRS microscopy, by improving the resolution $\geq \sqrt{2}$.

3.2.2 Axial resolution

To further characterize the technique, we will roughly estimate the Z-resolution of the microscope. We image a 2 layer structure of 500 nm polystyrene beads for multiple z-positions. The outcome of the SIM algorithm is presented in Fig. 3.7 for two layers separated by 1000 nm depth. The conventional SRS resolves the two layers, since

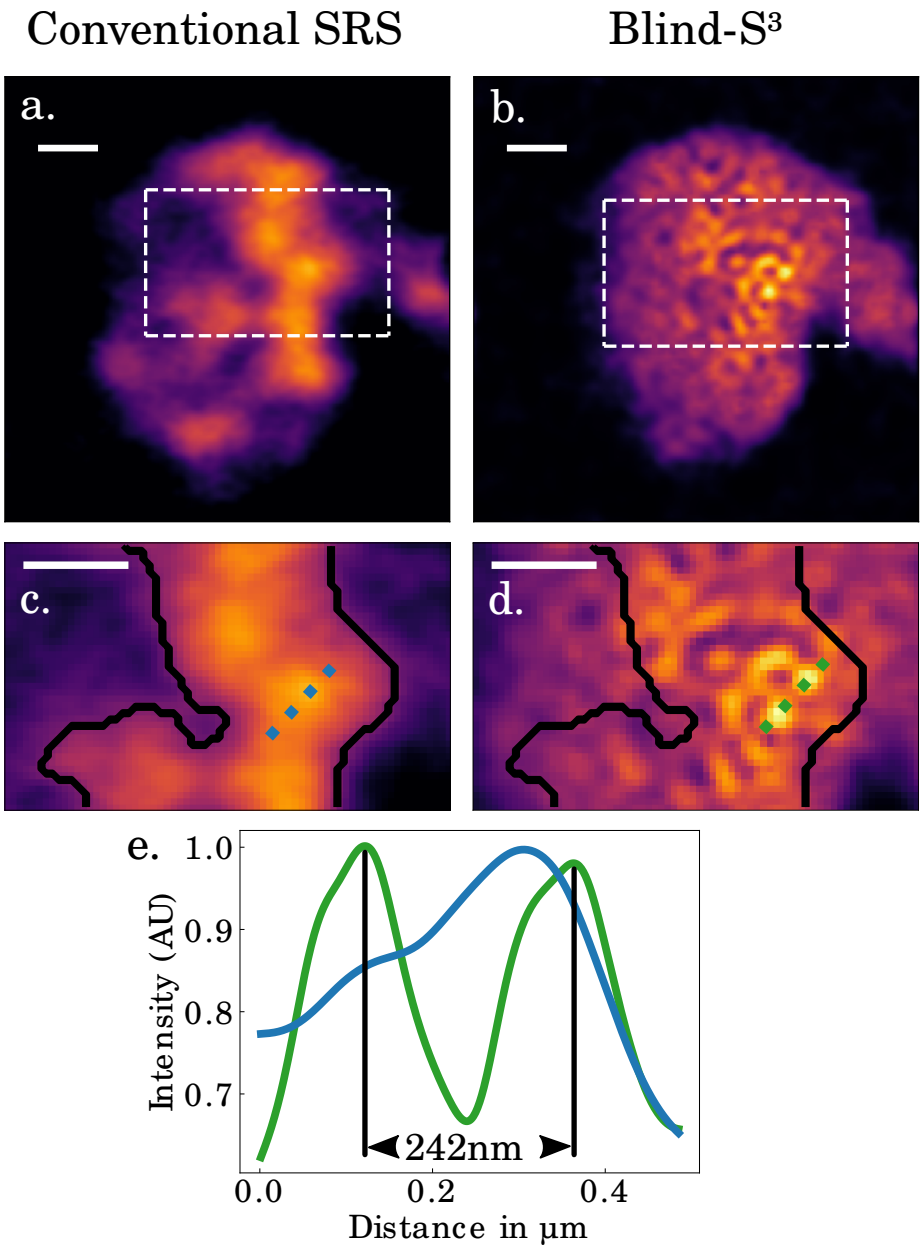

Figure 3.6: **Experimental transverse resolution comparison between conventional SRS and blind-S^3 showing super resolution on polystyrene beads.**. Images of polystyrene beads of 239nm diameter immersed in deuterated water and probed at Raman resonance 2903cm^{-1}. **a.** Conventional SRS large FOV. **b.** Blind-S^3 large FOV. **c.** Conventional SRS from dashed line in **a.** **d.** Blind-S^3 from dashed line in **b.** **e.** Line profil from the dashed line **c.** and **d**. The blue line corresponds to the conventional SRS and the green line corresponds to the blue line. The 242nm distance between the two tops in green is close to the nominal diameter of 239nm beads. All scale bars: 500 nm

they have different morphology, which is coherent with the resolution of conventional SRS $\Delta z_{SRS} = \Delta z\sqrt{\sqrt{2}-1} = 718nm$ (with $\Delta z = \frac{2\lambda}{NA^2}$). Therefore, we infer that the blind-S^3 longitudinal resolution is to the best similar and in any case not too far to the conventional SRS given the similar morphology of the retrieved images while being close to the theoretical diffraction limit of standard SRS.

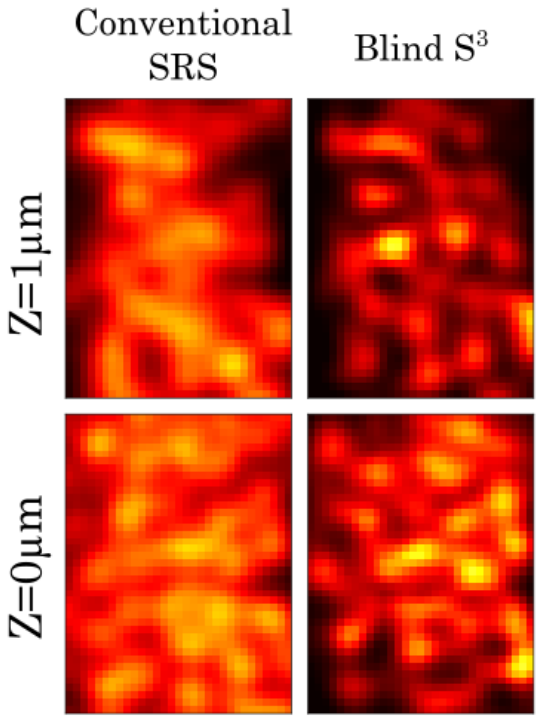

Figure 3.7: **Sectioning experiment in a thin film of oil**. (left panel) The dashed blue curve is the SRS signal of a z-scanned thin-film. The green curve correspond to the blind-S^3 signal of a z-scanned thin-film and it is an average of multiple speckle realizations. (right panel) Extracted FWHM for the simulation (dash) and experimental data (line) vs the relative transverse FOV diameter which is linked to the macro-pixel size of the random phase on the SLM.

3.2.3 Sectioning

One key feature if one wants to use a super resolution technique in biology is sectioning (see section 1.5). Sectioning is the ability to reject signal from layers above and under the focus thus preventing them to contribute to the background signal resulting in a higher signal to noise ratio (SNR). Remarkably, and contrary to conventional wide-field imaging, super-resolution in blind-S^3 comes with intrinsic high z-sectioning capabilities. In each illumination during the blind-S^3 procedure, an image is formed based on a

wide-field geometry model in the transverse plane, that is, an object is convoluted with a linear point-spread function (PSF) (see equation 3.3). In the conventional wide-field microscope using multi-pixel cameras, the acquisition procedure is not able to effectively reject the signal from out-of-focus region, therefore deteriorating image quality and resolution due to the background noise (shot-noise). Conversely, in blind-S^3 the nonlinear optical response is local in the longitudinal direction, because SRS signals are only nonlinearly generated within the overlap region of the two beams, hence each SRS image illumination does not contain appreciable out-of-focus noise. To demonstrate the sectioning capabilities of blind-S^3, we probed a thin film of oil (few μm) by scanning it in the longitudinal direction. Note that we collect the signal that is generated for each z-position on a ≈10 mm-wide detector, hence, not in a confocal geometry. Clearly, conventional SRS and blind-S^3 give a peaked response which means that those two techniques have inherent longitudinal sectioning (Fig. 3.8 left). Indeed, the conventional SRS microscope is able to show such z-sectioning capability, due to its nonlinear longitudinal PSF. But contrary to conventional SRS, in blind-S^3 the z-

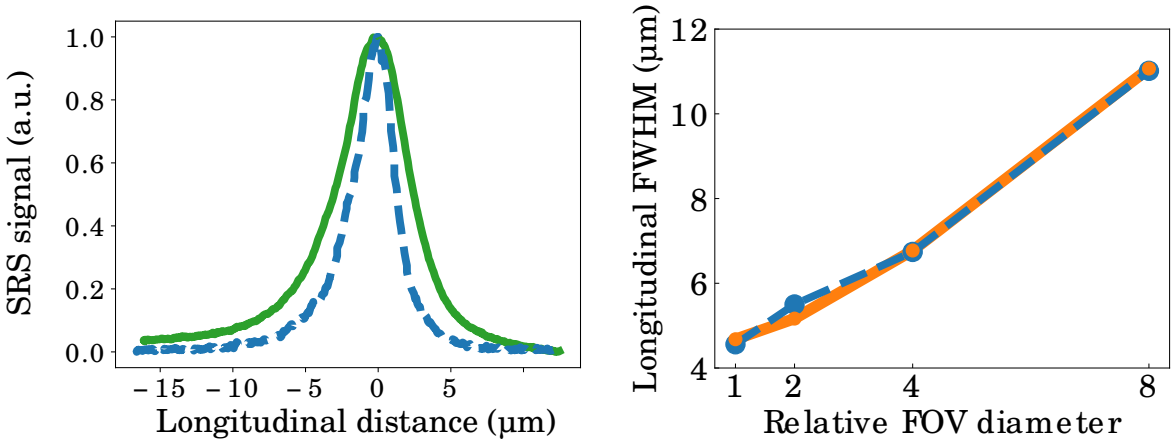

Figure 3.8: **Sectioning experiment in a thin film of oil**. (left panel) The dashed blue curve is the SRS signal of a z-scanned thin-film. The green curve correspond to the blind-S^3 signal of a z-scanned thin-film and it is an average of multiple speckle realizations. (right panel) Extracted FWHM for the simulation (dash) and experimental data (line) vs the relative transverse FOV diameter which is linked to the macro-pixel size of the random phase on the SLM.

sectioning is coupled with the effective field-of-view (FOV), with a weak dependence, since the speckle envelope in the transverse direction is coupled with the longitudinal one (See Fig.3.8 right). For the same reason as the increase of the spread of the speckle, which corresponds to an increase of the FOV, we decrease the sectioning ability. This is why we can see on Fig.3.8. that the sectioning for conventional SRS (blue dashed curve) is greater than the blind-S^3 (Green curve). Depending on the application, a

comfortable trade-off has to be found if no additional step is taken. Otherwise, the combinaison of the blind-S^3 technique with temporal focusing could enable to ease the trade-off [99].

To further confirm this relationship between FOV and sectioning, we derive an analytic expression for explaining the sectioning ability of blind-S^3. We assume two superposed Gaussian beams with electric fields E and $\tilde{E}$ at two different wavelengths, and corresponding beam waist ω_0 and $\tilde{\omega_0}$, Rayleigh range Z_R and $\tilde{Z_R}$. The two beams z-scan a continuous thin film containing Raman active centers ρ with a thickness d. The total signal detected S_{sect} can be calculated as:

$$\begin{aligned} S_{sect}(z) &= \iiint \rho(x',y',z')|E(x',y',z')|^2|\tilde{E}(x',y',z')|^2\,dx'\,dy'\,dz' \\ &= \frac{\pi}{2}\int_{z-d/2}^{z+d/2} \rho(z')\frac{\omega_0^2\tilde{\omega}_0^2}{\omega_0^2+\tilde{\omega}_0^2+z'^2(\frac{\omega_0^2}{Z_R^2}+\frac{\tilde{\omega}_0^2}{\tilde{Z}_R^2})}\,dz' \\ &= \frac{\pi\omega_0^2\tilde{\omega}_0^2}{2\sqrt{(\omega_0^2+\tilde{\omega}_0^2)(\frac{\omega_0^2}{Z_R^2}+\frac{\tilde{\omega}_0^2}{\tilde{Z}_R^2})}}\cdot \\ &\left[\arctan\left((\frac{d}{2}-z)\sqrt{\frac{\frac{\omega_0^2}{Z_R^2}+\frac{\tilde{\omega}_0^2}{\tilde{Z}_R^2}}{\omega_0^2+\tilde{\omega}_0^2}}\right)-\arctan\left((-\frac{d}{2}-z)\sqrt{\frac{\frac{\omega_0^2}{Z_R^2}+\frac{\tilde{\omega}_0^2}{\tilde{Z}_R^2}}{\omega_0^2+\tilde{\omega}_0^2}}\right)\right] \end{aligned} \tag{3.13}$$

.

Comparison between the data and this simplified model shows a remarkable agreement, despite the fact that the rapid fluctuations of the speckle are not taken into account — that is, we do not use Eq. 3.2 for computing the average response from multiple speckle realizations, due to its high computational cost. In order to compare with the model, we have z-scanned a thin film in a blind-S^3 acquisition procedure, and averaged over all realizations, for various FOV controlled by the number of independent macro pixels shown in the SLM (Fig. 3.8). We extracted the full-width-at-half-maximum (FWHM) of each FOV and compare them with simulations using Eq. 3.13 and plotted them in Fig. 3.9 The agreement between the coarse approximation (which does not take into account the sharp fluctuations of the speckle, and neither the nonlinear polarization in the SRS process) and the experimental data describes very well the dependence of the transverse FOV with the sectioning capabilities.

In summary, we showed in this section that it was experimentally possible to do super resolution imaging in a label free manner. We paid a close attention to ensuring the reconstructed imaged were well representative of the reality and then demonstrated the super resolution capabilities of the technique. Finally, we focused on some of the interesting intrinsic features of this new method and especially the sectioning ability which is so crucial for many biological imaging applications.

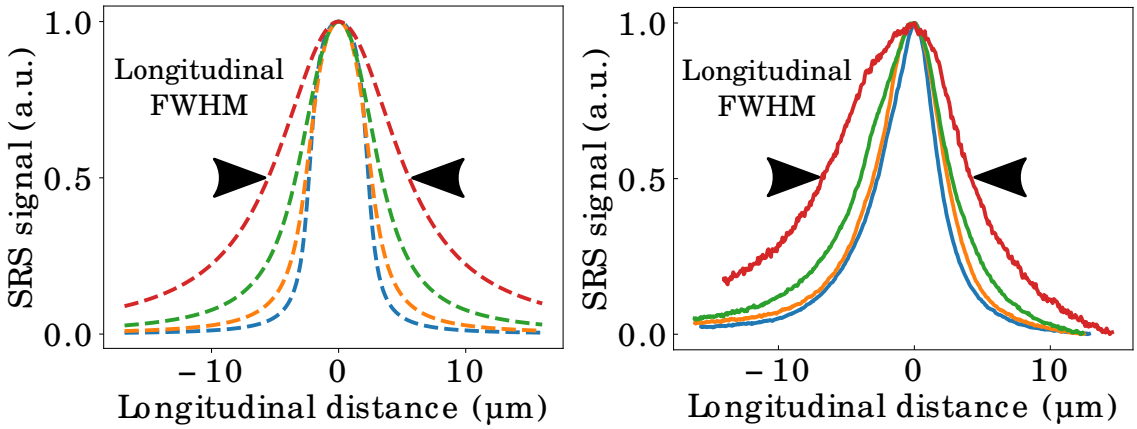

Figure 3.9: **Depth sectioning analysis**. (left panel) SRS signal of a z-scanned thin-film for various transverse FOV. Each curve is an average of multiple speckle realizations. (middle panel) Simulation of an SRS-equivalent process (see text and Eq. 3.13 development).

3.3 Demonstration of compatibility with biological tissues

Now that we demonstrated super resolution and sectioning capabilities, the next challenging piece of experiment is to apply the methodology to real and uncalibrated biological tissues. Indeed, as we will see in the next section, there are some works on label-free super resolution and biological tissues but there is no experimental demonstration of a truly label-free super resolution technique working on such type of tissues. To that end, we decided to first use the technique on 'thin' samples like HeLa cells — meaning mostly 2D sample with not a too complex structure. Then, we imaged more complex samples from mouse brains which we can consider as 3D structures meaning that there are molecules with Raman active resonances anywhere in the 3D volume thus the signal can come from lower or upper layer from the focus.

3.3.1 HeLa cell imaging

In this section, we demonstrate blind-S^3 compatibility with biological specimens by imaging standard cell lines.

Conventional SRS reveals several μm-large droplets within the cell in the FOV (Fig. 3.10a). The microscope is set on the 2958cm^{-1} Raman resonance. Indeed, it corresponds to a CH stretch present in lipids, proteins and DNA. Based on previous literature, these images are a proxy to the local concentration of lipid in the cell which means that we are observing large lipid droplets. An overview of the cell that we

image is depicted in Fig.3.10.a. where the two white dashed rectangles are close-up images. These images show different cluster morphologies (Fig. 3.10b. and c.), and

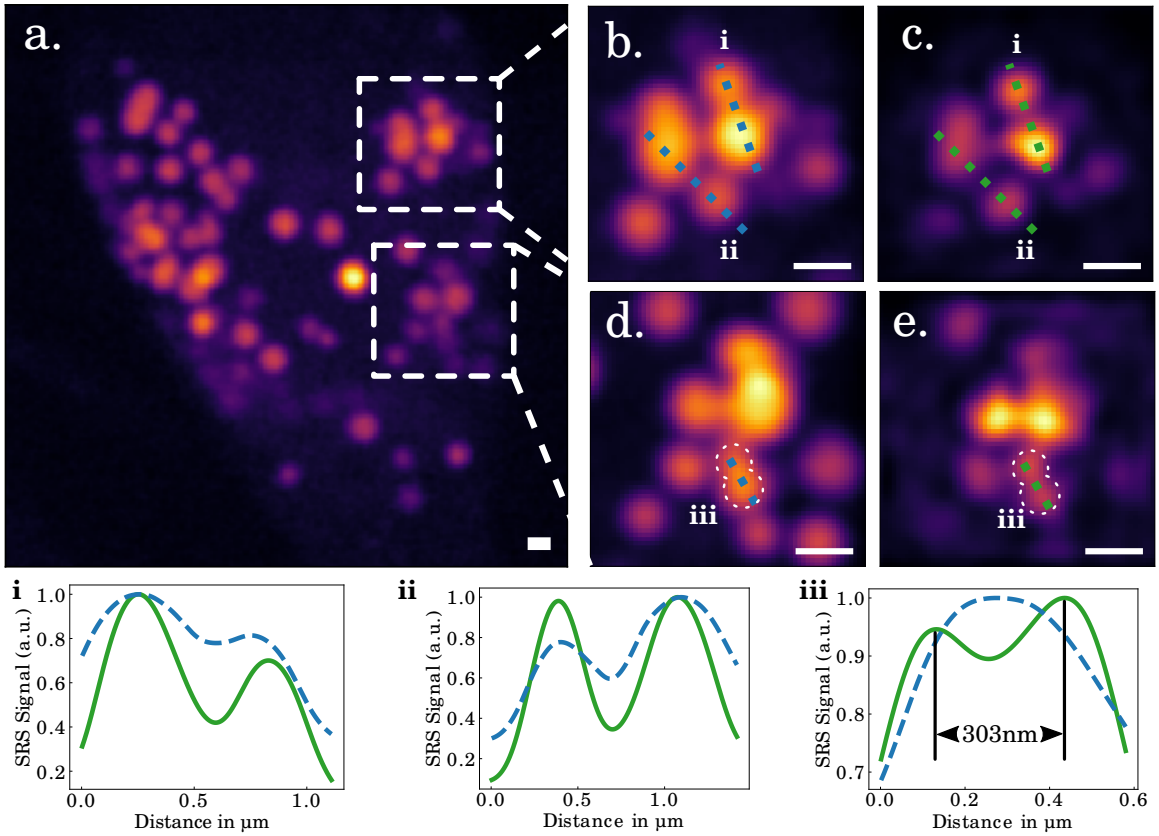

Figure 3.10: **Label-free HeLa cells images in conventional and blind-S^3.** (**a**) Macroscopic view of the Hela cell sample. The region highlighted in dashed white rectangles are close-up in (**b**), (**d**) and (**c**), (**e**) for conventional SRS and blind-S^3 respectively. Blue dashed lines in (**b**), (**d**) and green dashed lines in (**c**), (**e**) are the line profiles corresponding to conventional SRS and blind-S^3 respectively. Line profiles from (**b**) and (**c**) are depicted in (**i**), (**ii**) and lines profiles in (**d**) and (**e**) are depicted in (**iii**). All scale bars: 500 nm.

we can clearly notice an increase in transverse resolution with blind-S^3 from the line profiles of selected ROI (Fig. 3.10i, ii, iii). Notably in 3.10.e., we manage to resolve two beads that are indistinguishable in 3.10.d. even if we could guess that there were two droplets since the shape is too elongated to be a single droplet (dashed with circles). The distance between the two droplets is just under the diffraction limit of standard SRS but it is clearly not able to resolve. It highlights again the fact that it is very hard to have a standard SRS microscope in the infra red that is diffraction limited.

Finally, as explained previously, we can notice the Gaussian envelope in the blind-S^3 images. We can clearly see that in Fig.3.10.c., the center of the Gaussian envelope

is somewhere along the line profile "i". And that is why it seems like the lower left droplet is almost extinguished on the image compared to standard SRS. The image in Fig.3.10.a. was taken after b. and c. and it shows that the technique is able to perform imaging without doing structural photo-damages on the sample.

3.3.2 Mouse brain imaging

Now, we will image more complex biological structure. In mouse brain tissues, we target the cerebellum — blue dashed rectangle — where there is a lot of lipidic content such a myelin which surrounds the axon of the neuron. We will image myelin sheaths in an opaque region of the sample as it is shown in dashed red rectangle in Fig.3.11.a. where we see that in bright field microscopy we have a white colored region. Indeed, the white color of the mouse brain part is an evidence of high scattering in that region. Another important feature of mouse brain tissues is that in the 3D volume of the sample. This means that there are a lot myelin filaments going in any direction and any depth. And since we set the Raman resonance to lipid active Raman resonance (2958cm^{-1}), we would have signal coming from anywhere if there were no sectioning at all.

So, to demonstrate capabilities for aberrant and opaque tissues, we imaged highly scattering brain slices at 8 μm-deep in the sample (Fig. 3.11.c-d) and we make sure that there are some myelin structured in the layers below and above the focal plane. We then acquire an overview of the region in conventional SRS Fig.3.11.b. and we zoom in the region dashed in white and compare conventional and blind-S^3 in a close-up image. As shown in Fig.3.11.e., the line profiles that are taken from the blue and green dashed lines in (**c**) and (**d**) demonstrate an increased resolution power of the myelin structures. Moreover, the close-up images with super-resolution capabilities (Fig. 3.11d) reveal that the structure of the myelin in the tissue is actually not as symmetrically perfect as inferred from the low-resolution images. These structures are apparently typical from ex-vivo myelin structures that aged before being imaged [100]. These results show that the method is compatible with thick tissue imaging, despite being opaque.

As we can see from the line profiles in 3.11.e., the conventional SRS is able to resolve the first feature of those two myelin sheaths in close contact. However, it is unable to resolve the second feature while the blind-S^3 goes beyond the resolution of standard SRS but the feature under study is still larger than the diffraction limit. We did not manage to find and image features below the diffraction limit of the standard SRS. Nevertheless, we showed here that the blind-S^3 is capable of imaging in a complex volumetric biological tissue while maintaining high resolution ability.

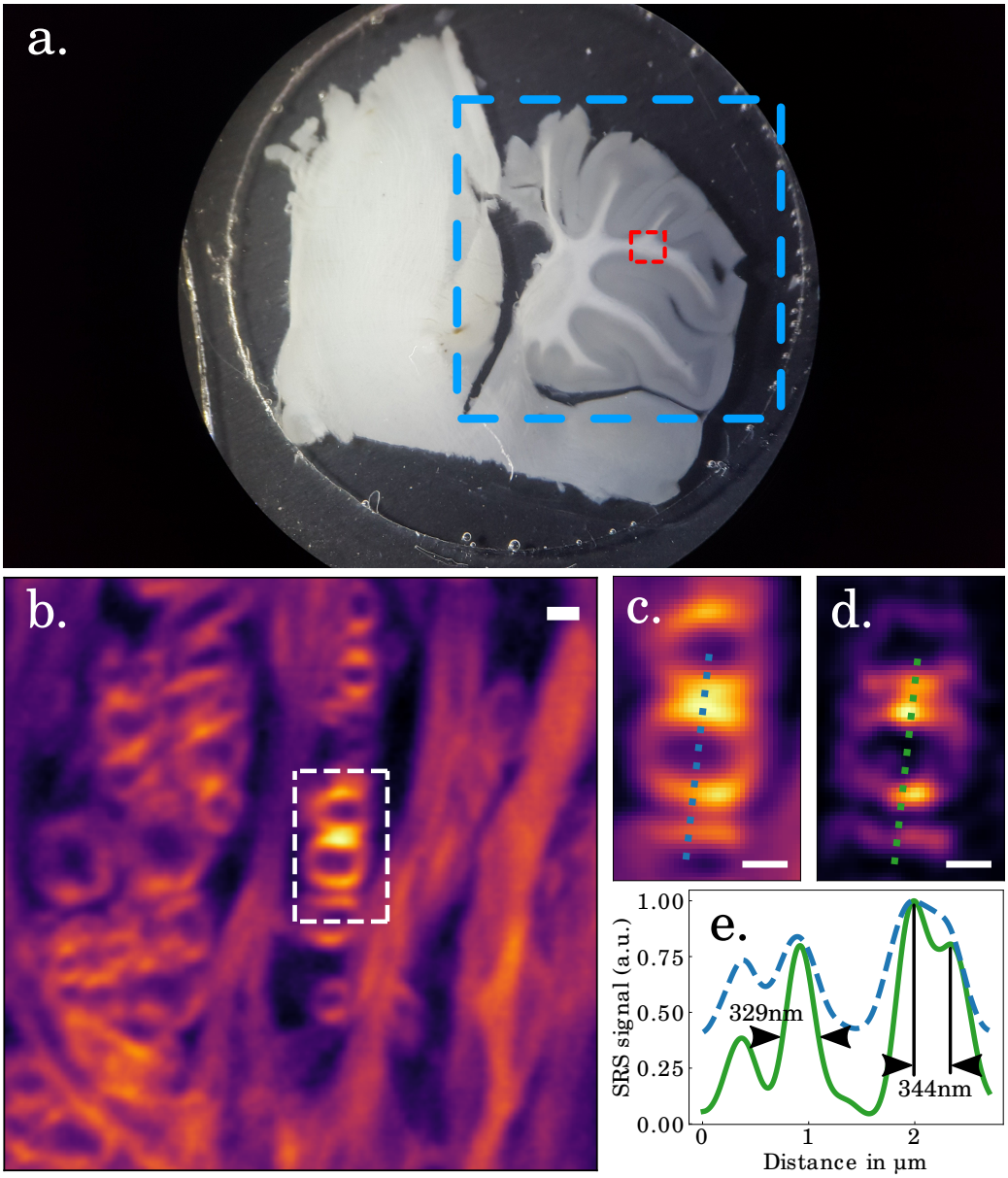

Figure 3.11: **Label-free mouse brain images in conventional and blind-S^3.** (**a**) Macroscopic view of the mouse brain sample. The blue dashed line depicts the cerebellum of the mouse brain. The region highlighted in dashed red corresponds to the type of zone imaged below. The dashed rectangle here is not at scale with the images below. (**b**) Large FOV image of opaque 100 μm thick mouse cerebellum (conventional SRS). A zoomed-in ROI is depicted by dashed boxes with conventional SRS (**c**) and blind-S^3 (**d**) methods, with a line profile chosen (**e**) for conventional (dashed blue line) and blind-S^3 (Green line) methods. All scale bars: 500 nm.

3.4 Discussion

Label-free super resolution using Raman scattering signals has been a decade long challenge as can be noted from table 1.1. At the beginning the topic was studied only theoretically but most of the approaches were based on CARS signal and STED-like methods which makes setup more complex. Later, experimental work showing super resolution was published but no biological tissues were done presumably because the need for high peak power could be phototoxic and induce photodamages. A very recent exception is Xiong et al. [80] where they do show super resolution in Raman excited fluorescence on E. Coli cells. However, the cells need to be stained with a specifically designed marker which has the energy level to mediate a Raman fluorescence transition. The marker is thus necessary in order to generate signal and thus it is not a truly label-free technique even though using Raman scattering. Here we proposed a technique enabling the combination of chemically selective and truly label-free super resolution technique.

However, there are some technical points that needs to be discussed. First, since the Pump beam is spread in a speckle pattern there is a loss in sensitivity of the method. While it is true for the raw images since there is a decrease by facto a 2 in the SNR (see Table 3.1), it does not hold for the final reconstruction since it is computationally improved as can be seen in Fig.3.12. In Fig.3.12, we show one speckle sample image a., one conventional b., and the final reconstruction of tissue c. (over 167 images) and an average of the conventional d. (over 65 images). On the other hand, sensitivity

	Raw speckle SNR	Raw SRS SNR
1	4.219	10.438
2	5.102	9.804
3	4.484	7.407

Table 3.1: Signal to noise ratio (SNR) for area of interest 1, 2 and 3 from Fig.3.12. respectively for a raw speckle realization and a standard SRS image. These images are extracted from the data showed in Fig.3.10.b top row.

could be improved through technical upgrades of the setup. Indeed, to narrow the spectrum of the beams we use classical frequency-domain spectral narrowing methods consisting in a set of grating and a DMD to spectrally narrow the Pump beam and a mechanical slit for the Stokes beam which through away a lot of energy. Therefore, the throughput is lower and it is limiting the FOV. Instead, spectral focusing could be used, thus making use of all the available power from the laser source [101]. We estimated that an increase of 50 times the current signal for our laser bandwidths since $\Delta I_{SRS} \propto \left(\frac{resolution\ bandwidth}{laser\ bandwidth}\right)^2$. Second, a lower repetition rate laser would enable

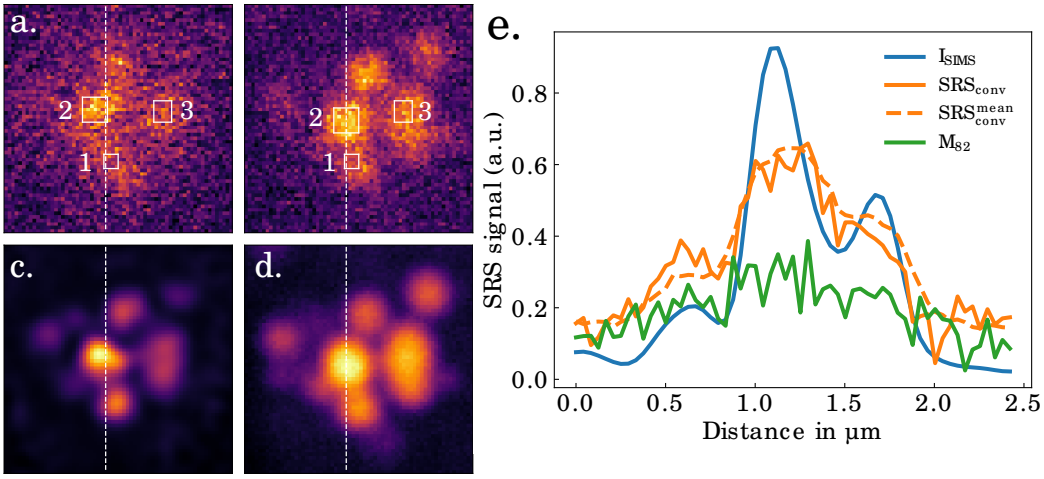

Figure 3.12: **Noise and sensitivity analysis.** Raw images of a single speckle a. and conventional SRS b. realizations for the HeLa cells specimens. These images are from the data shown in Fig.3.10.b top row. **c.** Reconstructed image for the blind-S^3 method. **d.** Average of **65** images for conventional SRS. **e.** Line profiles taken at the column depicted by the line in the images above. ROI 1, 2 and 3 are used to compute the SNR of the signal inside the boxes. The results are shown in Table.3.1

to greatly increase the signal but further characterization is needed since the laser stability of such a laser (even if it is not a fiber laser) can be worse than our current solid-state laser. Indeed, laser stability is a prominent concern for SRS microscopy since we measure ΔI_{SRS} with a LIA. It means that if the pulse to pulse energy fluctuates, an artificial signal could be created thus decrease signal sensitivity. Third, another concern that could be raised by the technique is the amount of unused power in the illumination plane. Indeed, the Stokes beam power is always fully used but the Pump beam power (speckle pattern) is only useful where the Stokes beam is located when it is scanning. In the experiments we did, we took the zoomed out image after both the conventional SRS and blind-S^3 were taken and no photodamage is visible. Nevertheless, with more powerful lasers it could be an issue but the following points need to be taken into consideration:

- the power density of the Pump beam is lower than for conventional SRS meaning that if we can do SRS we can probably do blind-S^3
- no effective linear photon absorption occurs in SRS contrary to linear fluorescence

In any case, if there were photodamages induced by the unused energy outside of the focal volume of the Stokes beam, one could use a DMD conjugated with the imaging plane to keep on the Pump beam where there is the focused Stokes beam. In the current form of the setup, this method would not slow down the acquisition since the pixel dwell time of the DMD (50μs) is shorter than the pixel dwell time of the images

taken in the manuscript. However, in an upgraded version with a lower repetition rate laser or with the implementation of spectral focusing, the pixel dwell time of the DMD could become the bottleneck. Now in terms of speed, the current technique is not video-rate but can be qualified as fast compared to other currently developed Raman super resolution techniques: pixel dwell time 150 μs $\times$ $(64px)^2$ $\times$ 150 images = 1minutes 30seconds which is to be compared to the 1h to 2h for spontaneous Raman super resolution on biological tissues [73].

More importantly, in general, widefield approaches lack of depth sectioning and it is even more important for Raman scattering super resolution than fluorescence since labeling sparsity cannot be controlled. As shown in Fig.3.9, the new sampling scheme enables sectioning but it also turns out that we can use standard blind-SIM algorithm to retrieve the object since the forward model is compatible (see section 3.1.2). Finally, contrary to other super resolution techniques for Raman scattering, the blind-S^3 is compatible with spectroscopy even if not showed in this PhD. Indeed, if the technique is controlling vibrational/electronic states to obtain super resolution, it drastically increases the complexity of the setup. On the contrary, blind-S^3 is compatible with spectroscopic measurement. The question is how to make use of the spectral information to use it efficiently in a reconstruction algorithm yet to be developed.

To conclude, we showed label-free super resolution in biological tissues by combining SRS and structured illumination reaching a factor $> \sqrt{2}$ resolution improvement. This factor can be greater for higher order nonlinear signal such as CARS. However, by squaring the speckle pattern ($I_{CARS} \propto I_{Stokes} I_{Pump}^2$) the sparsity of the speckle grains increases that implies that more images have to be taken to keep a uniform illumination. In the next chapter, we will explore what could bring CARS and some leads to reduce the number of images required for the acquisition.

Chapter 4

Speckle tailoring for Blind Structured Illumination Microscopy

We showed in the previous chapter that blind-S^3 was able to reach super resolution in complex biological tissues in a label-free manner. Now, we can wonder how to improve even further these results and a first idea could be to use higher nonlinear order signals.

The idea to go to higher nonlinear orders is not new and was applied in the fluorescence field when scientists thought about going from 2PF ($\sim$ 1200 nm) to 3PF ($\sim$ 1700 nm). Because higher order fluorescence signals mean longer excitation wavelength, it does not bring resolution enhancement. In fact, the higher order dependency brings more sectioning capabilities (reduction of out of focus signal) with the third power in intensity and it also improves the penetration depth since these wavelength are less scattered.

In the case of coherent Raman scattering, the same excitation wavelengths are used for SRS and CARS but the Pump intensity is squared in the case of CARS (see Equation 4.1). Indeed, SRS depends on the square of the incoming intensity while CARS is depending on the third power of the incoming intensity. Because the same wavelengths are used, a resolution improvement is expected for CARS compared to SRS. Plus, both signals are simultaneously generated as we saw in section 1.2.3 equation 1.9, therefore it does not require much experimental changes for anyone with a working SRS microscope since only the detection systems are different. Similarly to 3PF, the sectioning capabilities should be enhanced by the third order dependency on incoming intensity. On the penetration depth side, the wavelength used here are slightly lower than what would be used for 3PF (800 nm for the Pump beam and $\sim$ 1050 nm for the Stokes beam) but they are still in the NIR and could be moved further in the infrared as long as the beam are beating with the Raman resonance. One should not go to far in the infrared though since it would decrease the signal efficiency and increase the likelihood of exciting vibrational state directly from infrared light. Finally, using CARS, the illumination would correspond to a squared speckle pattern. Thus, it would correspond to nonlinear SIM which is known to bring higher resolution improvement [102] (see Fig.4.1). For all the reasons mentioned above, we decided to investigate label-free super resolution using blind-SIM applied to CARS images.

Nevertheless, the benefits mentioned above do not come without a cost. Indeed, even though CARS is label-free, the nonlinear dependency on $\chi^{(3)}$ makes it non trivial for quantitative imaging:

$$\begin{aligned} \Delta I_{SRS} &\propto |\chi_R^{(3)}| I_S I_P \\ I_{CARS} &\propto |\chi^{(3)}|^2 I_S I_P^2 \end{aligned} \tag{4.1}$$

where $\chi^{(3)} = \chi_R^{(3)} + \chi_{NR}^{(3)}$, $\chi_R^{(3)}$ and $\chi_{NR}^{(3)}$ are resonant and non-resonant nonlinear susceptibilities respectively.

We can see from these equations that I_{CARS} is proportional to $\chi^{(3)}$ and not $\chi_R^{(3)}$.

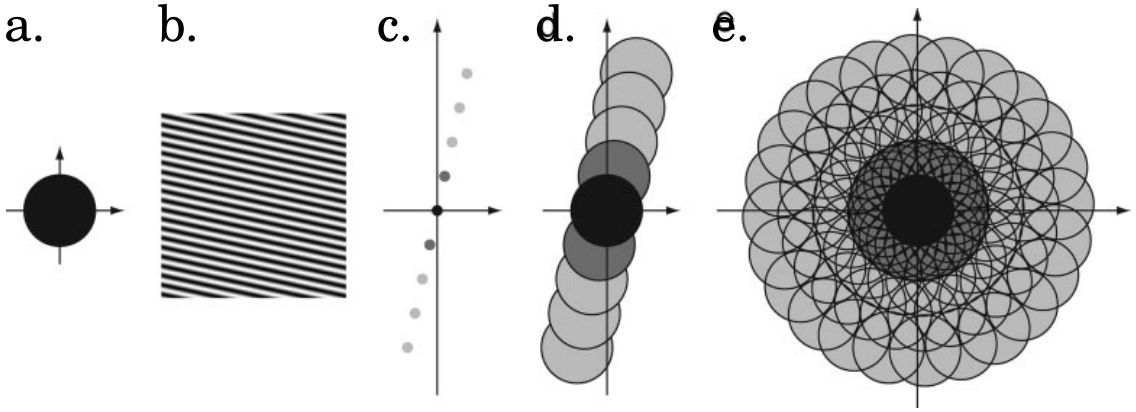

Figure 4.1: **Nonlinear SIM resolution improvement scheme.** a. The region of frequency space that is observable by conventional microscopy. b. An example of a sinusoidal illumination pattern. c. That illumination pattern has three frequency components: one at the origin (black), representing the average intensity, and two at $\pm k_1$, representing the modulation (dark gray). These are also the frequency components of the effective excitation under linear structured illumination. Under conditions of nonlinear effects a theoretically infinite number of additional components appear in the effective excitation; the three lowest harmonics are shown here (light gray). d. Observable regions for conventional microscopy (black), linear structured illumination (dark gray), and nonlinear structured-illumination microscopy (light gray) based on those three lowest harmonics. e. Corresponding observable regions if the procedure is repeated with other pattern orientations. The much larger region of observable spatial frequencies e. compared with that shown in a makes it possible to reconstruct the sample with correspondingly increased spatial resolution. Figure and caption extracted from [102].

Indeed, CARS-like signal is also generated by non resonant transitions interfering with the resonant signal which generates as a non resonant bakcground that lower the fidelity of the images at quantifying $\chi_R^{(3)}$. Finally, since I_{CARS} is proportional to $\chi^{(3)}$ a phase retrieval algorithms should be used to estimate and retrieve $\chi_R^{(3)}$.

In this chapter, we will elaborate on a strategy to shape the intensity speckle distribution to used blind-SIM with CARS. Then, we will study numerically how sensitive the shaping of the intensity distribution is to scattering since we want to apply super resolution in biological tissues. In addition, we will look at the effect of the shaping on the blind-SIM reconstruction algorithm. It should be stated that the results that are shown here are to be considered as preliminary.

4.1 Shaping speckle distribution

In the case of CARS, the signal depends quadratically on the Pump beam intensity, while the Stokes beam is linearly dependent on intensity (Equation 4.1). Since the Pump beam has a shorter wavelength, it is the one we want to use as a structured speckle pattern because in a scattering media it will end up into a speckle pattern faster anyway.

In general, speckle patterns satisfy the Rayleigh statistics in intensity distribution i.e. $e^{-\frac{I}{<I>}}$ which means that most of the object is illuminated with low intensities and in some regions there are "hot spots" of higher intensity i.e. the brightest speckle grains. When the speckle pattern is squared, the probability density function (PDF) is changed and the speckle pattern is even more "switched off" as can be seen in Fig.4.2 — it is more sparse. Indeed, we can see the exponentially decaying distribution of intensity of the squared speckle going down faster than the standard speckle pattern. Then, if one wants to use a second order nonlinear signal with a speckle pattern, it would make the illumination more sparse which can be seen as an issue in the case of blind-SIM. Naturally, a larger number of illuminations would be required in order to meet the condition of homogeneous illumination of the sample if one does not change the intensity distribution. To that end, it is desirable to customize the intensity statistics while keeping the speckle fully developed i.e. the same speckle grain size.

In the literature, there are several ways to achieve non-Rayleigh statistics. First, in the weak scattering regime, a speckle with a low contrast and a strong background is generated since the phase is not uniformly distributed [103]. Second, in the strongly scattering regime where the phases are uniformly distributed, it is possible to generate non-Rayleigh speckle by fluctuation of the total power either because of the transmission through the scattering media is altered by mesoscopic correlations [104] or because of the fluctuation of the intensity of the incoming beam [105]. In addition, by interfering two speckle patterns with fluctuating relative phases it is also possible to generate non-Rayleigh statistics [106]. However, even though these methods exhibit non-Rayleigh intensity distributions, each realization is a Rayleigh speckle combined with another Rayleigh speckle pattern resulting in a non-Rayleigh intensity distribution. Finally, as demonstrated by Cao et al. [107, 108], it is possible to arbitrarily design the intensity distribution from a Rayleigh speckle pattern by modulating the phase front of the incoming beam while the phase is uniformly distributed (see Fig.4.3). This is the method we chose to focus on. These non-Rayleigh distributions arise from the high order correlation of the fields in the Fourier space. However, some PDF cannot be generated because of the finite support of the spatial frequency and thus these PDF would be smoothed. Mainly, it is not possible to set the PDF to zero or make it discontinuous. Nonetheless in our case, the idea would be to counter balance the "squaring" effect by designing an intensity distribution that would have a Rayleigh distribution

when it is squared.

There are 3 categories to classify the type of speckle PDF: Rayleigh; sub-Rayleigh or super-Rayleigh. They are classified by the value of their contrast $C = \sqrt{\langle I^2 \rangle / \langle I \rangle^2 - 1}$ compared to 1. When a speckle pattern has a Rayleigh PDF, the contrast of that speckle pattern is 1. Sub-Rayleigh and super-Rayleigh PDFs are defined by a contrast < 1 or > 1 respectively.

In the next section, we will see how the algorithm works to design new intensity distributions.

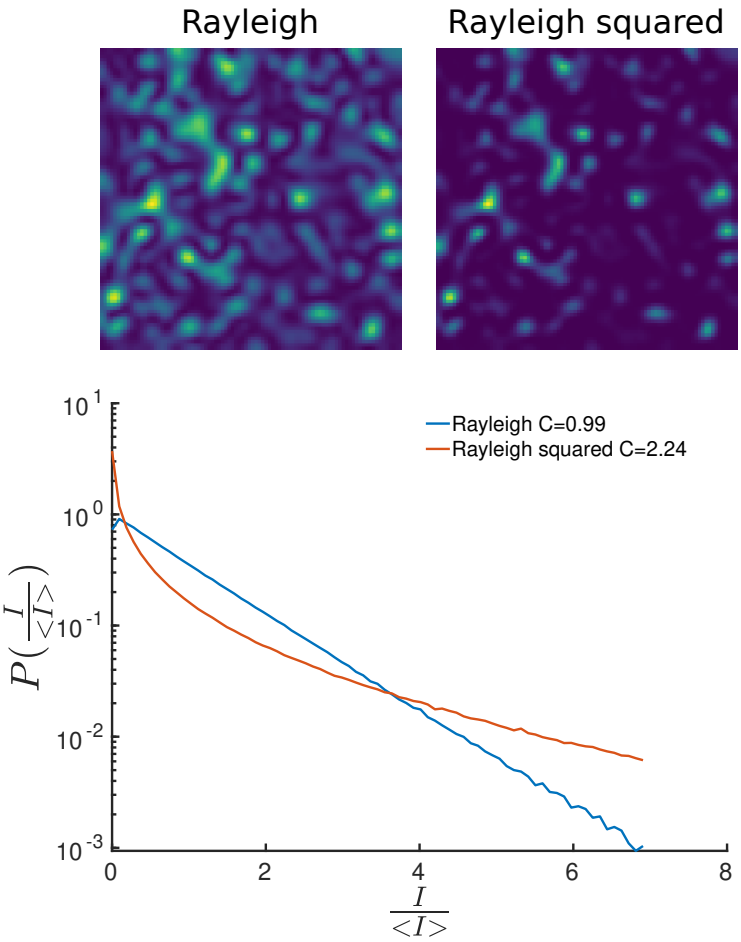

Figure 4.2: **Rayleigh and squarred Rayleigh speckle patterns and related intensity distribution.** On the top left, example of a standard Rayleigh speckle pattern. On the top right, example of a standard Rayleigh speckle pattern from above squared. On the bottom, probability density function averaged over 200 simulations. In blue, PDF of standard Rayleigh patterns. In orange, PDF of the same Rayleigh patterns but squared. C stands for contrast.

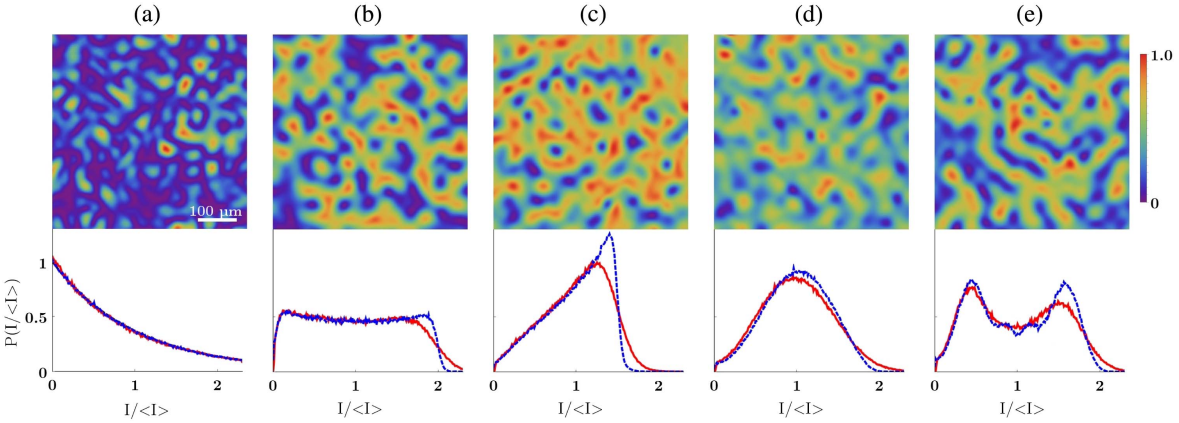

Figure 4.3: **Arbitrary shapes of speckle intensity distribution.** (a) Rayleigh speckle pattern and (b-e) customized speckle patterns with distinct intensity statistics. In the top row, each pattern has a size of 504 μm by 504 μm, and the maximum intensity is normalized to 1. The associated PDF, shown in the lower row, is (b) uniform, (c) increasing linearly, (d) peaked at a non-zero intensity, and (e) bimodal, within a predefined range of intensity. The red solid curves are experimental data, whereas the blue dashed curves are from numerically generated target speckle patterns. Both are a result of spatial and ensemble averaging over 50 independent speckle patterns. Figure from [108].

4.1.1 Algorithm

To change the speckle distribution into the desired plane, one needs to engineer the phase of the incoming wavefront, for example with a SLM. To find out what phase is required, the algorithm used here is composed of two steps to produce an arbitrary speckle pattern (Derivated from Cao et al. [108]):

Phase 1: find the nonlinear local transformation

The idea here is to generate a set of pattern with the desired speckle intensity distribution. The algorithm starts with a regular Rayleigh speckle pattern which can be described by a random phase pattern on a SLM at the Fourier plane of a lens. First, one needs to find the transformation function f that modifies the original speckle pattern intensity I locally to go from a Rayleigh PDF $P(I)$ to the speckle intensity $\tilde{I}$ with targeted PDF $F(\tilde{I})$. We are searching for f such that $\tilde{I} = f(I)$ and $P(I)dI = F(\tilde{I})d\tilde{I}$ which can be re written $\int_0^I e^{-I'}dI' = \int_{\tilde{I}_{min}}^{\tilde{I}} F(\tilde{I}')d\tilde{I}'$. Once f is found, one is able to generate the targeted intensity distribution from any Rayleigh speckle pattern. Then, to obtain a stack of non-Rayleigh PDFs, one need to feed the algorithm with a stack of Rayleigh PDF.

Phase 2: find the SLM phase pattern
The idea here is to find a set of phase mask that can generate the speckle with the desired intensity distribution. We have a set of non Rayleigh PDF speckle patterns and we want to generate them experimentally. To do so, one measures the transmission matrix between the SLM plane and the image plane which enables to map the field on the SLM to the field on the camera. The camera has to respect the Nyquist limit so that the speckle pattern is well sampled for this part to work. Numerically and with a Gerchberg-Saxton approach [109], we compute the difference between the targeted speckle pattern (image created in phase 1) and the resulting speckle of the SLM phase multiplication by the transmission matrix.

Sometimes the procedure does not converge the desired speckle pattern and the intensity distribution stays Rayleigh. In that case, we will not take that image into account. For example in Fig.4.5, we wanted to create 200 tailored speckle distribution images but we use only 183 of them. Indeed, 17 images were either Rayleigh distributions or had only one very intense speckle spot which was not realistic of a speckle. Finally, we obtain a set of non-Rayleigh PDF and a set of phase masks to experimentally generate those PDFs.

We will now explore how to design the function to transform a Rayleigh PDF image into the desired PDF.

4.1.2 Design of a sub-Rayleigh speckle pattern

In the case of a nonlinear signal of second order like 2PF or the Pump in a CARS process, the speckle becomes more sparse. To counter balance the induced sparsity by the nonlinearity, we want to illuminate the sample with a so called sub-Rayleigh PDF which means that there are fewer bright spots than a regular Rayleigh PDF. To that end, we decided to design speckle patterns that satisfy a $e^{-\frac{1}{2}\frac{I}{<I>}}$ PDF. In the following we will derive how to perform such a transformation on a random set of Rayleigh speckles.

$$\begin{aligned} PDF_{Rayleigh} &= \int_0^I e^{-I'} dI' = \beta \int_0^{\tilde{I}'} e^{-\frac{1}{2}\tilde{I}'} d\tilde{I}' \\ \implies \tilde{I} &= -\frac{2}{\beta} \ln\left(1 - \frac{PDF_{Rayleigh}}{2}\right) \end{aligned} \tag{4.2}$$

where $< I >= 1$ and β a normalization constant which is computed as follows:

$$\begin{aligned} < I > &= < \tilde{I} > \\ \implies < \tilde{I} > &= \beta \int_0^{I_{max}} \tilde{I}' e^{-\frac{1}{2}\tilde{I}'} d\tilde{I}' \\ \implies \beta &= 4 \left(1 - e^{-\frac{1}{2}\tilde{I}_{max}} \left(1 + \frac{\tilde{I}_{max}}{2} \right) \right) \end{aligned} \tag{4.3}$$

where I_{max} is the maximum intensity of the speckle.

In Fig.4.4, from initially Rayleigh PDF speckle pattern stack we compute a sub-Rayleigh speckle pattern stack of images and one image of each is depicted in the top row. The average contrast over the whole stack of Rayleigh pattern is $C = 1$ as expected and the sub-Rayleigh distribution reaches $C = 0.76 < 1$. Then, both stack of images are squared and normalized so that the energy in each image is conserved. We can notice the sub-Rayleigh pattern seems more homogeneously illuminated and it is corroborated in Fig.4.4 (top). In Fig.4.4 (bottom), we plotted the average PDFs of the different types of speckle statistics. We can notice that the sub-Rayleigh squared curve (purple) crosses the standard Rayleigh curve (orange) before the standard Rayleigh squared curve (yellow). However, sub-Rayleigh squared speckle pattern has a contrast above 1 which is above what was targeted by designing the transformation function. Indeed, the squared sub-Rayleigh PDF should have match the standard Rayleigh PDF. It can be explained by the speckle grain size reduction brought by squaring the speckle. Indeed, when we compute the sub-Rayleigh PDF from a Rayleigh pattern, the algorithm changes the PDF but keeps the speckle grain size the same. Thus the squaring effect on the size of the speckle grain is not taken into account while we attempt to counter balance the squaring effect on the PDF. The transformation was designed to match a Rayleigh PDF after squaring and for the same reason as above mentioned it is altered from the Rayleigh PDF.

In conclusion, we will compare a Rayleigh pattern (A), a sub-Rayleigh pattern (B), a squared Rayleigh pattern (C) and a squared sub-Rayleigh pattern (D) and we will study numerically what would be the consequences of such PDFs on the blind-SIM reconstructed image.

4.2 Usage of speckle tailoring in BSIM

We consider 4 stacks of images with different speckle PDFs and we will use them to simulate what would be the consequences of such intensity distributions on a blind-SIM reconstruction. As a forward model for CARS, we will use a 3PF equivalent to simplify:

$$M_l = \left(\rho \cdot \left(I_l^{illumination} \right)^2 \right) \circledast h_{detection} \tag{4.4}$$

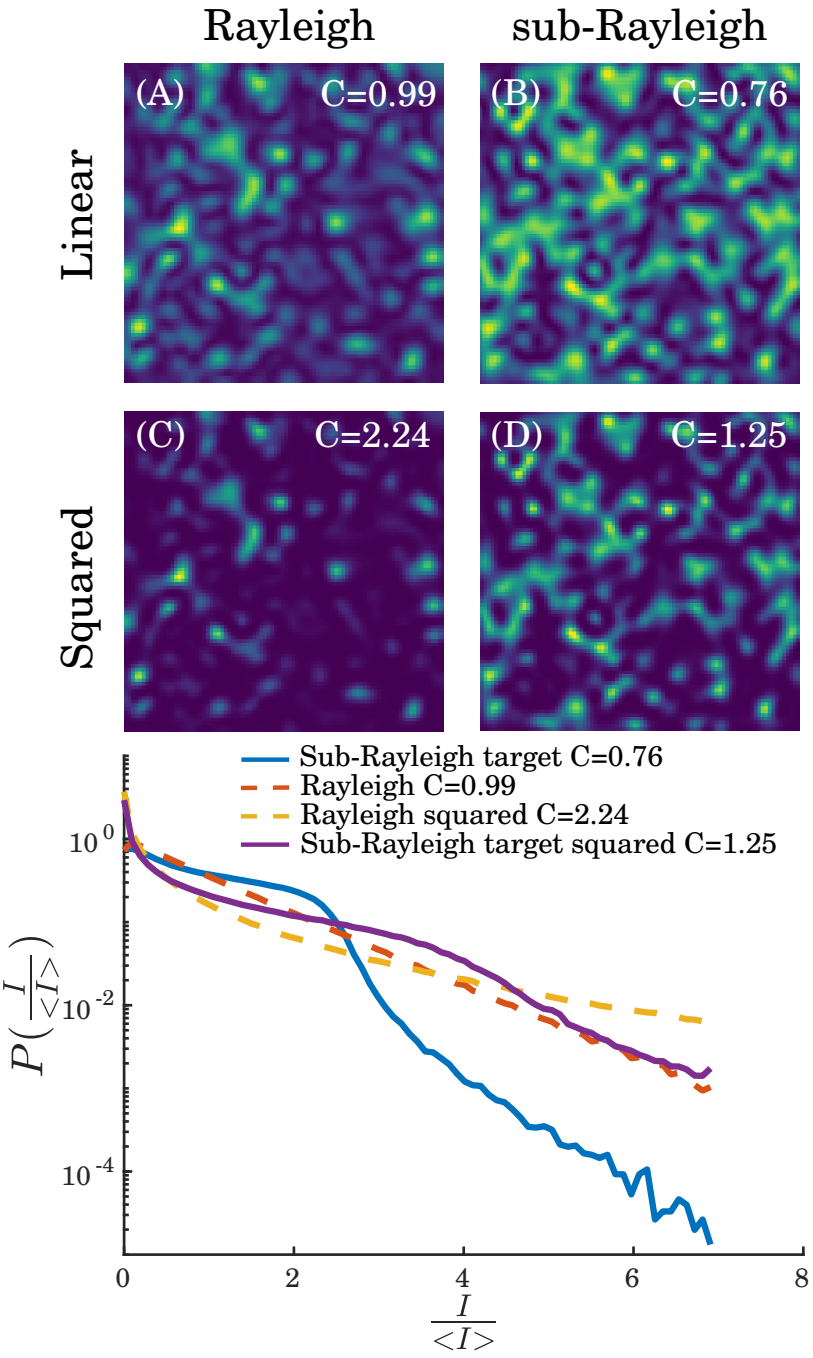

Figure 4.4: **Arbitrary shapes of speckle intensity distribution.** (a) Rayleigh speckle pattern and (b-e) customized speckle patterns with distinct intensity statistics. In the top row, each pattern has a size of 504 μm by 504 μm, and the maximum intensity is normalized to 1. The associated PDF, shown in the lower row, is (b) uniform, (c) increasing linearly,

where M_l is one image, ρ the density of fluorophores for example, $I_l^{illumination}$ a speckle pattern and $h_{detection}$ the PSF of the system detection in our case the Stokes beam.

To simulate experimental images, we use equation (4.4) for CARS and $\left(I_l^{illumination}\right)^2$ corresponds to the stack of illumination from set (C) or (D) from Fig.4.4. Similarly, we simulate 2PF equivalents by using the equation (3.3) used in chapter 3 where $I_l^{illumination}$ corresponds to stack (A) and (B). These 2PF equivalents could be 2PF, SHG or SRS, neglecting coherent effect of the PSFs. In the same way as in chapter 3, we use the Siemens star as the unknown object to reconstruct ρ. For both 2PF and 3PF equivalents, the PSF for detection is the same $h_{detection}$ since in CARS the dependency on the Stokes intensity is linear. We then feed the simulated images to our standard blind-SIM algorithm with exactly the same parameters for each reconstruction and we will study the final results as well as intermediary reconstruction of the object for the different PDFs. We can see the results in Fig.4.5., where each column represent a different PDF type going from sub-Rayleigh (2PF equivalent), Rayleigh (2PF equivalent), sub-Rayleigh squared (3PF equivalent) and Rayleigh squared (3PF equivalent). Each row corresponds to a different number of speckle realizations from the given stack that is used to reconstruct the Siemens star. Note that we keep the speckle in the same order which means that for the first row, each 5 speckle patterns for the 4 different PDFs used are coming from the same initial Rayleigh pattern. In fact, when transforming a Rayleigh PDF pattern into a sub-Rayleigh pattern or a squared pattern, the images still share similar spatial features since the transformations are local. This way, the spatial pattern are somehow similar and it enables us to compare reconstruction with very few images without too much spatial feature discrepancies.

We can observe that the fastest PDF to give satisfying results is the sub-Rayleigh PDF and the final reconstruction looks much better than the standard Rayleigh PDF case. Indeed, with only 35 images the Siemens star reconstruction starts to look decent while all the other PDFs are still not convincing with the Rayleigh squared far behind. For the final reconstruction with 183 images, we see that the squared Rayleigh is still far from the Siemens star object. This result confirms that for CARS, it is either needed to acquire a lot more images or to tailor the PDF. However, the resolution limit for each case is very similar while we should see an improvement for the squared patterns whereas we can see that the speckle grains in Fig.4.4. are smaller as it is expected. While the results are encouraging showing that tailoring can indeed help to speed up the acquisition by 2-3-fold, there is clearly further work needed to understand why the resolution has not been improved.

Now, we will compute the correlation of the reconstructed image with the ground truth Siemens star image to have quantitative value of how good the reconstruction is. The results are depicted in Fig.4.6. We compute the correlation for different number of images in each reconstruction and plot the results for the different PDFs. The vertical

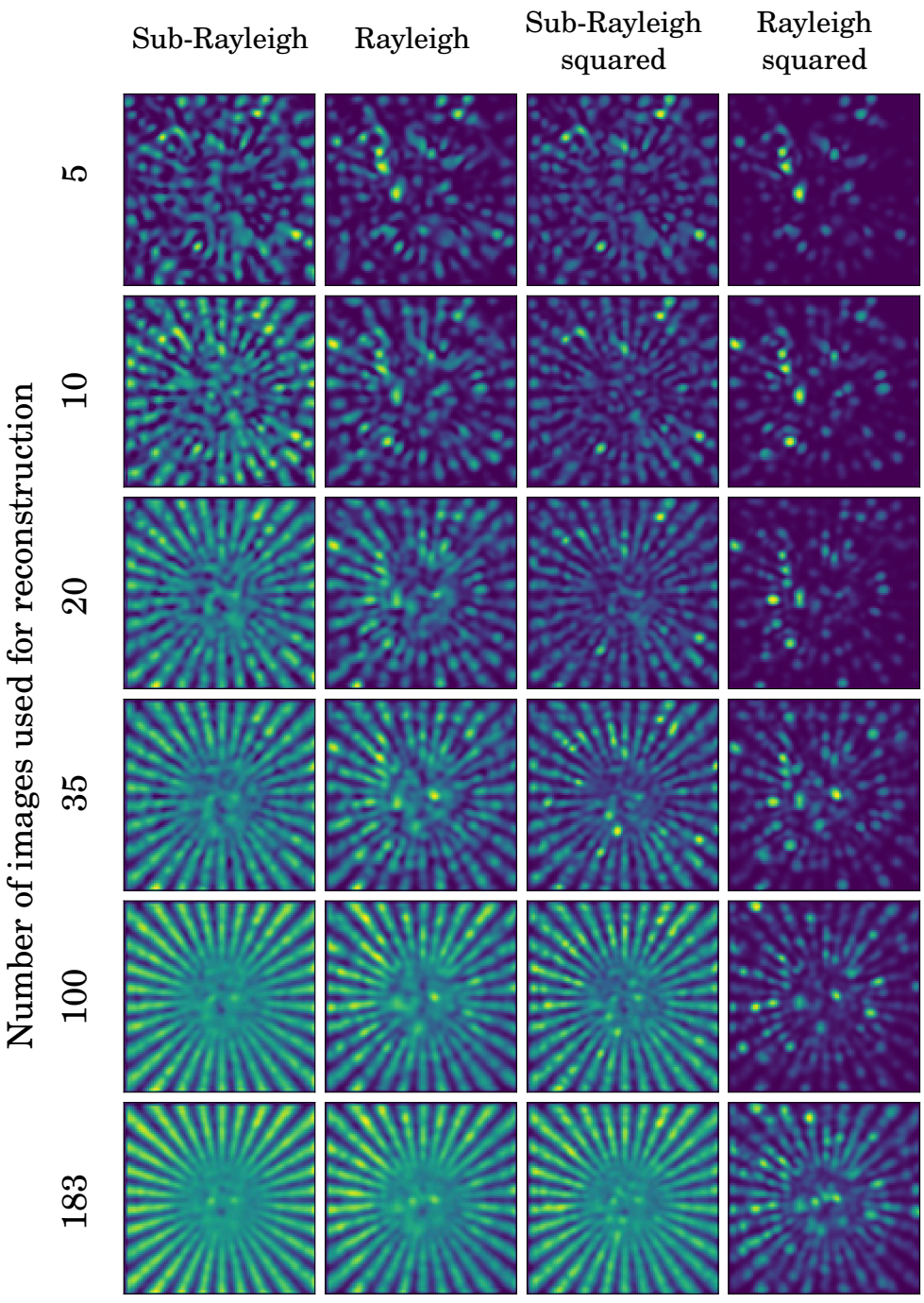

Figure 4.5: **Evolution of the Siemens star reconstruction depending on the number of images.** Siemens star reconstruction using blind-SIM algorithm. Each column correspond to a different speckle PDF among Sub-Rayleigh, Rayleigh, Sub-Rayleigh squared and Rayleigh squared which are shown in Fig.4.4. Each row correspond to a different number of images used in the blind-SIM algorithm to reconstruct the Siemens star.

black lines represent the number of images used for the reconstruction in Fig.4.5. We can see that each PDF converges toward an upper limit where the correlation saturates. As it was visible in Fig.4.5, the standard CARS equivalent is far behind the reconstruction quality of the three others. The sub-Rayleigh PDF has the highest correlation upper limit and it is then the best reconstruction result and it is able to reach this saturation value with as few as 50 images while 80, 120 images are needed for sub-Rayleigh squared and Rayleigh respectively. In other words, the value of the contrast does not seem to be the most relevant criteria.

However, one can notice that both the sub-Rayleigh and sub-Rayleigh squared PDFs have a small bump at $2\frac{I}{\langle I\rangle}$ and $4\frac{I}{\langle I\rangle}$ compared to the Rayleigh PDF. It seems that it is more beneficial to have more speckle grains with a moderate intensity than lower number with high intensity. One could imagine a speckle distribution like in Fig.4.3.d. with different peak values to find out what is the best ratio $\frac{I}{\langle I\rangle}$ or to combine several of them like in the distribution in Fig.4.3.e. This result can bring the question what is the optimal speckle PDF for blind-SIM methods ? We will not address this question in the manuscript but it is an interesting topic. In ghost imaging, Kuplicki et al. [110] showed that higher-order correlations are beneficial. Indeed, standard Rayleigh PDF have second order correlation but they do not have higher order correlation while it is exactly why tailored PDF are fully developed and diffraction limited grain size. That being said, for the same order of correlation they find that sub-Rayleigh PDFs produce the highest resolution compared to Rayleigh and super-Rayleigh PDFs.

To conclude, we showed that a speckle PDF that differs from the standard Rayleigh can enhanced the reconstruction by lowering the number of required images like sub-Rayleigh pattern designed here but it can also worsen the reconstruction like the Rayleigh squared.

4.3 Resilience of speckle tailoring to scattering

We demonstrated that it was beneficial to tailor the speckle PDF. However, in blind-SIM we do not want to control and know what kind of pattern is reaching the sample. In the process of designing a non-Rayleigh speckle pattern, we start with a known Rayleigh speckle to change its statistics and obtain a known image of a non-Rayleigh PDF. Now if we sent this tailored speckles into an unknown weakly scattering media, what happens to the speckle statistics ? How much does the non-Rayleigh statistics of a speckle hold in a scattering medium? We will start to answer this question in this section by propagating numerically the phase mask giving non-Rayleigh PDFs through a scattering medium.

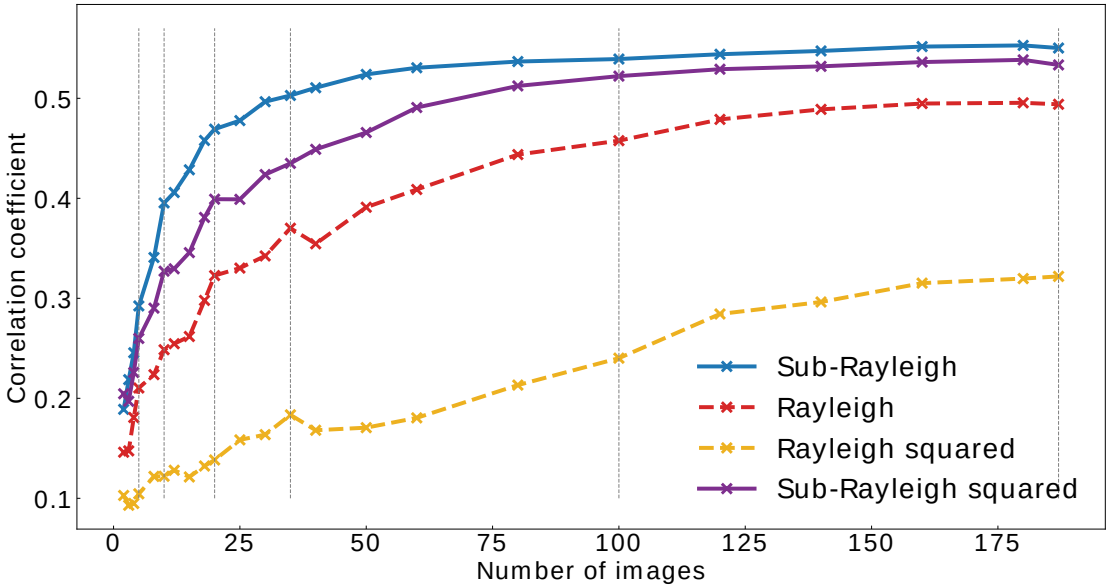

Figure 4.6: **Correlation between ground truth object and the reconstructed image using different number of images.** Each color represents a different speckle PDF among Sub-Rayleigh (blue), Rayleigh (dashed red), Rayleigh squared (dashed yellow) and Sub-Rayleigh squared (purple) which are shown in Fig.4.4. Dashed vertical gray lines represent the number of image used for reconstructed images which are shown in Fig.4.5

4.3.1 Propagation method

To simulate the propagation in a scattering media, we use the beam propagation method algorithm (BPM) developed by Cheng et al. [111]. The scattering medium is modeled as a series of parallel planar layers of phase masks and at each plane location a spatially varying random phase $e^{i\Phi(x,y)}$ is applied (see Fig.4.7). In between layers, the wave propagates freely without any inhomogeneities. To propagate the field, the angular spectrum method is used and consists in taking the Fourier transform of the field, multiply it with a propagator P and Fourier transform it back.

$$P = e^{i\Psi} = e^{in\sqrt{k^2-k_x^2-k_y^2}d}e^{i\Phi} \tag{4.5}$$

where d is the distance between neighboring phase masks, n is the refractive index, λ is the wavelength, $k = \frac{2\pi}{\lambda}$ is the wave number, and k_x , k_y are its x, y transverse components, respectively.

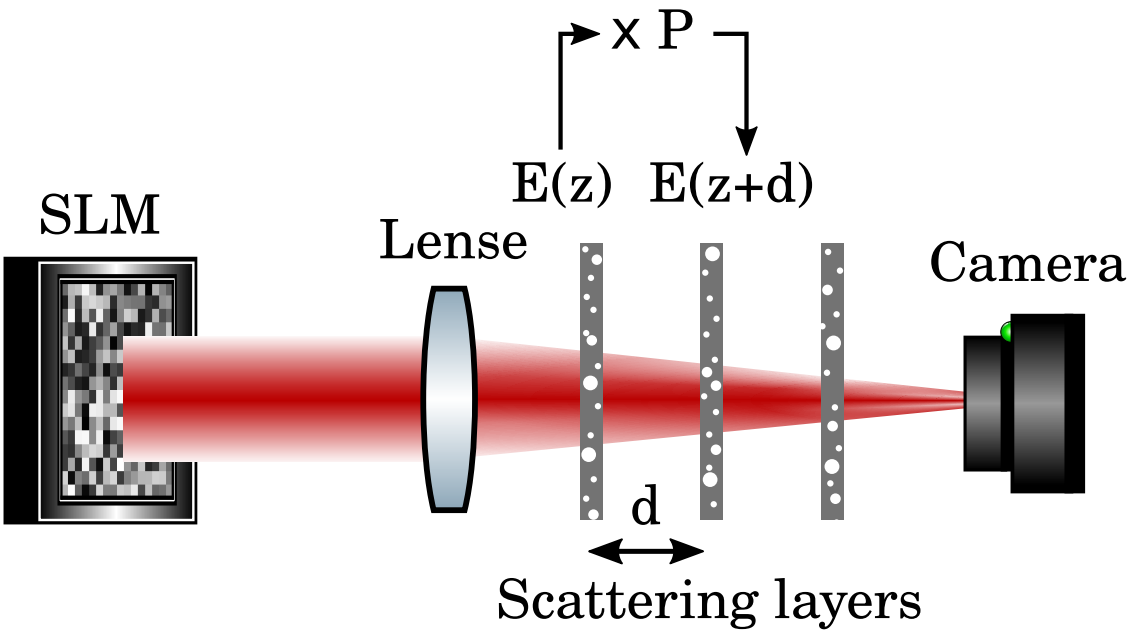

Figure 4.7: **Propagation of the field using angular spectrum method.**

4.3.2 Non-Rayleigh speckle statistics after propagation in a scattering medium

Here we took a SLM phase mask stack that corresponds to a sub-rayleigh PDF and propagated it. When a non-Rayleigh PDF phase mask gets scrambled, it converges back to a standard Rayleigh PDF. For this reason, we decided to characterize the non-Rayleigh PDF properties of the speckle by measuring the contrast of the given pattern for different optical thicknesses of the medium. The results are plotted in Fig.4.8. When there is no scattering, the mean contrast of the stack of non-Rayleigh PDFs is around 0.64. We progressively increased the scattering of the medium where the non-Rayleigh speckles were propagating. We can observe that there is a continous increase in the constrat which is a proxy for the loss of non Rayleigh PDF. More precisely, the speckle keeps a sub-Rayleigh PDF until $L/l_S \approx 0.6$ and then converges back to a contrast close to 1 around a ratio $L/l_S \approx 1.4$ which corresponds to a Rayleigh PDF. This means that it is possible to use the speckle tailoring method only for rather small optical thicknesses compared to 1. Assuming a 200 μm mean free path [6], it would correspond to 120 μm deep which is already very deep for super resolution technique without any active correction.

If the imaging technique is operated at low optical thicknesses, we have seen that the non-Rayleigh PDF still holds without characterizing the medium. In these conditions, there is yet another interesting feature of the non-Rayleigh PDF. Indeed, the intensity

distribution is tailored for one targeted plane but the speckle statistics reverts back to Rayleigh PDF after one Rayleigh range propagation z_R as can be seen in Fig.4.9. We can observe that the contrast is quickly rising as soon as we move from the targeted depth and it reverts back to ≈ 1 after $\approx 2z_R$. Since in the super resolution algorithm we retrieve the illuminating speckle, in principle we could add a condition on the retrieved speckle PDF. It would result in a reconstruction which would favor some type a speckle PDF and thus ignoring Rayleigh pattern feature from above and below the focus. In addition, Rayleigh pattern out of the focus would not be properly reconstructed since they require more images to properly reconstruct an object. Therefore, it could computationally reject signals coming from lower and upper layers from the focus resulting in the better sectioning.

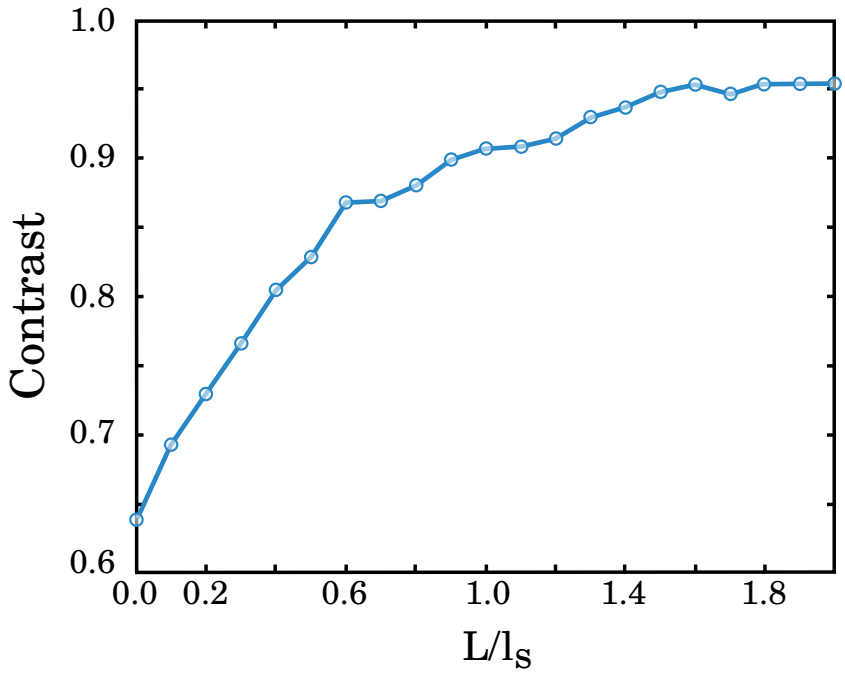

Figure 4.8: **Evolution of the contrast of a non-Rayleigh PDF with optical thickness.**

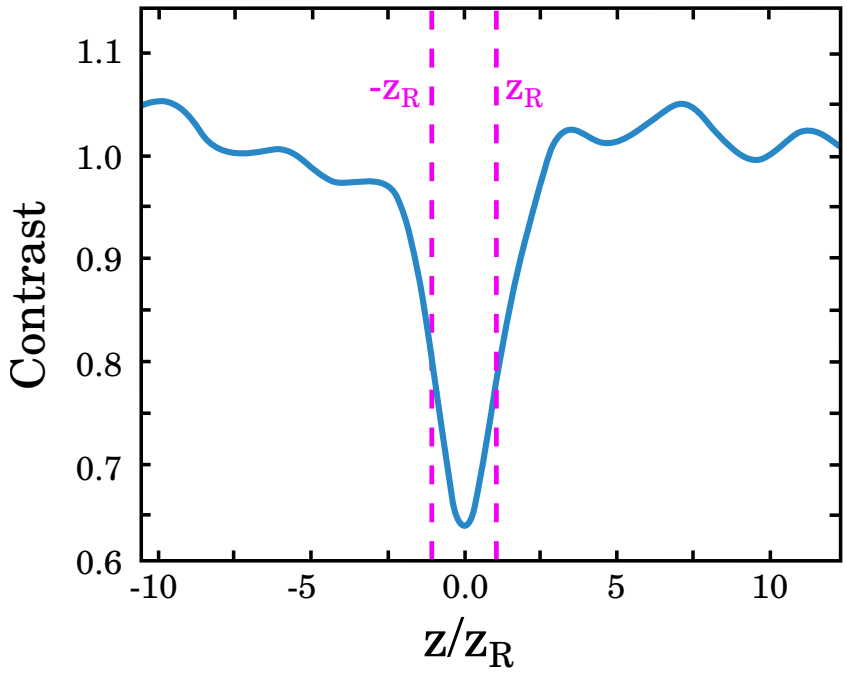

Figure 4.9: **Evolution of the contrast of a non-Rayleigh PDF along the optical axis with no scattering.**

In this chapter, the objective was to start to think about the difficulties for CARS compatibility with the blind-S^3 methodology and more precisely we looked at the increasing sparsity of the speckle pattern. To tackle this issue, we modified the intensity distribution from a Rayleigh to non-Rayleigh PDF and studied the effect it could have on the number of images required to reconstruct a final image and the implications it could have on the image quality. We showed that a sub-Rayleigh PDF, or more precisely a PDF which has more average intensity speckle grain can greatly reduces the number of image required to reconstruct the final image. Finally, the modified speckle PDF can hold some scattering from an unknown medium ($L/L_s \approx 0.6$) but it reverts back to a Rayleigh speckle when the medium is optically too thick. Nevertheless, these depths are extremely deep for super resolution imaging without active corrections and thus speckle tailoring could be useful at reducing the number of speckle realizations required for blind-SIM even in scattering biological tissues.

Chapter 5

Conclusion and perspectives

During this PhD, we investigated how to achieve super resolution imaging of biological tissues in a label-free manner keeping chemical selectivity and the possibility to realize spectroscopy measurement.

To begin with, we introduced fluorescence imaging which is currently the main imaging modality for biological tissues. We highlighted the central role that fluorescence labels has and described some of its main downsides:

- It alters the natural behavior of biological specimens and can be toxic for biological tissues.
- The fluorescence labels fade away because of quenching or photobleaching.
- It is cumbersome to develop a new label for new biological applications and it is tedious to label biological tissues.
- The emission spectrum is broad and hinders spectral multiplexing imaging.

Hence, we investigated optical signal from other natures and described the Raman scattering different contrast mechanisms based on Raman scattering. First, spontaneous Raman with which it is possible to obtain a full Raman spectrum but its cross section is very weak so that it does not seem compatible with fast imaging. Then, we featured the mechanism of coherent Raman scattering which is significantly more efficient than its spontaneous counterpart. Following this, we investigated what could be the super resolution method that could be the most compatible with biological imaging using coherent Raman.

The next step was to choose the super resolution mechanism. We investigated localization method but since they require blinking label and no label-free mechanism has this blinking feature thus far, we discarded it. Then, we investigated STED-like approach and even though it was possible to image without labels, the energy needed to obtain a resolution improvement with high NA objective would not be compatible with

biological imaging. Finally, we explored SIM-like method and highlighted the independence of the resolution gain with incoming intensity and its easy implementation. After reviewing these different methods we decided to choose SIM-like method because it is the most compatible with biological tissue imaging even though the gain in resolution is not as high as with other method on the paper. Moreover, blind-SIM methodology was a plus because it would resolve the problem of the scattering naturally arising from biological tissues.

Consequently, we designed a setup to demonstrate the feasibility of a coherent Raman super resolution microscope. Indeed, coherent Raman and SIM are not compatible straightforwardly since SIM is a wide-field imaging approach while coherent Raman requires point scanning for energy but also detection purposes. To match both methods, we designed a new scanning scheme which enables to combine coherent Raman scattering imaging and blind-SIM while still remaining compatible with standard reconstruction algorithm. Moreover, to evaluate resulting images we needed to compare them to the conventional coherent Raman counterpart. Thus, we built a multi-modal microscope where it is easy to swap between different configurations. To summarize, there are two main beam paths corresponding to the conventional coherent Raman scattering scheme and to the blind-S^3 scheme where it is possible to spectrally filter both the Pump or the Stokes beam.

Following this, we move to the experimental side. We experimentally demonstrated that the blind-S^3 methodology is able to reach super resolution using plastic samples. These samples were calibrated polystyrene beads of 239nm diameter that we excited at the C-H stretch Raman resonance corresponding to 2903 cm^{-1}. The conventional stimulated Raman scattering counterpart was not able to resolve the beads while the blind-S^3 did and we retrieved the correct beam diameter for the beads making sure the reconstruction underwent a correct procedure. To further study the capabilities of the method, we scanned a thin film of oil along the optical axis and showed that the blind-S^3 is able to reject signal when the sample is out of the focus thus demonstrating a sectioning feature. Then, we decided to image thin biological samples, namely HeLa cells, and we managed to improve the resolution compared to the conventional SRS and confirm that the methodology was compatible with biological imaging. Finally, we imaged much thicker biological sample, namely mouse cerebellum, and went as deep as $\approx 8\mu$m with scattering and Raman resonant media below and above the focus. We imaged in the C-H spectral region and could disentangled two myelin rings by using our super resolution method. It further confirmed that the technique is compatible with biological tissues but also highlighted the sectioning abilities of the method.

After combining SRS and blind-SIM, we wanted to study how to go further in resolution improvement. We reached the conclusion that going for high nonlinearity orders in intensity was relevant and decided to study what would be the difficulties to implement CARS blind-SIM. There are several issues we can think of, for instance the non

resonant background which was not addressed here but one could look at the following paper from Ganikhanov [112] or quantitative imaging issue [113]. In this manuscript, we decided to first study the effect of the nonlinearity on the speckle sparsity and the effect on the number of images required to obtain a satisfying reconstruction. We showed that by using a sub-Rayleigh PDF we could greatly reduce the number of images needed to reconstruct a object compared to Rayleigh PDF. We then showed that a squared sub-Rayleigh PDF corresponding to a CARS equivalent case would need fewer images and reach a better correlation to the initial object than the Rayleigh PDF with lower nonlinearity order while the squared Rayleigh PDF had higher number of images and lower correlation. Finally, we studied how we could keep the blind feature from blind-SIM while changing the speckle intensity distribution. To that end, we numerically propagated non-Rayleigh phase masks into several optical thickness medium. We showed that the speckle PDF could hold the non-Rayleigh PDF until $\approx 0.6\ L/l_S$ and then rapidly reverted back to a Rayleigh PDF. This means that for optically thin medium, it is possible to combine speckle PDF tailoring and blind-SIM.

In further work, it would be interesting to study more in depth the effect of speckle PDFs on blind-SIM algorithm. We think that there are more optimal solutions than the one we used and probably there are some different solutions if one wants to reduce the number of image needed or the contrast of the reconstructed image. In addition, it is important to test these results experimentally since the numerical simulations were done without noise and also to make sure that it does no result in a large increase in the power needed to obtain satisfying SNR.

Then, it would be interesting to start exploring deep imaging with the blind-S^3 methodology to study how far the resolution gain can sustain. It was not possible with the laser source we had in the lab, but with the new laser now available it becomes possible. The 2MHz laser source will have much higher pulse energy than the current 80MHz while being nowhere near the low repetition rate laser used in STED-like imaging ($\sim 1\ kHz$ or lower). Coupling this new laser source with spectral focusing would increase the available power by a factor ~ 50 which enables deep imaging in scattering sample. In addition, blind-S^3 could benefit from temporal focusing to have two sources of sectioning capabilities, one coming from the nonlinearity and the other from temporal focusing. This additional source of sectioning will be usefull to keep sectioning capabilities while extending the FOV for blind-S^3 by releasing nonlinear sectioning (trade-off mentioned in Chapter 3).

Finally, we did not explore the spectroscopy capabilities of the current setup during this PhD. It is a very important feature from Raman scattering and could be used at its advantage for super resolution measurement. Indeed, it is possible to acquire several images for the same speckle realization at different Raman resonances and then change

the realization and repeat. This way, the stack of images has 2 dimensions and one could develop a new blind-SIM algorithm taking into account the different chemical natures of species under illumination. By adding this feature, the reconstruction algorithm would not only take spatial information but also spectral information to reconstruct the final super resolution image. In addition, in case of using non-Rayleigh PDF, the speckle statistics could be introduced in the reconstruction algorithm as well in an attempt to improve the rejection of the signal coming from outside the focus area.

To conclude, we have shown a chemically selective label-free super resolution method that is compatible with biological tissues imaging. By using coherent Raman scattering, we pave the way for fast label-free super resolution imaging that could empower biologist communities to work more with label-free technique which we hope will lead to great discoveries.

Bibliography

[1] Albert Van Helden, Sven Dupré, and Rob van Gent. *The origins of the telescope*, volume 12. Amsterdam University Press, 2010.

[2] Robert Hooke. *Micrographia : or, Some physiological descriptions of minute bodies made by magnifying glasses.* 1665.

[3] Osamu Shimomura, Frank H Johnson, and Yo Saiga. Extraction, purification and properties of aequorin, a bioluminescent protein from the luminous hydromedusan, aequorea. *Journal of cellular and comparative physiology*, 59(3):223–239, 1962.

[4] Douglas C Prasher, Virginia K Eckenrode, William W Ward, Frank G Prendergast, and Milton J Cormier. Primary structure of the aequorea victoria green-fluorescent protein. *Gene*, 111(2):229–233, 1992.

[5] Martin Chalfie, Yuan Tu, Ghia Euskirchen, William W Ward, and Douglas C Prasher. Green fluorescent protein as a marker for gene expression. *Science*, 263 (5148):802–805, 1994.

[6] Nicholas G. Horton, Ke Wang, Demirhan Kobat, Catharine G. Clark, Frank W. Wise, Chris B. Schaffer, and Chris Xu. In vivo three-photon microscopy of subcortical structures within an intact mouse brain. 7(3):205–209. ISSN 1749-4885, 1749-4893. doi: 10.1038/nphoton.2012.336. URL `http://www.nature.com/articles/nphoton.2012.336`.

[7] Jean Livet, Tamily A. Weissman, Hyuno Kang, Ryan W. Draft, Ju Lu, Robyn A. Bennis, Joshua R. Sanes, and Jeff W. Lichtman. Transgenic strategies for combinatorial expression of fluorescent proteins in the nervous system. 450 (7166):56–62. ISSN 0028-0836, 1476-4687. doi: 10.1038/nature06293. URL `http://www.nature.com/articles/nature06293`.

[8] Demirhan Kobat, Nicholas G. Horton, and Chris Xu. In vivo two-photon microscopy to 1.6-mm depth in mouse cortex. 16(10):106014. ISSN 10833668. doi: 10.1117/1.3646209. URL `http://biomedicaloptics.spiedigitallibrary.org/article.aspx?doi=10.1117/1.3646209`.

[9] Qianru Yu and Ahmed A Heikal. Two-photon autofluorescence dynamics imaging reveals sensitivity of intracellular nadh concentration and conformation to cell physiology at the single-cell level. *Journal of Photochemistry and Photobiology B: Biology*, 95(1):46–57, 2009.

[10] Dong Li, Wei Zheng, and Jianan Y Qu. Two-photon autofluorescence microscopy of multicolor excitation. *Optics letters*, 34(2):202–204, 2009.

[11] V Nucciotti, C Stringari, L Sacconi, F Vanzi, L Fusi, M Linari, G Piazzesi, V Lombardi, and FS Pavone. Probing myosin structural conformation in vivo by second-harmonic generation microscopy. *Proceedings of the National Academy of Sciences*, 107(17):7763–7768, 2010.

[12] Xiyi Chen, Oleg Nadiarynkh, Sergey Plotnikov, and Paul J Campagnola. Second harmonic generation microscopy for quantitative analysis of collagen fibrillar structure. *Nature protocols*, 7(4):654–669, 2012.

[13] Jeff A Squier, Michiel Müller, GJ Brakenhoff, and Kent R Wilson. Third harmonic generation microscopy. *Optics express*, 3(9):315–324, 1998.

[14] Bettina Weigelin, Gert-Jan Bakker, and Peter Friedl. Third harmonic generation microscopy of cells and tissue organization. *Journal of Cell Science*, 129(2): 245–255, 2016.

[15] F Zernike. The phase contrast process in microscopic examinations. *Physikalische Zeitschrift*, 36:848–851, 1935.

[16] Gregory W Auner, S Kiran Koya, Changhe Huang, Brandy Broadbent, Micaela Trexler, Zachary Auner, Angela Elias, Katlyn Curtin Mehne, and Michelle A Brusatori. Applications of raman spectroscopy in cancer diagnosis. *Cancer and Metastasis Reviews*, 37(4):691–717, 2018.

[17] Kevin M Dean and Amy E Palmer. Advances in fluorescence labeling strategies for dynamic cellular imaging. *Nature chemical biology*, 10(7):512–523, 2014.

[18] Nikki Kuhar, Sanchita Sil, Taru Verma, and Siva Umapathy. Challenges in application of raman spectroscopy to biology and materials. *RSC advances*, 8 (46):25888–25908, 2018.

[19] Lu Wei, Zhixing Chen, Lixue Shi, Rong Long, Andrew V Anzalone, Luyuan Zhang, Fanghao Hu, Rafael Yuste, Virginia W Cornish, and Wei Min. Super-multiplex vibrational imaging. *Nature*, 544(7651):465–470, 2017.

[20] Ji-Xin Cheng and X Sunney Xie. Vibrational spectroscopic imaging of living systems: An emerging platform for biology and medicine. page 11.

[21] Fa-Ke Lu, Srinjan Basu, Vivien Igras, Mai P. Hoang, Minbiao Ji, Dan Fu, Gary R. Holtom, Victor A. Neel, Christian W. Freudiger, David E. Fisher, and X. Sunney Xie. Label-free DNA imaging in vivo with stimulated raman scattering microscopy. 112(37):11624–11629. ISSN 0027-8424, 1091-6490. doi: 10.1073/pnas.1515121112. URL http://www.pnas.org/lookup/doi/10.1073/pnas.1515121112.

[22] Rajinder Singh. C. v. raman and the discovery of the raman effect. 4:22.

[23] Hervé Rigneault and Pascal Berto. Tutorial: Coherent raman light matter interaction processes. 3(9):091101. ISSN 2378-0967. doi: 10.1063/1.5030335. URL http://aip.scitation.org/doi/10.1063/1.5030335.

[24] Robert W Boyd. *Nonlinear optics*. Academic press, 2020.

[25] Martin J. Klein. The first phase of the bohr-einstein dialogue. *Historical Studies in the Physical Sciences 2*, 2:pp. 218–219. ISSN 0073-2672. doi: 10.2307/27757302. URL https://online.ucpress.edu/hsns/article/doi/10.2307/27757302/47768/The-First-Phase-of-the-BohrEinstein-Dialogue.

[26] Adlof Smekal. Zur quantentheorie der dispersion. *Naturwissenschaften*. URL https://link.springer.com/article/10.1007%2FBF01576902.

[27] Arthur H. Compton. A quantum theory of the scattering of x-rays by light elements. 21(5):483–502. doi: 10.1103/PhysRev.21.483. URL https://link.aps.org/doi/10.1103/PhysRev.21.483. Publisher: American Physical Society.

[28] R. H. Stuewer. *The Compton effect. Turning points in physics.* 1975.

[29] C. V. Raman. A new radiation. *Indian Journal Physics*, 2:387–398, 1928.

[30] Lars Kastrup and Stefan W. Hell. Absolute optical cross section of individual fluorescent molecules. 43(48):6646–6649. ISSN 1521-3773. doi: 10.1002/anie.200461337. URL https://onlinelibrary.wiley.com/doi/abs/10.1002/anie.200461337. _eprint: https://onlinelibrary.wiley.com/doi/pdf/10.1002/anie.200461337.

[31] Gisela Eckhardt, R. W. Hellwarth, F. J. McClung, S. E. Schwarz, D. Weiner, and E. J. Woodbury. Stimulated raman scattering from organic liquids. 9(11):455–457. ISSN 0031-9007. doi: 10.1103/PhysRevLett.9.455. URL https://link.aps.org/doi/10.1103/PhysRevLett.9.455.

[32] E. Ploetz, S. Laimgruber, S. Berner, W. Zinth, and P. Gilch. Femtosecond stimulated raman microscopy. 87(3):389–393. ISSN 0946-2171, 1432-0649.

doi: 10.1007/s00340-007-2630-x. URL http://link.springer.com/10.1007/s00340-007-2630-x.

[33] P. D. Maker and R. W. Terhune. Study of optical effects due to an induced polarization third order in the electric field strength. 137(3):A801–A818. ISSN 0031-899X. doi: 10.1103/PhysRev.137.A801. URL https://link.aps.org/doi/10.1103/PhysRev.137.A801.

[34] M. D. Duncan, J. Reintjes, and T. J. Manuccia. Scanning coherent anti-stokes raman microscope. 7(8):350. ISSN 0146-9592, 1539-4794. doi: 10.1364/OL.7.000350. URL https://www.osapublishing.org/abstract.cfm?URI=ol-7-8-350.

[35] Andreas Zumbusch, Gary R. Holtom, and X. Sunney Xie. Three-dimensional vibrational imaging by coherent anti-stokes raman scattering. 82(20):4142–4145. ISSN 0031-9007, 1079-7114. doi: 10.1103/PhysRevLett.82.4142. URL https://link.aps.org/doi/10.1103/PhysRevLett.82.4142.

[36] Pascal Berto, Esben Ravn Andresen, and Hervé Rigneault. Background-free stimulated raman spectroscopy and microscopy. *Physical review letters*, 112(5): 053905, 2014.

[37] D. W. Pohl, W. Denk, and M. Lanz. Optical stethoscopy: Image recording with resolution Îż/20. 44(7):651–653. ISSN 0003-6951, 1077-3118. doi: 10.1063/1.94865. URL http://aip.scitation.org/doi/10.1063/1.94865.

[38] E.H. Synge. XXXVIII. *A suggested method for extending microscopic resolution into the ultra-microscopic region.* 6(35):356–362. ISSN 1941-5982, 1941-5990. doi: 10.1080/14786440808564615. URL http://www.tandfonline.com/doi/abs/10.1080/14786440808564615.

[39] Stefan Hell and Ernst H. K. Stelzer. Properties of a 4pi confocal fluorescence microscope. *J. Opt. Soc. Am. A*, 9(12):2159–2166, Dec 1992. doi: 10.1364/JOSAA.9.002159. URL http://www.osapublishing.org/josaa/abstract.cfm?URI=josaa-9-12-2159.

[40] Stefan W. Hell, Ernst H. K. Stelzer, Steffen Lindek, and Christoph Cremer. Confocal microscopy with an increased detection aperture: type-b 4pi confocal microscopy. *Opt. Lett.*, 19(3):222–224, Feb 1994. doi: 10.1364/OL.19.000222. URL http://www.osapublishing.org/ol/abstract.cfm?URI=ol-19-3-222.

[41] Stefan Hell and Ernst H.K. Stelzer. Fundamental improvement of resolution with a 4pi-confocal fluorescence microscope using two-photon excitation. *Optics Communications*, 93(5):277–282, 1992. ISSN 0030-4018. doi: https:

//doi.org/10.1016/0030-4018(92)90185-T. URL https://www.sciencedirect.com/science/article/pii/003040189290185T.

[42] Mats GL Gustafsson, David A Agard, and John W Sedat. Sevenfold improvement of axial resolution in 3d wide-field microscopy using two objective-lenses. In *Three-Dimensional Microscopy: Image Acquisition and Processing II*, volume 2412, pages 147–156. International Society for Optics and Photonics, 1995.

[43] Mats GL Gustafsson, David A Agard, and John W Sedat. 3d widefield microscopy with two objective lenses: experimental verification of improved axial resolution. In *Three-Dimensional Microscopy: Image Acquisition and Processing III*, volume 2655, pages 62–66. International Society for Optics and Photonics, 1996.

[44] Mats GL Gustafsson, DA Agard, JW Sedat, et al. I5m: 3d widefield light microscopy with better than 100nm axial resolution. *Journal of microscopy*, 195 (1):10–16, 1999.

[45] Stefan W. Hell and Jan Wichmann. Breaking the diffraction resolution limit by stimulated emission: stimulated-emission-depletion fluorescence microscopy. *Opt. Lett.*, 19(11):780–782, Jun 1994. doi: 10.1364/OL.19.000780. URL http://www.osapublishing.org/ol/abstract.cfm?URI=ol-19-11-780.

[46] Thomas A. Klar and Stefan W. Hell. Subdiffraction resolution in far-field fluorescence microscopy. *Opt. Lett.*, 24(14):954–956, Jul 1999. doi: 10.1364/OL.24.000954. URL http://www.osapublishing.org/ol/abstract.cfm?URI=ol-24-14-954.

[47] Eric Betzig, George H Patterson, Rachid Sougrat, O Wolf Lindwasser, Scott Olenych, Juan S Bonifacino, Michael W Davidson, Jennifer Lippincott-Schwartz, and Harald F Hess. Imaging intracellular fluorescent proteins at nanometer resolution. *Science*, 313(5793):1642–1645, 2006.

[48] Samuel T Hess, Thanu PK Girirajan, and Michael D Mason. Ultra-high resolution imaging by fluorescence photoactivation localization microscopy. *Biophysical journal*, 91(11):4258–4272, 2006.

[49] Michael J Rust, Mark Bates, and Xiaowei Zhuang. Sub-diffraction-limit imaging by stochastic optical reconstruction microscopy (storm). *Nature methods*, 3(10): 793–796, 2006.

[50] Willard Miller Jr. Symmetry and separation of variables. 1977.

[51] Giuseppe Vicidomini, Paolo Bianchini, and Alberto Diaspro. STED super-resolved microscopy. 15(3):173–182. ISSN 1548-7091, 1548-7105. doi: 10.1038/nmeth.4593. URL http://www.nature.com/articles/nmeth.4593.

[52] Manish Saxena, Gangadhar Eluru, and Sai Siva Gorthi. Structured illumination microscopy. 7(2):241. ISSN 1943-8206. doi: 10.1364/AOP.7.000241. URL https://www.osapublishing.org/abstract.cfm?URI=aop-7-2-241.

[53] William Meiniel, Piernicola Spinicelli, Elsa D. Angelini, Alexandra Fragola, Vincent Loriette, FranÃğois Orieux, Eduardo Sepulveda, and Jean-Christophe Olivo-Marin. Reducing data acquisition for fast structured illumination microscopy using compressed sensing. In *2017 IEEE 14th International Symposium on Biomedical Imaging (ISBI 2017)*, pages 32–35, 2017. doi: 10.1109/ISBI.2017.7950461.

[54] Benjamin Thomas, Michelle Momany, and Peter Kner. Optical sectioning structured illumination microscopy with enhanced sensitivity. 15(9):094004, sep 2013. doi: 10.1088/2040-8978/15/9/094004. URL https://doi.org/10.1088/2040-8978/15/9/094004.

[55] Delphine Débarre, Edward J. Botcherby, Martin J. Booth, and Tony Wilson. Adaptive optics for structured illumination microscopy. *Opt. Express*, 16(13):9290–9305, Jun 2008. doi: 10.1364/OE.16.009290. URL http://www.osapublishing.org/oe/abstract.cfm?URI=oe-16-13-9290.

[56] Yicong Wu and Hari Shroff. Faster, sharper, and deeper: structured illumination microscopy for biological imaging. 15(12):1011–1019. ISSN 1548-7091, 1548-7105. doi: 10.1038/s41592-018-0211-z. URL http://www.nature.com/articles/s41592-018-0211-z.

[57] E. Mudry, K. Belkebir, J. Girard, J. Savatier, E. Le Moal, C. Nicoletti, M. Allain, and A. Sentenac. Structured illumination microscopy using unknown speckle patterns. 6(5):312–315. ISSN 1749-4885, 1749-4893. doi: 10.1038/nphoton.2012.83. URL http://www.nature.com/articles/nphoton.2012.83.

[58] Michael Hofmann, Christian Eggeling, Stefan Jakobs, and Stefan W Hell. Breaking the diffraction barrier in fluorescence microscopy at low light intensities by using reversibly photoswitchable proteins. *Proceedings of the National Academy of Sciences*, 102(49):17565–17569, 2005.

[59] W. Ruchira Silva, Christian T. Graefe, and Renee R. Frontiera. Toward label-free super-resolution microscopy. 3(1):79–86. ISSN 2330-4022, 2330-4022. doi: 10.1021/acsphotonics.5b00467. URL https://pubs.acs.org/doi/10.1021/acsphotonics.5b00467.

[60] Doyeon Kim, Dae Sik Choi, Jiwoong Kwon, Sang-Hee Shim, Hanju Rhee, and Minhaeng Cho. Selective suppression of stimulated raman scattering with another competing stimulated raman scattering. 8(24):6118–6123, . ISSN 1948-7185. doi:

10.1021/acs.jpclett.7b02752. URL https://pubs.acs.org/doi/10.1021/acs.jpclett.7b02752.

[61] Sohee Lim, Dae Sik Choi, Hanju Rhee, and Minhaeng Cho. An efficient switching-off of coherent anti-stokes raman scattering via double stimulated raman scattering processes of heteromolecular vibrational modes. *The Journal of Physical Chemistry B*, 124(17):3583–3590. ISSN 1520-6106, 1520-5207. doi: 10.1021/acs.jpcb.0c03080. URL https://pubs.acs.org/doi/10.1021/acs.jpcb.0c03080.

[62] Willem P. Beeker, Petra GroÃ§, Chris J. Lee, Carsten Cleff, Herman L. Offerhaus, Carsten Fallnich, Jennifer L. Herek, and Klaus-Jochen Boller. A route to sub-diffraction-limited CARS microscopy. *Optics Express*, 17(25):22632, 2009. ISSN 1094-4087. doi: 10.1364/OE.17.022632.

[63] Willem P. Beeker, Chris J. Lee, Klaus-Jochen Boller, Petra Groß, Carsten Cleff, Carsten Fallnich, Herman L. Offerhaus, and Jennifer L. Herek. Spatially dependent rabi oscillations: An approach to sub-diffraction-limited coherent anti-stokes raman-scattering microscopy. *Phys. Rev. A*, 81:012507, Jan 2010. doi: 10.1103/PhysRevA.81.012507. URL https://link.aps.org/doi/10.1103/PhysRevA.81.012507.

[64] Kim M. Hajek, Brad Littleton, Douglas Turk, Timothy J. McIntyre, and Halina Rubinsztein-Dunlop. A method for achieving super-resolved widefield CARS microscopy. 18(18):19263. ISSN 1094-4087. doi: 10.1364/OE.18.019263. URL https://www.osapublishing.org/oe/abstract.cfm?uri=oe-18-18-19263.

[65] Varun Raghunathan and Eric Olaf Potma. Multiplicative and subtractive focal volume engineering in coherent raman microscopy. 27(11):2365. ISSN 1084-7529, 1520-8532. doi: 10.1364/JOSAA.27.002365. URL https://www.osapublishing.org/abstract.cfm?URI=josaa-27-11-2365.

[66] Wei Liu and Hanben Niu. Diffraction barrier breakthrough in coherent anti-stokes raman scattering microscopy by additional probe-beam-induced phonon depletion. *Physical Review A*, 83(2):023830. ISSN 1050-2947, 1094-1622. doi: 10.1103/PhysRevA.83.023830. URL https://link.aps.org/doi/10.1103/PhysRevA.83.023830.

[67] Carsten Cleff, Petra GroÃ§, Carsten Fallnich, Herman L. Offerhaus, Jennifer L. Herek, Kai Kruse, Willem P. Beeker, Chris J. Lee, and Klaus-Jochen Boller. Ground-state depletion for subdiffraction-limited spatial resolution in coherent anti-stokes raman scattering microscopy. *Physical Review A*, 86(2):023825. ISSN 1050-2947, 1094-1622. doi: 10.1103/PhysRevA.86.023825. URL https://link.aps.org/doi/10.1103/PhysRevA.86.023825.

[68] Hyunmin Kim, Garnett W. Bryant, and Stephan J. Stranick. Superresolution four-wave mixing microscopy. 20(6):6042, . ISSN 1094-4087. doi: 10.1364/OE.20.006042. URL https://www.osapublishing.org/oe/abstract.cfm?uri=oe-20-6-6042.

[69] D. D. Yavuz and Z. J. Simmons. Optical imaging with nanoscale resolution using optical nonlinearities and spatiotemporal modulation. *Physical Review A*, 86(1): 013817. ISSN 1050-2947, 1094-1622. doi: 10.1103/PhysRevA.86.013817. URL https://link.aps.org/doi/10.1103/PhysRevA.86.013817.

[70] Li Gong and Haifeng Wang. Breaking the diffraction limit by saturation in stimulated-raman-scattering microscopy: A theoretical study. 90(1):013818, . ISSN 1050-2947, 1094-1622. doi: 10.1103/PhysRevA.90.013818. URL https://link.aps.org/doi/10.1103/PhysRevA.90.013818.

[71] Li Gong and Haifeng Wang. Suppression of stimulated raman scattering by an electromagnetically-induced-transparencyâĂŞlike scheme and its application for super-resolution microscopy. *Physical Review A*, 92(2):023828, . ISSN 1050-2947, 1094-1622. doi: 10.1103/PhysRevA.92.023828. URL https://link.aps.org/doi/10.1103/PhysRevA.92.023828.

[72] Yasuo Yonemaru, Almar F. Palonpon, Shogo Kawano, Nicholas I. Smith, Satoshi Kawata, and Katsumasa Fujita. Super-spatial- and -spectral-resolution in vibrational imaging via saturated coherent anti-stokes raman scattering. *Phys. Rev. Applied*, 4(1):014010. ISSN 2331-7019. doi: 10.1103/PhysRevApplied.4.014010. URL https://link.aps.org/doi/10.1103/PhysRevApplied.4.014010.

[73] Kozue Watanabe, Almar F. Palonpon, Nicholas I. Smith, Liang-da Chiu, Atsushi Kasai, Hitoshi Hashimoto, Satoshi Kawata, and Katsumasa Fujita. Structured line illumination raman microscopy. 6(1):10095. ISSN 2041-1723. doi: 10.1038/ncomms10095. URL http://www.nature.com/articles/ncomms10095.

[74] Ryan Beams and Stephan Stranick. Side lobe suppression in phase mask-based nonlinear superresolution microscopy. In Prabhat Verma and Alexander Egner, editors, *Nanoimaging and Nanospectroscopy V*, page 8. SPIE. ISBN 978-1-5106-1157-3 978-1-5106-1158-0. doi: 10.1117/12.2275870. URL https://www.spiedigitallibrary.org/conference-proceedings-of-spie/10350/2275870/Side-lobe-suppression-in-phase-mask-based-nonlinear-superresolution-microscopy/10.1117/12.2275870.full.

[75] Dae Sik Choi, B. Jayachander Rao, Doyeon Kim, Sang-Hee Shim, Hanju Rhee, and Minhaeng Cho. Selective suppression of CARS signal with three-beam com-

peting stimulated raman scattering processes. 20(25):17156–17170. ISSN 1463-9084. doi: 10.1039/C8CP02230E. URL https://pubs.rsc.org/en/content/articlelanding/2018/cp/c8cp02230e.

[76] B. Jayachander Rao and Minhaeng Cho. Three-beam double stimulated raman scatterings: Cascading configuration. *The Journal of Chemical Physics*, 148 (11):114201. ISSN 0021-9606, 1089-7690. doi: 10.1063/1.5022092. URL http://aip.scitation.org/doi/10.1063/1.5022092.

[77] B. Jayachander Rao, Dae Sik Choi, and Minhaeng Cho. Selective suppression of CARS signal with two competing stimulated raman scattering processes. *The Journal of Chemical Physics*, 149(23):234202. ISSN 0021-9606, 1089-7690. doi: 10.1063/1.5053435. URL http://aip.scitation.org/doi/10.1063/1.5053435.

[78] Li Gong, Wei Zheng, Ying Ma, and Zhiwei Huang. Saturated stimulated-raman-scattering microscopy for far-field superresolution vibrational imaging. 11(3): 034041. ISSN 2331-7019. doi: 10.1103/PhysRevApplied.11.034041. URL https://link.aps.org/doi/10.1103/PhysRevApplied.11.034041.

[79] T. WÃijrthwein, N. Irwin, and C. Fallnich. Saturated raman scattering for sub-diffraction-limited imaging. *The Journal of Chemical Physics*, 151(19):194201. ISSN 0021-9606. doi: 10.1063/1.5128874. URL https://aip.scitation.org/doi/10.1063/1.5128874.

[80] Hanqing Xiong, Naixin Qian, Yupeng Miao, Zhilun Zhao, Chen Chen, and Wei Min. Super-resolution vibrational microscopy by stimulated Raman excited fluorescence. *Light: Science & Applications*, 10(1):87, dec 2021. ISSN 2047-7538. doi: 10.1038/s41377-021-00518-5. URL http://www.nature.com/articles/s41377-021-00518-5.

[81] Christian T Graefe, David Punihaole, Michael J Lynch, W Ruchira Silva, and Renee R Frontiera. Stimulated raman imaging below the diffraction limit with a mhz laser. *Journal of Raman Spectroscopy*, 52(2):404–411, 2021.

[82] Felix Scholkmann, Stefan Kleiser, Andreas Jaakko Metz, Raphael Zimmermann, Juan Mata Pavia, Ursula Wolf, and Martin Wolf. A review on continuous wave functional near-infrared spectroscopy and imaging instrumentation and methodology. *Neuroimage*, 85:6–27, 2014.

[83] W.F. Cheong, S.A. Prahl, and A.J. Welch. A review of the optical properties of biological tissues. 26(12):2166–2185. ISSN 00189197. doi: 10.1109/3.64354. URL http://ieeexplore.ieee.org/document/64354/.

[84] A N Yaroslavsky, P C Schulze, I V Yaroslavsky, R Schober, F Ulrich, and H-J Schwarzmaier. Optical properties of selected native and coagulated human brain tissues in vitro in the visible and near infrared spectral range. 47(12): 2059–2073. ISSN 00319155. doi: 10.1088/0031-9155/47/12/305. URL https://iopscience.iop.org/article/10.1088/0031-9155/47/12/305.

[85] S. Hell, G. Reiner, C. Cremer, and E. H. K. Stelzer. Aberrations in confocal fluorescence microscopy induced by mismatches in refractive index. 169(3):391–405. ISSN 00222720. doi: 10.1111/j.1365-2818.1993.tb03315.x. URL https://onlinelibrary.wiley.com/doi/10.1111/j.1365-2818.1993.tb03315.x.

[86] C. Soeller and M. B. Cannell. Two-photon microscopy: Imaging in scattering samples and three-dimensionally resolved flash photolysis. 47(3):182–195. ISSN 1059-910X, 1097-0029. doi: 10.1002/(SICI)1097-0029(19991101)47:3<182::AID-JEMT4>3.0.CO;2-4. URL https://onlinelibrary.wiley.com/doi/10.1002/(SICI)1097-0029(19991101)47:3<182::AID-JEMT4>3.0.CO;2-4.

[87] Xiaojun Cheng, Sanaz Sadegh, Sharvari Zilpelwar, Anna Devor, Lei Tian, and David A. Boas. Comparing the fundamental imaging depth limit of two-photon, three-photon, and non-degenerate two-photon microscopy. 45(10):2934, . ISSN 0146-9592, 1539-4794. doi: 10.1364/OL.392724. URL https://www.osapublishing.org/abstract.cfm?URI=ol-45-10-2934.

[88] Joseph W Goodman. *Statistical optics*. John Wiley & Sons, 2015.

[89] Peter Kovesi. Good colour maps: How to design them. URL http://arxiv.org/abs/1509.03700.

[90] Fritjof Helmchen and Winfried Denk. Deep tissue two-photon microscopy. 2 (12):932–940. ISSN 1548-7091, 1548-7105. doi: 10.1038/nmeth818. URL http://www.nature.com/articles/nmeth818.

[91] Sébastien Popoff. Setting up a DMD: Diffraction effects - wavefrontshaping.net. URL https://www.wavefrontshaping.net/post/id/21.

[92] Ji-xin Cheng, Andreas Volkmer, Lewis D Book, and X Sunney Xie. An epi-detected coherent anti-stokes raman scattering (e-cars) microscope with high spectral resolution and high sensitivity. *The Journal of Physical Chemistry B*, 105(7):1277–1280, 2001.

[93] Pascal Berto, Esben Ravn Andresen, and HervÃľ Rigneault. Background-free stimulated raman spectroscopy and microscopy. 112(5):053905. ISSN 0031-9007, 1079-7114. doi: 10.1103/PhysRevLett.112.053905. URL https://link.aps.org/doi/10.1103/PhysRevLett.112.053905.

[94] Halina Abramczyk, Beata Brozek-Pluska, Marta Krzesniak, Monika Kopec, and Alina Morawiec-Sztandera. The cellular environment of cancerous human tissue. interfacial and dangling water as a âĂIJhydration fingerprintâĂİ. 129:609–623. ISSN 13861425. doi: 10.1016/j.saa.2014.03.103. URL https://linkinghub.elsevier.com/retrieve/pii/S1386142514005149.

[95] Julien Guilbert, Awoke Negash, Simon Labouesse, Sylvain Gigan, Anne Sentenac, and Hilton B. de Aguiar. Label-free super-resolution chemical imaging of biomedical specimens. URL http://biorxiv.org/lookup/doi/10.1101/2021.05.14.444185.

[96] P Nandakumar, A Kovalev, and A Volkmer. Vibrational imaging based on stimulated raman scattering microscopy. 11(3):033026. ISSN 1367-2630. doi: 10.1088/1367-2630/11/3/033026. URL https://iopscience.iop.org/article/10.1088/1367-2630/11/3/033026.

[97] Li-Hao Yeh, Lei Tian, and Laura Waller. Structured illumination microscopy with unknown patterns and a statistical prior. 8(2):695. ISSN 2156-7085, 2156-7085. doi: 10.1364/BOE.8.000695. URL https://www.osapublishing.org/abstract.cfm?URI=boe-8-2-695.

[98] Florian Stehr, Johannes Stein, Florian Schueder, Petra Schwille, and Ralf Jungmann. Flat-top TIRF illumination boosts DNA-PAINT imaging and quantification. 10(1):1268. ISSN 2041-1723. doi: 10.1038/s41467-019-09064-6. URL https://www.nature.com/articles/s41467-019-09064-6. Bandiera_abtest: a Cc_license_type: cc_by Cg_type: Nature Research Journals Number: 1 Primary_atype: Research Publisher: Nature Publishing Group Subject_term: Fluorescence imaging;Super-resolution microscopy Subject_term_id: fluorescence-imaging;super-resolution-microscopy.

[99] Guanghao Zhu, James Van Howe, Michael Durst, Warren Zipfel, and Chris Xu. Simultaneous spatial and temporal focusing of femtosecond pulses. *Optics express*, 13(6):2153–2159, 2005.

[100] Yan Fu, T. B. Huff, Han-Wei Wang, Ji-Xin Cheng, and Haifeng Wang. Ex vivo and in vivo imaging of myelin fibers in mouse brain by coherent anti-stokes raman scattering microscopy. 16(24):19396. ISSN 1094-4087. doi: 10.1364/OE.16.019396. URL https://www.osapublishing.org/oe/abstract.cfm?uri=oe-16-24-19396.

[101] Thomas Hellerer, Annika MK Enejder, and Andreas Zumbusch. Spectral focusing: High spectral resolution spectroscopy with broad-bandwidth laser pulses. *Applied Physics Letters*, 85(1):25–27, 2004.

[102] Mats GL Gustafsson. Nonlinear structured-illumination microscopy: wide-field fluorescence imaging with theoretically unlimited resolution. *Proceedings of the National Academy of Sciences*, 102(37):13081–13086, 2005.

[103] WT Welford. Laser speckle and surface roughness. *Contemporary Physics*, 21 (4):401–412, 1980.

[104] Th M Nieuwenhuizen and MCW Van Rossum. Intensity distributions of waves transmitted through a multiple scattering medium. *Physical review letters*, 74 (14):2674, 1995.

[105] Joseph W Goodman. *Speckle phenomena in optics: theory and applications*. Roberts and Company Publishers, 2007.

[106] Peilong Hong, Jianbin Liu, and Guoquan Zhang. Two-photon superbunching of thermal light via multiple two-photon path interference. *Physical Review A*, 86 (1):013807, 2012.

[107] Yaron Bromberg and Hui Cao. Generating non-rayleigh speckles with tailored intensity statistics. 112(21):213904. doi: 10.1103/PhysRevLett.112.213904. URL `https://link.aps.org/doi/10.1103/PhysRevLett.112.213904`.

[108] Nicholas Bender, Hasan YÄślmaz, Yaron Bromberg, and Hui Cao. Customizing speckle intensity statistics. 5(5):595–600. ISSN 2334-2536. doi: 10.1364/OPTICA.5.000595. URL `https://www.osapublishing.org/optica/abstract.cfm?uri=optica-5-5-595`.

[109] Ralph W Gerchberg. A practical algorithm for the determination of phase from image and diffraction plane pictures. *Optik*, 35:237–246, 1972.

[110] Kyrus Kuplicki and Kam Wai Clifford Chan. High-order ghost imaging using non-rayleigh speckle sources. 24(23):26766. ISSN 1094-4087. doi: 10.1364/OE.24.026766. URL `https://www.osapublishing.org/abstract.cfm?URI=oe-24-23-26766`.

[111] Xiaojun Cheng, Yunzhe Li, Jerome Mertz, Sava SakadÅ¿iÄĞ, Anna Devor, David A. Boas, and Lei Tian. Development of a beam propagation method to simulate the point spread function degradation in scattering media. 44 (20):4989, . ISSN 0146-9592, 1539-4794. doi: 10.1364/OL.44.004989. URL `https://www.osapublishing.org/abstract.cfm?URI=ol-44-20-4989`.

[112] Feruz Ganikhanov, Conor L. Evans, Brian G. Saar, and X. Sunney Xie. High-sensitivity vibrational imaging with frequency modulation coherent anti-stokes

raman scattering (FM CARS) microscopy. 31(12):1872. ISSN 0146-9592, 1539-4794. doi: 10.1364/OL.31.001872. URL https://www.osapublishing.org/abstract.cfm?URI=ol-31-12-1872.

[113] Li Li, Haifeng Wang, and Ji-Xin Cheng. Quantitative coherent anti-stokes raman scattering imaging of lipid distribution in coexisting domains. 89(5):3480–3490. ISSN 00063495. doi: 10.1529/biophysj.105.065607. URL https://linkinghub.elsevier.com/retrieve/pii/S0006349505729891.

RÉSUMÉ

L'objectif de ce doctorat est de développer une nouvelle technique d'imagerie et notamment une méthode n'utilisant pas de marqueurs chimiques. Plus précisément, cette thèse se propose de développer une technique d'imagerie de super résolution sans marqueur et compatible avec les tissus biologiques qui sont généralement considérés comme fragiles, c'est à dire qu'ils ne peuvent supporter une densité d'énergie trop élevée. Afin d'imager des tissus sans marqueur et de pouvoir cibler un type précis de molécule, la diffusion Raman est une candidate idéale car toutes les molécules possèdent des signatures uniques appelées résonances de diffusion Raman. Cependant, le caractère spontané de l'émission ne permettrait pas d'imager suffisamment rapidement. Une solution communément employée et que nous avons exploitée dans cette thèse est l'utilisation du signal de la diffusion Raman cohérente qui améliore considérablement la section efficace du signal et donc la vitesse d'imagerie. Néanmoins, les techniques de microscopie sont limitées en résolution par la diffraction, ce qui peut être problématique lors de l'imagerie de structures biologiques sub-longueur d'onde. Afin d'obtenir des images allant au delà de la limite de résolution, nous avons choisi de développer durant cette thèse une technique utilisant la diffusion Raman cohérente avec une stratégie originale de balayage de faisceau afin de pouvoir l'utiliser en combinaison avec des techniques de microscopie par illuminations structurées. Nous montrerons dans le manuscrit des simulations numériques de cette technique et des images expérimentales sur des objets calibrés mais également sur des tranches de cerveau de souris pour démontrer que cette technique est effectivement capable d'atteindre la super résolution mais qu'elle est également compatible avec l'imagerie de tissus biologiques. Nous développons ensuite des idées pour aller plus loin et améliorer les performances de cette nouvelle technique d'imagerie.

MOTS CLÉS

Diffusion Raman stimulée, super-résolution, imagerie, optique, tissu biologique, reconstruction algorithmique

SUMMARY

The objective of this PhD is to develop a new imaging technique and in particular a method which is not using any chemical markers. More precisely, this PhD proposes to develop a super-resolution imaging technique which does not require any markers and is compatible with biological tissues which are generally considered as fragile, i.e. they cannot support a too high energy density. In order to image tissues without markers and to be able to target a specific type of molecule, Raman scattering is an ideal candidate because all molecules have unique signatures called Raman scattering resonances. However, the spontaneous nature of the emission would not allow sufficiently fast imaging. A commonly used solution that we have exploited in this PhD is the use of the coherent Raman scattering signal which considerably improves the cross section of the signal and thus the imaging speed. Nevertheless, microscopy techniques are limited in resolution by diffraction, which can be problematic when imaging sub-wavelength biological structures. During this PhD, in order to obtain images beyond the resolution limit, we have chosen to develop a technique using coherent Raman scattering with an original scanning strategy that enables to use it in combination with structured illumination microscopy techniques. We will show in the manuscript numerical simulations of this technique and experimental images on calibrated objects but also on mouse brain slices to demonstrate that this technique is indeed able to reach super resolution but that it is also compatible with the imaging of biological tissues. We then elaborate on ideas to go further and improve the performances of this new imaging technique.

KEYWORDS

Stimulated Raman scattering, super resolution, imaging, optics, biological tissue, algorithmic reconstruction